A single-cell transcriptomic and anatomic atlas of mouse dorsal raphe *Pet1* neurons

Authors: Benjamin W. Okaty*#, Nikita Sturrock*, Yasmin Escobedo Lozoya, YoonJeung Chang, Krissy A. Lyon, Olga V. Alekseyenko, Susan M. Dymecki#

Department of Genetics, Harvard Medical School, Boston, MA, USA.

* These authors contributed equally

Corresponding Authors

Abstract

The dorsal raphe nucleus (DR) contains the largest brain population of *Pet1*-lineage neurons, a predominantly serotonergic group distributed throughout multiple DR subdomains. These neurons collectively regulate diverse physiology and behavior and are often therapeutically targeted to treat affective disorders. Characterizing *Pet1* neuron molecular heterogeneity and relating it to anatomy is vital for understanding DR functional organization, with potential to inform therapeutic separability. Here we use high-throughput and DR subdomain-targeted single-cell transcriptomics and intersectional genetic tools to map molecular and anatomical diversity of DR-*Pet1* neurons. We describe up to fourteen neuron subtypes, many showing biased cell body distributions across the DR. We further show that *P2ry1-Pet1* DR neurons – the most molecularly distinct of the subtypes – possess unique efferent projections and electrophysiological properties. The present data complement and extend previous DR characterizations, combining intersectional genetics with multiple transcriptomic modalities to achieve fine-scale molecular and anatomic identification of *Pet1* neuron subtypes.

Introduction

Brainstem neurons that synthesize the monoamine neurotransmitter serotonin (5-hydroxytryptamine, 5-HT) (Baker et al., 1991a; Baker et al., 1991b; Baker et al., 1990; Dahlstroem and Fuxe, 1964; Ishimura et al., 1988; Steinbusch, 1981; Steinbusch et al., 1978) derive from embryonic precursors that express the transcription factor PET1 (alias FEV) upon terminal cell division (Hendricks et al., 1999). PET1 shapes the serotonergic identity of neurons by regulating expression of genes required for 5-HT biosynthesis, packaging in synaptic vesicles, reuptake, and metabolism (Hendricks et al., 2003; Krueger and Deneris, 2008; Liu et al., 2010; Wyler et al., 2015; Wyler et al., 2016), though some *Pet1*-lineage cells in the brain have ambiguous phenotypes with respect to their ability to synthesize and release 5-HT (Alonso et al., 2013; Barrett et al., 2016; Okaty et al., 2015; Pelosi et al., 2014; Sos et al., 2017). Aside from shared expression of 5-HT marker genes (to varying degrees), *Pet1*-lineage neurons display wide-ranging phenotypic heterogeneity, including diverse brainstem anatomy, hodology, and expression of neurotransmitters in addition to or other than 5-HT, suggestive of distinct *Pet1* neuron subtypes with divergent neural circuit functions (recently reviewed in (Okaty et al., 2019)). We have previously shown that the mature molecular identities of *Pet1*-lineage neurons strongly correlate with both the embryonic progenitor domain (rhombomeric domain) from which they derive and with their mature anatomy (Jensen et al., 2008; Okaty et al., 2015), largely consistent with (Alonso et al., 2013). However, even within a given *Pet1* rhombomeric sublineage and anatomical subdomain, *Pet1* neurons may display different molecular and cellular phenotypes (Niederkofler et al., 2016; Okaty et al., 2015). *Pet1* neurons project widely throughout the brain and are functionally implicated in numerous life-sustaining biological processes and human pathologies. Thus, assembling a taxonomy of *Pet1* neuron subtypes based on molecular and cellular properties and linking identified *Pet1* neuron subtypes to specific biological functions is important for basic neuroscience and human health, including the development of targeted therapeutics. Here we provide a

high-resolution, single-cell transcriptomic atlas of dorsal raphe *Pet1*-lineage neurons revealing hierarchically and spatially organized molecular subtypes, each expressing unique repertoires of neurotransmitters, plasma membrane receptors, ion channels, cell adhesion molecules, and other gene categories important for specifying neuronal functions.

The dorsal raphe (DR) nucleus comprises the largest anatomically defined subgroup of *Pet1* expressing cells in the brain, and these cells are derived from embryonic progenitors in the isthmus and rhombomere 1 (Alonso et al., 2013; Jensen et al., 2008). Multiple studies have demonstrated neuronal diversity within the DR, in *Pet1*-expressing 5-HT neurons as well as other resident cell populations (Calizo et al., 2011; Challis et al., 2013; Crawford et al., 2010; Fernandez et al., 2016; Huang et al., 2019; Kirby et al., 2003; Niederkofler et al., 2016; Prouty et al., 2017; Ren et al., 2018; Ren et al., 2019; Spaethling et al., 2014; Vasudeva and Waterhouse, 2014; Zeisel et al., 2018). In the present study, we extend these findings by transcriptionally profiling *Pet1*-lineage marked DR neurons using microfluidic cell sorting and droplet-based single-cell RNA sequencing (scRNA-seq). Our particular experimental approach combining intersectional mouse genetics, high-throughput cell-type-specific purification (using the On-Chip Biotechnologies microfluidic sorter), and newly improved scRNA-seq library construction chemistry (using the 10X Genomics Chromium Single Cell 3' v3 kit) allowed us to surpass prior resolution of DR *Pet1* neuron molecular diversity, both in terms of the number of DR *Pet1* cells profiled and the number of transcriptomically distinct *Pet1* neuron subtypes identified. To further characterize the anatomical organization of these molecularly defined *Pet1* neuron subtypes, we used intersectional mouse transgenic tools, crossing *Pet1::Flpe* mice with various subtype-relevant Cre-driver mice and dual Flpe- and Cre-responsive fluorescent reporter lines. In addition to performing histological analyses of these intersectionally defined *Pet1*-lineage neuron subpopulations, we further characterized them using manual cell-sorting from microdissected sub-domains of the DR followed by scRNA-seq. Comparing this data with our

high-throughput droplet-based scRNA-seq approach allowed us to map *Pet1* neuron molecular diversity onto DR anatomy. We found that DR *Pet1*-lineage neurons comprise as many as fourteen distinct molecularly defined subtypes, several of which we show are anatomically biased within rostral-caudal, dorsal-ventral, and medial-lateral axes. Additionally, by combining intersectional genetics with projection mapping and *ex vivo* slice electrophysiology we show examples of distinct *Pet1* neuron molecular subtypes that also differ in other cellular phenotypes important for function, such as hodology and electrophysiology.

Results

Droplet-based scRNA-seq of *Pet1* fate-mapped DR neurons reveals new molecularly defined neuron subtypes

To characterize the molecular diversity of *Pet1*-lineage DR neurons in a targeted, high-throughput, high-resolution manner we partnered recombinase-based genetic fate mapping, microfluidic fluorescence-based cell sorting, and droplet-based single-cell barcoding followed by RNA-seq library preparation and next-generation sequencing using the 10X Genomics Chromium Single Cell 3' v3 kit (**Figure 1A; Methods**). Fluorescent labeling of *Pet1*-lineage DR neurons was achieved in mice of the following genotypes: (1) *Pet1::Flpe* (Jensen et al., 2008); *En1::cre* (Kimmel et al., 2000); *RC::FrePe* (the latter transgene a dual Flpe- and Cre-dependent fluorescent reporter inserted into the *ROSA26* (*R26*) locus (Brust et al., 2014; Dymecki et al., 2010; Okaty et al., 2015)), in which *Pet1*-lineage neurons derived from the *En1*$^{+}$ isthmus and rhombomere 1 (r1) embryonic progenitor domains, are marked by eGFP expression or (2) *Pet1::Flpe; RC*::*FL-hM3Dq* (Sciolino et al., 2016), in which all *Pet1* neurons are eGFP-labeled (Cre was not utilized in these experiments, thus only eGFP, not hM3Dq, was expressed).

Brains were acutely dissected from 6-10 week old mice of both genotypes (4 males and 6 females), and DR cells were dissociated as previously described (Okaty et al., 2015) (also see **Methods**). eGFP-expressing neurons were selectively purified using the On-Chip Biotechnologies microfluidic cell sorter, a recently developed technology that greatly reduces the pressure forces typically exerted on cells in conventional flow sorters, thereby achieving higher levels of cell viability (Watanabe et al., 2014). Indeed, examination of sorted neurons revealed that many still had intact processes emanating from their somas. Cells were then run through the 10X Genomics Chromium Single Cell 3' v3 protocol, followed by Illumina NextSeq 500 sequencing. The Cell Ranger pipeline was used for transcript mapping and single-cell de-multiplexing, and all analyses of transcript counts were performed using the R package Seurat (Butler et al., 2018; Stuart et al., 2019) (also see **Methods**). After stringently filtering out "suspect" single-cell libraries (e.g. libraries with high levels of non-neuronal or mitochondrial genes, outlier library complexity, or absence/low levels of *Pet1* transcripts), we obtained 2,350 single cells for further analysis, with a mean of 7,521 genes detected per single cell library (mean of 57,678 UMIs per cell), and a total of 17,231 genes detected in aggregate (after filtering out genes that were expressed in fewer than ten cells).

As the principal goal of our scRNA-seq experiments was to characterize molecular diversity of *Pet1*-lineage neurons, our analyses were aimed at identifying genes with significantly variable transcript expression across single neurons, and using these gene expression differences to classify *Pet1*-lineage neuron subtypes. Typical clustering approaches used to classify cell types (or cell states) based on scRNA-seq data are largely unsupervised, but do require supervised input regarding a number of parameters that have the potential to significantly alter the resulting cluster assignments. These parameters include the data reduction used prior to clustering (such as principal components analysis), the number of components included in the reduction, and a resolution or granularity parameter that determines the "community" size of clusters (i.e.

whether cluster boundaries are more or less inclusive; coarse-grained or fine-grained). Rather than arbitrarily choosing a set of parameters for our *Pet1*-lineage neuron subtype classification, we chose a more exploratory approach by systematically varying key parameters and examining how sensitive the resulting clusters were to these combinations of parameters.

First, single-cell transcript counts were log-normalized, and we carried out principal components analysis (PCA) on the scaled and centered expression values of the top two thousand genes with the highest variance (after applying a variance-stabilizing transform, see **Methods**) in order to reduce the dimensionality of the data onto a smaller set of composite variables that represent the most salient gene expression differences. Plotting the variance explained by each principal component we observed an inflection point, or "elbow", around the fiftieth component suggesting a drop-off in the information content of subsequent components (**Figure 1–figure supplement 1A**), and found that roughly forty percent of the total variance was explained by these first fifty components. Further examination of the gene loadings of each component revealed that components six and seven were heavily weighted towards sex-specific transcripts and transcripts that largely correlated with batch. As our experiments were not designed to explicitly compare sex as a variable, and given the difficulties of interpreting batch-correlated gene expression differences (e.g. these could stem from population sampling biases of the different cell sorts, different genotypes used, different balance of sexes, or any number of idiosyncratic biological and technical differences) we ultimately chose to remove components six and seven from downstream analyses (though we found that their inclusion had only modest effects on data clustering).

Next, we varied: (1) the number of PCs included in the data reduction (from one to fifty, excluding PCs six and seven) used as input to the Seurat FindNeighbors function, and (2) the resolution parameter in the Seurat FindClusters function (from 0.1 to 2.0, in intervals of 0.1, using the Louvain algorithm). The results of this analysis are summarized in the contour plot in **Figure 1–figure supplement**

1B. Including only the first few principal components led to highly variable numbers of clusters depending on the resolution parameter (resulting in as many as 40 clusters at the highest resolution). However, for all resolutions the number of clusters mostly stabilized after including the first thirty PCs. In this regime of parameter space the number of clusters was, for the most part, bounded between five and twenty depending on the resolution. As a first pass at homing in on the "optimum" number of clusters (strictly in a heuristic sense), we calculated the frequency of obtaining a given number of clusters over all combinations of parameters, reasoning that cluster numbers that are less sensitive to precise tuning of parameters would appear more frequently, and the "robustness" of these cluster numbers might more faithfully reflect biologically meaningful subgroup structure in the data. The cluster number frequency plot in **Figure 1–figure supplement 1C** shows that there are four local maxima and one global maximum corresponding to five, eight, eleven, fourteen, and seventeen clusters respectively. Given the high frequency of these cluster numbers, we chose to examine their composition more carefully. As multiple combinations of parameters lead to the same number of clusters (**Figure 1–figure supplement 1D**), in some cases leading to differences in cluster composition (generally subtle), we decided to err on the side of including more data and thus fixed the number of PCs at one to fifty, excluding PCs six and seven, and varied the resolution to obtain five, eight, eleven, fourteen, and seventeen clusters.

We characterized cluster structure through hierarchical dendrograms, uniform manifold approximation and projection for dimension reduction (UMAP) (a technique recently developed by McInness, Healy, and Melville as described in a manuscript available at arXiv.org, and implemented in Seurat), and differential expression analysis using Wilcoxon rank-sum tests to identify transcripts that are significantly enriched or depleted among clusters (**Figure 1–figure supplement 2A-I**, **Figure 1 B-D**). We ultimately judged seventeen clusters (resolution = 1.5) to be excessive, due to the inclusion of clusters with very few enriched genes as well as clusters that appeared somewhat intermixed in UMAP space (analysis

not shown). We thus focused our analyses on lower resolution clusters. Across all resolutions analyzed (0.1, 0.3, 0.7, and 0.9), we found a common set of genes that was useful in characterizing cluster structure, namely *Tph2, Gad2, Gad1, Slc17a8 (*alias *Vglut3*)*,* and *Met*. The *Tph2* gene encodes for tryptophan hydroxylase 2, the rate-limiting enzyme involved in 5-HT biosynthesis in the central nervous system (Walther and Bader, 2003; Walther et al., 2003), and all but one cluster showed consistently high *Tph2* transcript expression. In the five- and eight-cluster-number analyses (resolution = 0.1 and 0.3, respectively), one cluster displayed a strikingly bi-modal distribution of *Tph2* transcript expression (**Figure 1–figure supplement 2A,D**, clusters four and six, respectively), however increasing the resolution further divided this group into a *Tph2*-low and a *Tph2*-"variable" group, displaying a broader distribution of single-cell expression than other clusters (**Figure 1–figure supplement 2G** and **Figure 1B**, clusters ten and fourteen, respectively, corresponding to resolutions of 0.7 and 0.9). Beyond *Tph2* expression, these two subgroups displayed similarly shaped distributions (lower mean expression and higher variability) for several 5-HT neuron marker genes (**Figure 1–figure supplement 3**). *Gad1* and *Gad2* are paralogous genes that encode two distinct forms of the gamma-aminobutyric acid (GABA) synthetic enzyme glutamate decarboxylase (Erlander et al., 1991), and we found a sizable cluster of *Pet1* neurons (~50%) that express high levels of *Tph2* and *Gad2*, and to a lesser extent *Gad1* (generally detected in fewer cells than *Gad2*), which could be further subdivided into five sub-clusters at finer resolution (**Figure 1B, C,** clusters two-six**)**. One of these clusters, cluster six (**Figure 1B,C**), contained *Pet1* neurons additionally expressing intermediate levels of transcripts for *Vglut3,* encoding the vesicular glutamate transporter 3 (Fremeau et al., 2002; Gras et al., 2002). Notably, this group of neurons also had the highest expression of *Gad1* relative to other groups. High expression levels of *Vglut3* transcripts were detected in eight clusters (**Figure 1B, C,** clusters seven to fourteen), comprising ~46% of profiled *Pet1* neurons, including the *Tph2*-low and *Tph2*-variable clusters (**Figure 1B, C,** clusters 13 and 14). Cluster twelve, the most striking outlier group of *Pet1* neurons, is characterized by high transcript expression of

Tph2, *Vglut3,* and *Met,* the latter encoding the MET proto-oncogene (also known as hepatocyte growth factor receptor) (Iyer et al., 1990). The remaining 4% of *Pet1* neurons, comprising cluster one, expressed high levels of *Tph2* transcripts but only sporadically expressed transcripts for *Gad2*, *Gad1*, or *Vglut3* (**Figure 1B,C**).

Examination of the dendrogram in **Figure 1B** and the UMAP plot in **Figure 1C** (as well as examining the successively parcelled UMAP clusters in **Figure 1–figure supplement 2B, E, and H** with increasing resolution) gives a sense of "relatedness" among clusters. For example, *Gad1/2-Tph2* clusters two to four are more similar to each other than to *Vglut3-Tph2* clusters, while cluster six, the *Gad1/2-Vglut3-Tph2* cluster, and cluster five are situated between the other *Gad1/2-Tph2* and *Vglut3-Tph2* groups. Like cluster twelve, clusters thirteen and fourteen appear as outliers from the other clusters in the dendrogram (**Figure 1B)**, but despite showing low and variable expression of the 5-HT neuron marker gene *Tph2*, respectively, they nonetheless cluster more closely to other *Pet1* neurons than do *Met-Vglut3-Tph2-Pet1* neurons (cluster twelve) in the UMAP plot (**Figure 1C)**.

Met-expressing *Pet1* neurons have been previously reported in mice, both at the transcript and protein levels, specifically in the caudal DR and the median raphe (MR) (Kast et al., 2017; Okaty et al., 2015; Wu and Levitt, 2013) and more recently (Huang et al., 2019; Ren et al., 2019). Likewise, *Vglut3*- and *Gad1/2*-expressing DR *Pet1* neurons have been previously reported in mice and rats, as demonstrated by mRNA *in situ*, immunocytochemistry, and RNA-seq (Amilhon et al., 2010; Commons, 2009; Fu et al., 2010; Gagnon and Parent, 2014; Gras et al., 2002; Herzog et al., 2004; Hioki et al., 2004; Hioki et al., 2010; Huang et al., 2019; Okaty et al., 2015; Ren et al., 2018; Ren et al., 2019; Rood et al., 2014; Shikanai et al., 2012; Spaethling et al., 2014; Voisin et al., 2016). Consistent with functional expression of VGLUT3, which allows for filling of synaptic vesicles with the excitatory neurotransmitter glutamate, depolarization-induced glutamate release by DR *Pet1*/5-HT neurons has been demonstrated by a number of

groups (Johnson, 1994; Kapoor et al., 2016; Liu et al., 2014; Sengupta et al., 2017; Wang et al., 2019). Additionally, VGLUT3 is thought to interact with vesicular monoamine transporter two (encoded by *Slc18a2,* alias *Vmat2* (Erickson et al., 1992)) to enhance the loading of 5-HT into synaptic vesicles by increasing the pH gradient across vesicular membranes, a process referred to as "vesicle-filling synergy" (Amilhon et al., 2010; El Mestikawy et al., 2011; Munster-Wandowski et al., 2016). GABA-release by *Pet1* DR neurons, on the other hand, has not been reported, thus the functional consequences of *Gad1* and *Gad2* transcript expression are presently unknown.

Differentially expressed genes span functional categories relevant to neuronal identity

Scaled expression of the top five marker genes for each cluster (ranked by p-value or in some cases fold enrichment) are represented in the heatmaps in **Figure 1–figure supplement 2C, F, I**, and **Figure 1D,** depending on the cluster resolution. To aid interpretation of the functional significance of differentially expressed genes, expression patterns of a subset of significantly variable genes and cluster markers (for the fourteen clusters resulting from a cluster resolution of 0.9) are represented in the dot plots in **Figure 2**, organized by categories of biological function (identified by Gene Ontology annotations and literature searches). These gene categories were selected based on general importance for shaping neuronal functional identity – e.g. genes that encode transcription factors which broadly regulate molecular phenotypes, as well as genes that encode ion channels, plasma membrane receptors, calcium-binding proteins, kinases, and cell adhesion and axon guidance molecules, which collectively govern neuronal electrophysiology, signal transduction, and synaptic connectivity.

Transcription Factors

History of expression of *Pet1/Fev,* encoding the FEV transcription factor, ETS family member (Fyodorov et al., 1998; Hendricks et al., 1999) defines the *Pet1* neuronal lineage. As can be observed from the transcription factor dot plot in **Figure 2** (as well as the violin plot in **Figure 1–figure supplement 3**), *Pet1/Fev* displays broad expression across clusters but is expressed at significantly lower levels in cluster thirteen *Pet1* neurons. Several genes known to be directly regulated by *Pet1* (Hendricks et al., 2003; Liu et al., 2010; Wyler et al., 2015; Wyler et al., 2016), such as *Tph2*, *Slc6a4/Sert* (encoding the serotonin transporter (Hoffman et al., 1991; Lesch et al., 1993)*,* and *Slc18a2/Vmat2* likewise show reduced expression in cluster thirteen. The transcription factor engrailed 1 (*En1*) (Joyner et al., 1985), in its expression overlap with *Pet1,* is a marker of having derived from progenitors in the isthmus and r1 (Alonso et al., 2013; Jensen et al., 2008; Okaty et al., 2015), and, as expected, *En1* transcripts are detected broadly across all DR clusters. The paralogous gene engrailed 2 (*En2*) (Joyner and Martin, 1987)*,* shows a more variable expression profile across *Pet1* DR neurons, being largely absent in cluster eight and twelve, and significantly lower in cluster seven. *En1* and *En2* are required for normal development of DR *Pet1* neuron cytoarchitecture and for perinatal maintenance of serotonergic identity (Fox and Deneris, 2012). *Nr3c1*, encoding the nuclear receptor subfamily 3, group C, member 1, aka the glucocorticoid receptor, which binds the stress hormone corticosterone (cortisol in humans), is expressed broadly across clusters one through eleven, but is de-enriched in cluster twelve, and to a lesser extent clusters thirteen and fourteen, suggesting differential sensitivity to corticosterone across different *Pet1* neuron molecular subtypes. Numerous studies have highlighted the functional importance of DR glucocorticoid signaling for 5-HT neuron activity and behavioral modulation (Bellido et al., 2004; Evrard et al., 2006; Judge et al., 2004; Laaris et al., 1995; Vincent et al., 2018; Vincent and Jacobson, 2014).

Other transcription factor encoding genes show more striking expression specificity. Transcripts for neuronal pas domain 1 and 3 (encoded by *Npas1* and

Npas3) and POU class 3 homeobox 1 (*Pou3f1*) are significantly enriched in cluster one *Pet1* neurons. From mouse genetic studies, both NPAS1 and NPAS3 are associated with regulation of genes and behavioral endophenotypes implicated in psychiatric disorders, such as schizophrenia, though NPAS1/3 are also expressed by other cell types in the brain, such as cortical interneurons, which may contribute to observed behavioral effects of *Npas1/3* loss of function (Erbel-Sieler et al., 2004; Michaelson et al., 2017; Stanco et al., 2014).

Pax5, encoding paired box 5 (Asano and Gruss, 1992), a transcription factor involved in the regulation of isthmic organizer activity during development (Funahashi et al., 1999; Ye et al., 2001) is significantly enriched in clusters two, four, and five, and highly expressed in clusters three and six as well. *Pou6f2* (POU class 6 homeobox 2) and *Klf5* (Kruppel like factor 5) show a similar pattern of expression. *Sox14* (SRY-box transcription factor 14) and *Satb2* (SATB homeobox 2) show an even more restricted expression profile, limited to clusters two through four. Notably, clusters two through six are also enriched for expression of *Gad2*, which, like *Sox14*, is most highly expressed in cluster four. *Sox14* expression has been shown to regulate GABAergic cell identity in the dorsal midbrain (Makrides et al., 2018), and *Pax5* expression has been implicated in GABAergic neurotransmitter specification in the dorsal horn of the spinal cord (Pillai et al., 2007), suggesting that these genes may play similar roles in DR *Pet1* neurons. Interestingly, *Nr2f2* (encoding nuclear receptor subfamily 2, group F, member 2, alias COUP-TFII) shows an expression profile that is complementary to *En2* and *Pax5,* enriched in cluster eight, nine, and twelve, all of which are enriched for *Vglut3* transcripts, and are largely devoid of *Gad1/2* expression.

Overall, each of the fourteen transcriptome-defined clusters of DR *Pet1* neurons can largely be classified by the combinatorial expression of two to three transcription factors. For example, *Pou3f2* (POU class three homeobox 2), *Bcl11a* (B cell CLL/lymphoma 11A zinc finger protein), and *Id2* (inhibitor of DNA binding 2) show enriched expression in cluster six, and to a lesser extent cluster

thirteen. Other notable transcription factor markers of *Pet1* neuron subgroups include *Foxp1* (forkhead box P1), enriched in clusters seven and fourteen, *Rorb* (RAR-related orphan receptor beta), enriched in cluster eight, *Maf* (avian musculoaponeurotic fibrosarcoma oncogene homolog), enriched in cluster nine, *Foxa1* (forkhead box A1), enriched in cluster eleven, *Zeb2* (zinc finger E-box binding homeobox 2) enriched in cluster twelve, *Zfp536* (zinc finger protein 536), *Nfix* (nuclear factor I/X), and *Nfib* (nuclear factor I/B), enriched in cluster thirteen (detected in cluster six as well), and *Ldb2* (LIM domain binding 2), enriched in clusters thirteen and fourteen.

Neurotransmitters and Neuropeptides

Pet1 neuron subtypes defined by transcriptomic clustering also show differential expression of a number of neurotransmitter-related and neuropeptide-encoding genes (**Figure 2** Neurotransmitters and Neuropeptides dot plot). Transcript profiles related to classic neurotransmitter production, including *Tph2, Gad2, Gad1,* and *Slc17a8,* have already been described above (see also **Figure 1B**). Transcript expression of *Trh*, encoding thyrotropin-releasing hormone, is significantly enriched in cluster two *Pet1* neurons and detected in clusters four and six (**Figure 1D** and **Figure2**). Another gene involved in thyroid hormone signaling, *Crym*, encoding crystalline mu, also known as NADP-regulated thyroid-hormone-binding protein shows a similar expression profile (**Figure 1D**). *Pdyn*, encoding the preprohormone prodynorphin is enriched in clusters five, six, and fourteen. Prodynorphin is the precursor protein to the opioid polypeptide dynorphin, which predominately binds the kappa-opioid receptor to produce a variety of effects, such as analgesia and dysphoria (Bruchas et al., 2010; Chavkin et al., 1982; Land et al., 2008; Land et al., 2009). Expression of *Nos1*, encoding nitric oxide synthase 1, is significantly enriched in cluster five, nine, and eleven. The anatomical distribution of nitric oxide expressing DR 5-HT neurons in rodents has been characterized previously as being predominately midline in the DR (Fu et al., 2010; Prouty et al., 2017; Vasudeva et al., 2011; Vasudeva and Waterhouse, 2014). Cluster nine also shows enriched expression of *Crh*,

encoding corticotropin-releasing hormone. Several other neuropeptide encoding genes show sporadic, significantly variable expression among different clusters, including growth hormone-releasing hormone (*Ghrh),* neuromedin B (*Nmb),* neuropeptide B (*Npb),* proenkephalin (*Penk),* and somatostatin (*Sst).*

Ionotropic and G-Protein Coupled Receptors

Cluster one and cluster thirteen *Pet1* neurons show the most prominent specificity with respect to ionotropic receptor markers (**Figure 2 Ionotropic Receptors**), though in general we found relatively few *Pet1* neuron subtype-specific ionotropic gene markers relative to other categories of gene function. *Gabrq* and *Gabre*, encoding GABA type A receptor subunits theta and epsilon, respectively, are significantly enriched in cluster one, as well as *Gria1,* encoding glutamate ionotropic receptor AMPA type subunit 1. GABA type A receptor subunit gamma3 (*Gabrg3*) and glutamate ionotropic receptor NMDA type subunit 2A (*Grin2a*) transcripts are largely de-enriched in clusters two through four and twelve, are significantly enriched in cluster nine, and variably expressed in other clusters. GABA A receptor subunit alpha 2 (*Gabra2*) is expressed in all clusters but is significantly enriched in cluster twelve, and GABA A receptor subunit alpha 1 (*Gabra1*) and glutamate ionotropic receptor AMPA type subunit 3 (*Gria3*) transcripts both show significant enrichment in cluster thirteen.

Transcripts encoding G protein-coupled receptors (GPCRs) show patterns of enrichment largely across blocks of clusters (e.g. *Vglut3*-expressing versus non-*Vglut3*-expressing *Tph2-Pet1* neurons), or highly specific enrichment in either cluster twelve or clusters thirteen and fourteen (**Figure 2 G Protein-coupled Receptors**). For example, cluster twelve neurons show strong enrichment for opioid receptor mu (*Oprm1*), purine receptor y1 (*P2ry1)*, relaxin receptor (*Rxfp1)*, sphingosine-1-phosphate receptor *3* (*S1pr3*), and tachykinin receptor 3 (*Tacr3)* transcripts. Moreover, they lack expression of transcripts for many GPCRs expressed by the majority of other *Pet1* neurons, such as presynaptic 5-HT autoreceptors, encoded by *Htr1b* and *Htr1d*, as well as orexin and histamine

receptors (e.g. *Hcrtr1*, *Hcrtr2*, *Hrh1*, *Hrh3*), whose protein products are involved in the regulation of arousal. We found that histamine receptor 1 (*Hrh1*) and hypocretin (alias orexin) receptor 1 (*Hcrtr1*) transcripts were the most abundant in clusters one through four, and histamine receptor 3 (*Hrh3*) transcripts were the most abundant in clusters two through six. Hypocretin receptor 2 (*Hcrtr2*) transcripts showed a somewhat complementary expression pattern, with the highest levels in clusters seven through eleven, as well as cluster three. Other GPCR transcripts with notable expression patterns are neuropeptide Y receptor Y2 (*Npy2r*), enriched in clusters seven and ten, cannabinoid receptor 1 (*Cnr1*) and 5-HT receptor 2C (*Htr2c*), enriched in clusters thirteen and fourteen, and *Gpr101*, an "orphan" GPCR thought to play a role in the growth hormone releasing-growth hormone signaling axis (GHRH-GH axis) (Trivellin et al., 2016; Trivellin et al., 2018), enriched in cluster fourteen.

Regulators of Neuron Projections, Synaptic Connectivity, and Heparan Sulfate Proteoglycans

Similar to transcription factor expression patterns, most DR *Pet1* neuron subgroups can be classified by combinatorial enrichment of transcripts for genes encoding regulators of neuron projections and synaptic connectivity (**Figure 2 Regulators of Neuron Projections and Synaptic Connectivity**). Differential expression of these genes likely contributes to differential innervation patterns of distinct DR *Pet1* neuron subgroups, such as reported by various studies (Fernandez et al., 2016; Huang et al., 2019; Kast et al., 2017; Muzerelle et al., 2016; Niederkofler et al., 2016; Ren et al., 2018; Ren et al., 2019; Teng et al., 2017), and yet to be uncovered. Genes encoding regulators of heparan sulfate proteoglycans may also play a role in projection specificity and synaptic organization (Condomitti and de Wit, 2018; Di Donato et al., 2018; Lazaro-Pena et al., 2018; Minge et al., 2017; Zhang et al., 2018), and likewise show patterns of enrichment across different *Pet1* neuron clusters (**Figure 2 Regulators of Heparan Sulfate Proteoglycans**). For example, transcript expression of heparan sulfate-glucosamine 3-sulfotransferase 4 (*Hs3st4*) is enriched across

clusters one through four, heparan sulfate-glucosamine 3-sulfotransferase 5 (*Hs3st5*) expression is significantly enriched in cluster ten (and expressed at high levels in clusters one, eight, nine, and eleven), and sulfatase 2 (*Sulf2*) and heparan sulfate-glucosamine 3-sulfotransferase 2 (*Hs3st2*) transcripts are enriched in cluster thirteen.

Intersectional genetic labeling of *Pet1* neuron subgroups in combination with histology and manual scRNA-seq reveals spatial distributions of DR *Pet1* neuron subtypes

Having identified transcriptomically distinct DR *Pet1* neuron subtypes in a largely unsupervised manner, we next sought to determine whether the cell bodies of these molecularly defined *Pet1* neuron subtypes show differential distributions within anatomical subfields of the DR. Using intersectional genetics to fluorescently label *Pet1* neuron subgroups defined by pairwise expression of *Pet1* and one of an assortment of identified subtype marker genes, we iteratively mapped molecular subtypes to anatomy in two ways – (1) using histology and microscopy to directly characterize cell body locations in fixed brain sections (**Figure 3**), and (2) performing manual scRNA-seq on labeled cells dissociated and hand sorted from microdissected anatomical subdomains of the DR, and comparing these expression profiles to our above described high-throughput scRNA-seq data (which we will refer to as our 10X scRNA-seq data) (**Figure 4**). We iteratively bred triple transgenic mice harboring (1) our *Pet1::Flpe* transgene, (2) one of two dual Flpe- and Cre- responsive reporter constructs (*RC::FrePe* or *RC*::*FL-hM3Dq*), and (3) one of five Cre-encoding transgenes (*Sert::cre*, *Vglut3::IRES-cre*, *Npy2r::IRES-cre*, *Crh::cre*, or *P2ry1::IRES-cre*), where *cre* expression is driven by either the endogenous promoter of the marker gene or by a gene-specific bacterial artificial chromosome (BAC). In selecting candidate markers from our list of differentially expressed genes, we sought gene drivers that could potentially divide *Pet1* neurons into subgroups at varying resolutions and were available as *cre* lines. Representative images for each triple transgenic genotype are given in **Figure 3** (organized by marker genes, columns A-E, at

different rostrocaudal levels of the DR, rows 1-6). For each genotype, the intersectionally defined subpopulation of neurons is labeled in green (i.e. history of Flpe and Cre expression) whereas the "subtractive" subpopulation is labeled in red (i.e. history of Flpe but not Cre expression).

Histology of Pet1-Intersectionally Defined Neuron Populations

High *Sert* expression, like high *Tph2* expression, defines *Pet1* neuron clusters one through eleven. Cluster twelve shows consistently lower mean expression of *Sert* transcripts (and to a lesser extent *Tph2* transcripts) than clusters one through eleven (**Figure 3A**), cluster fourteen shows a broader distribution of *Sert* transcript levels (**Figure 3A**) and most 5-HT markers (**Figure 1–figure supplement 3**), and cluster thirteen shows very low levels of *Sert* transcripts (**Figure 3A**) and other 5-HT markers (**Figure 1–figure supplement 3**). Consistent with the majority of profiled *Pet1* neurons expressing high levels of *Sert* and *Pet1* transcripts, we detected intersectional *Sert::cre;Pet1::Flpe* fluorescently marked neurons throughout the full rostrocaudal and dorsoventral extent of the DR (**Figure 3A1-A6**), however the subtractive population (presumably cluster thirteen and perhaps some cluster twelve and fourteen *Pet1* neurons) showed a more limited distribution. These subtractive (Flpe+ but Cre-) neurons were most conspicuously concentrated in the rostromedial DR (**Figure 3A2**), where only a few *Sert::cre;Pet1::Flpe* intersectional (Flpe+ and Cre+) neurons were intermingled. More caudally, the Flpe-only, subtractive neurons remained largely midline, but became more intermixed with the double-positive *Sert::cre;Pet1::Flpe* intersectionally marked cells. As another way of anatomically characterizing putative cluster thirteen *Pet1* neurons, we immunostained for TPH2 in *En1::cre;Pet1::Flpe;RC::FrePe* mice (the same genotype as used in some of our 10X scRNA-seq experiments), and found that the distribution of TPH2 immuno-negative *Pet1* neuron cell bodies showed a very similar distribution to the subtractive neurons (Flpe-only) in *Sert::cre;Pet1::Flpe;RC::FrePe* mice. (**Figure 3–figure supplement 1A-B**), further confirming the existence of *Pet1*-expressing neurons that do not express

TPH2 protein (Barrett et al., 2016; Pelosi et al., 2014). We consistently observed that these *Pet1::Flpe*-captured, TPH2-immunonegative neurons often have smaller cell soma and bipolar morphology (**Figure 3–figure supplement 1B**).

Vglut3-Pet1 expression defines *Pet1* neuron clusters seven through fourteen, and to a lesser extent cluster six (**Figure 3B**). We observed that *Vglut3::cre;Pet1::Flpe* intersectionally marked neurons show a strong ventromedial bias in rostral portions of the DR (**Figure 3B1-B3**), and are the predominant *Pet1* neuron subgroup in the more caudal midline DR (**Figure 3B3-B6**). By contrast, the subtractive *Pet1* neuron subgroup (presumably comprising *Pet1* neurons from clusters one through five and partly six) show a strong dorsal and lateral bias and are largely absent from the most caudal portions of the DR. We further characterized VGLUT3 protein expression in *Pet1* neurons by VGLUT3 immunohistology in *Vglut3::IRES-cre;Pet1::Flpe; RC*::*FL-hM3Dq* mice. We found consistent overlap between intersectional recombination marked neurons and VGLUT3 protein expression, especially in medial, ventromedial, and caudal portions of the DR (**Figure 3–figure supplement 1C-J**). In the dorsal and lateral portions of the DR, however, where there are far fewer intersectionally labeled neurons, we observed a small number of *Vglut3::cre;Pet1::Flpe* intersectionally marked neurons that were negative for VGLUT3 antibody staining, suggesting transient expression of *Vglut3* (and *Vglut3::IRES-cre)* by these cells at an earlier time in their developmental history (or low *Vglut3* expression sufficient to drive Cre expression, but not VGLUT3 immunodetection).

Transcripts for *Npy2r*, encoding the neuropeptide Y receptor 2, are strongly enriched in clusters six, seven, and ten, with less consistent expression in clusters eleven, thirteen, and eight, and only sporadic expression elsewhere (**Figure 3C**). In mid-rostral portions of the DR, we found that *Npy2r::cre;Pet1::Flpe* intersectionally marked cell bodies show a largely midline bias, with a greater density of cells ventrally than dorsally, and the occasional labeled cell body appearing more laterally (**Figure 3C2-C3**). In more caudal

extents of the DR, *Npy2r::cre;Pet1::Flpe* intersectionally marked cell bodies appear to be concentrated more medially (**Figure 3C4-C6**).

Transcripts for *Crh*, encoding corticotropin-releasing hormone, are most highly enriched in neurons comprising cluster nine and to a lesser extent cluster five, with sporadic expression in other clusters (**Figure 3D**). *Crh::cre;Pet1::Flpe* intersectionally labeled neurons do not show an obvious overall anatomical bias, distributing widely throughout the DR (**Figure 3D1-D6**). At the most rostral levels of the DR, they appear to be more consistently medially and ventrally localized (**Figure 3D1-D2**), but additionally appear in the dorsal and lateral DR at mid-rostral levels, and are preferentially localized off the midline more ventrally in these same sections (in regions sometimes referred to as the ventrolateral wings) (**Figure 2D3-D4**). At the most caudal levels they distribute dorsally and ventrally, with an apparent gap between these two domains (**Figure 3D5-D6**).

The most molecularly distinct *Pet1* neuron subtype we identified, cluster twelve *Met-Vglut3-Tph2-Pet1* neurons, shows highly specific enrichment for a number of transcripts, including *P2ry1*, encoding purinergic receptor P2Y1, which is only sporadically expressed in other clusters (**Figure 3E**). *P2ry1::cre;Pet1::Flpe* intersectionally marked neurons likewise show a strikingly unique anatomical distribution from the other subgroups examined, being largely restricted to the caudal DR where they are densely clustered dorsally, just beneath the aqueduct (**Figure 3E5-E6**). This is consistent with previous characterizations of *Met*-expressing *Pet1/*5-HT neurons (Okaty et al., 2015; Wu and Levitt, 2013), as well as other more recent characterizations (Huang et al., 2019; Kast et al., 2017; Ren et al., 2019). Notably the distribution of *P2ry1::cre;Pet1::Flpe* intersectional neurons within the cDR is distinct from *Npy2r:: cre;Pet1Flpe* intersectional neurons, and only partially overlaps with where *Crh::cre;Pet1::Flpe* intersectional neurons are found, arguing for *Pet1/*5-HT neuron subtype diversity within the caudal DR, consistent with (Kast et al., 2017).

559 It should be noted that the precise anatomical boundaries of the caudal DR
560 (cDR), also referred to as B6 (Dahlstroem and Fuxe, 1964; Jacobs and Azmitia,
561 1992)), are variably described in the literature. Alonso and colleagues divide B6
562 into dorsal and ventral sub-compartments, referred to as r1DRd and r1DRv,
563 respectively, where "r1" designates the putative developmental domain of origin
564 of *Pet1* neurons residing in this DR sub-region (i.e. originating from r1, as
565 opposed to isthmus)(Alonso et al., 2013). r1DRv likely corresponds to what
566 others have described as the caudal portion of the "interfascicular" DR (DRI), a
567 medioventral band of DR cells flanked on either side by the medial longitudinal
568 fasciculi. 5-HT neurons of the caudal DRI merge with the more dorsal B6 DR
569 sub-nucleus roughly at the level of the DR where dorsolateral 5-HT neurons
570 become sparse (coronal sections 5 and 6 in **Figure 3**) (Hale and Lowry, 2011;
571 Jacobs and Azmitia, 1992). Depending on the plane and angle of sectioning
572 these caudal DRI cells also appear to merge with MR 5-HT neurons more
573 ventrally, and it has been proposed that caudal DRI cells may be more similar to
574 MR 5-HT neurons developmentally, morphologically, and hodologically than to
575 DR 5-HT neurons (Commons, 2015, 2016; Hale and Lowry, 2011; Jacobs and
576 Azmitia, 1992). In the present study, our designation of cDR is inclusive of
577 r1DRd/r1DRv/caudal DRI/B6, as indicated in **Figure 4A**. Moreover, we do not
578 discount the possibility that this region as drawn partially overlaps with what
579 Alonso and colleagues would call the most dorsal portion of the caudal median
580 raphe (MnRc), as the boundary between the MnRc and r1DRv is poorly defined.
581 Thus, the territory between the cluster of *Met-Vglut3-Tph2-Pet1* neurons beneath
582 the aqueduct in the cDR and the MR is difficult to classify strictly based on
583 cytoarchitecture, underscoring the importance of alternative classification
584 schemes, such as offered by transcriptomics.

585 *Manual scRNA-seq of Pet1-Intersectionally Defined Neuron Populations*

586 Having mapped the spatial distributions of intersectionally labeled *Pet1* neuron
587 subgroups, next we wanted to explore the correspondence of molecular subtype
588 identity with DR subregions more comprehensively. To do this, we

589 microdissected subdomains of the DR in a subset of the intersectional mouse
590 lines just described, dissociated and sorted fluorescently labeled neurons,
591 harvested mRNA from single cells, and prepared scRNA-seq libraries (n = 70
592 single-cell libraries in total) using the SMART-Seq v4 kit, followed by Illumina
593 sequencing (**Figure 4A**). Specifically, we separately microdissected and
594 manually sorted *Sert::cre;Pet1::Flpe* intersectionally labeled neurons from the
595 dorsolateral DR (dl or dlDR, n = 10 cells), dorsomedial DR (dm or dmDR, n = 9
596 cells) ventromedial DR (vm or vmDR, n = 8 cells), and caudal DR (cDR, n = 6
597 cells), as schematized in **Figure 4A**. Additionally, we separately microdissected
598 and manually sorted *Npy2r::cre;Pet1::Flpe* intersectional neurons from the rostral
599 (rDR, n = 9 cells) versus caudal (n = 10 cells) DR, *P2ry1:: cre;Pet1::Flpe*
600 intersectional neurons from the cDR (n = 10 cells) , and *Crh::cre;Pet1::Flpe*
601 intersectional neurons from the rostromedial DR (n = 8 cells). We then used the
602 fourteen *Pet1* neuron subtype identities derived from our 10X scRNA-seq data as
603 a reference to “query” the corresponding identities of our manually sorted and
604 transcriptomically profiled single cells (using the Seurat functions
605 FindTransferAnchors and TransferData as described in (Stuart et al., 2019)). A
606 summary of this analysis is shown in the dot plot in **Figure 4B**. We found that the
607 majority of *Sert::cre;Pet1::Flpe* dlDR neurons mapped to cluster two, with a
608 smaller percentage of single cells mapping to clusters one, three, and six.
609 *Sert::cre;Pet1::Flpe* dmDR neurons were split between clusters two and three,
610 and to a lesser extent four, five, and nine. *Sert::cre;Pet1::Flpe* vmDR neurons
611 mostly corresponded to cluster ten, and were additionally mapped to clusters
612 one, four, seven, and thirteen (note, this may suggest that some *Pet1* neurons
613 expressing little or no *Sert* nor *Tph2* in the adult may yet express the *Sert::cre*
614 transgene). Finally, *Sert::cre;Pet1::Flpe* cDR neurons mapped exclusively to
615 clusters eight and seven (note, cluster twelve neurons do not appear to be well
616 marked by *Sert::cre;Pet1::Flpe;RC::FrePe* eGFP expression – see **Figure 3A5**
617 compared with **Figure 3E5** – perhaps reflecting the lower levels of *Sert*
618 transcripts detected in these neurons).

The majority of *Npy2r::cre;Pet1::Flpe* neurons in the rDR were found to correspond to cluster six, with additional mapping to clusters five, seven, ten, and thirteen (consistent with the expression profile of *Npy2r* transcripts in the 10X scRNA-seq data) whereas the majority of *Npy2r:: cre;Pet1::Flpe* neurons from the cDR were found to correspond to cluster seven, with a smaller percentage corresponding to clusters ten and fourteen. *P2ry1::cre;Pet1::Flpe* cDR manually sorted and profiled neurons were mapped exclusively to cluster twelve as expected. *Crh::cre;Pet1::Flpe* profiled neurons were split across clusters in a manner consistent with sporadic *Crh* expression in our 10X scRNA-seq data, however, we found more cluster three than cluster nine *Crh::cre;Pet1::Flpe* neurons, perhaps reflecting that our sampling of this population was biased towards rostromedial DR (or a potential discrepancy between endogenous *Crh* expression and *Crh::cre* expression). Finally, we also included *Drd2::cre;Pet1::Flpe* intersectional scRNA-seq data (n = 17 cells) associated with a previous study from our lab (Niederkofler et al., 2016). *Drd2::cre;Pet1::Flpe* intersectional neurons show a largely dorsolateral and dorsomedial bias within the DR. The majority of these neurons map to clusters three and four, with a much smaller percentage mapping to clusters eight and eleven.

Thus combining intersectional genetics, histological analyses, and precisely targeted manual scRNA-seq we were able to infer the anatomical distributions of our fourteen clusters (**Figure 4C**). Clusters one through six and eleven appear to be dorsally, laterally and rostrally biased (to varying degrees), clusters seven, eight, and twelve appear to be caudally biased (as well as cluster fourteen, to a lesser extent), and the remaining clusters appear to be more ventromedial biased in the more rostral DR. Moreover, *Pet1-Tph2*^{low} neurons (comprising cluster thirteen) show a prominent enrichment in the medial-rostral DR. Among caudal DR *Pet1* neuron clusters, cluster twelve shows a clear dorsal bias, whereas clusters seven and eight are likely more ventrally biased, based on **Figure 3A5-6, C5-6,** though a nontrivial degree of intermixing of different genetically defined *Pet1* neuron subpopulations in the dorsal cDR is apparent from these images.

Expression patterns of cluster marker genes showing strong anatomical biases in our manual scRNA-seq data are depicted in the dot plot in **Figure 4–figure supplement 1** in comparison with our 10X scRNA-seq data.

These inferred anatomical distributions of molecularly distinct *Pet1* neuron populations shed further light on the potential developmental significance of transcription factor expression patterns described above. As noted, *Pax5*, a gene associated with isthmic organizer activity during embryonic development (Funahashi et al., 1999; Ye et al., 2001), shows a complementary expression pattern to *Nr2f2*, which encodes a transcription factor that appears to be excluded from the isthmus, but is expressed in r1 and other rhombomeres during development, at least in zebrafish (Love and Prince, 2012). We further validated the anatomical expression profile of these genes, as well as *Satb2* (expressed by cluster two through four), at the level of protein expression by performing immunohistology in tissue sections prepared from *Vglut3::IRES-cre;Pet1::Flpe;RC*::*FL-hM3Dq* mice (**Figure 4–figure supplement 2 A-E**). Consistent with our anatomically-targeted, manual scRNA-seq data, PAX5 and SATB2 display a rostrodorsal bias in predominately non-*Vglut3*-expressing DR *Pet1* neurons (**Figure 4–figure supplement 2B-C,E**), whereas NR2F2 has a ventromedial and caudal expression bias in predominately *Vglut3*-expressing DR *Pet1* neurons (**Figure 4–figure supplement 2D,E**). Alonso and colleagues have proposed that cDR *Pet1* neurons are derived from r1 progenitors, whereas more rostral *Pet1* neurons are derived from isthmus (Alonso et al., 2013), however further fate-mapping experiments would be helpful to clarify isthmic versus r1-derived *Pet1* neuron populations (Okaty et al., 2019). Moreover, while rostral DR *Pet1* neurons may derive from isthmus and cDR *Pet1* neurons may derive from r1, our scRNA-seq data nonetheless show substantial *Pet1* neuron molecular heterogeneity within both DR domains, suggesting factors beyond isthmus and r1-lineage driving molecular diversity.

cDR *P2ry1::cre;Pet1::Flpe* neurons display unique hodological and electrophysiological properties

679 Having established correlations between DR *Pet1* neuron molecular expression
680 profiles and anatomical distribution of cell bodies, we next wanted to explore
681 corresponding differences in other cellular phenotypes. We chose to focus on
682 cluster twelve *Met-Vglut3-Tph2 Pet1* neurons, captured intersectionally by
683 *P2ry1::IRES-cre;Pet1::Flpe,* as they are the most distinct from other *Pet1*
684 neurons molecularly. To determine if these neurons are likewise unique from
685 other DR *Pet1* neurons with respect to other features we explored the
686 hodological and electrophysiology properties of *P2ry1::cre;Pet1::Flpe* neurons
687 using the intersectional expression of TdTomato (*RC::Ai65*). The anatomical
688 location of cell somata labeled in *P2ry1::IRES-cre;Pet1::Flpe;RC::Ai65* animals
689 was similar to that found in the previously characterized *P2ry1::IRES-*
690 *cre;Pet1::Flpe;RC::FrePe* mice, with a dense population of neurons directly under
691 the aqueduct in the cDR. In addition, there were slightly higher numbers of
692 intersectionally labeled cells in the rostral part of the dorsal raphe as well as
693 scattered cells in the median raphe, consistent with the sporadic expression of
694 *P2ry1* revealed by the present RNA-seq data and the scRNA-seq data of *Pet1*
695 neurons from the MR (Okaty et al., 2015; Ren et al., 2019). Strikingly, most fibers
696 from *P2ry1::cre;Pet1::Flpe;RC::Ai65* neurons were supra-ependymal and were
697 found throughout the third, lateral, and fourth ventricles, a property previously
698 attributed to 5-HT neurons within the cDR (Kast et al., 2017; Tong et al., 2014).
699 Sparser fibers were found in regions such as the lateral hypothalamus, medial
700 and lateral septum, olfactory bulb, lateral parabrachial nucleus and the
701 amygdala. To gain a better perspective of the extent of *P2ry1::cre;*
702 *Pet1::Flpe;RC::Ai65* fibers in the lateral ventricle we stained for
703 *P2ry1::cre;Pet1::Flpe;RC::Ai65* fibers on a flat mount of the lateral wall as
704 previously described (Mirzadeh 2010). *P2ry1::cre; Pet1::Flpe;RC::Ai65* fibers
705 were found on all aspects of the wall except for the adhesion area, including
706 regions that contain proliferating cells and migrating neuroblasts from the
707 subventricular zone (Mirzadeh et al., 2010)(**Figure 5**). Further,
708 *P2ry1::cre;Pet1::Flpe;RC::Ai65* fibers were closely apposed to proliferating cells
709 (Ki67+) and migrating neuroblasts (doublecortin, DCX+) within the subventricular

zone (SVZ) and within the rostral migratory stream (RMS) (**Figure 5**). The proximity of *P2ry1::cre;Pet1::Flpe;RC::Ai65* fibers to adult neural stem cells suggests that they may constitute a serotonergic population of neurons that regulate SVZ proliferation, a process known to be regulated by 5-HT levels and that has previously been associated with the cDR (Aghajanian and Gallager, 1975; Banasr et al., 2004; Brezun and Daszuta, 1999; Hitoshi et al., 2007; Kast et al., 2017; Lorez and Richards, 1982; Mirzadeh et al., 2010; Negoias et al., 2010; Siopi et al., 2016; Soumier et al., 2010; Tong et al., 2014).

We next characterized electrophysiological properties of *P2ry1::IRES-cre; Pet1::Flpe;RC::Ai65* neurons in comparison with other more broadly defined *Pet1* neuron subpopulations using whole-cell patch clamp in acute slice preparations. As comparison groups we chose: (1) "subtractive" *P2ry1::IRES-cre; Pet1::Flpe;RC*::*FL-hM3Dq* neurons in the cDR (i.e. cDR neurons with a history of *Pet1::Flpe* expression but not *P2ry1::IRES-cre* expression; we chose to use *RC*::*FL-hM3Dq* as opposed to *RC::Ai65* or *RC::FrePe* because the subtractive population is identifiable in acute brain slices by eGFP fluorescence without the need for secondary staining), and (2) *Gad2::IRES-cre;Pet1::Flpe;RC::Ai65* neurons from the more rostral and mostly dorsal DR (**Figure 6**). Recording from *P2ry1::IRES-cre;Pet1::Flpe;RC*::*FL-hM3Dq* subtractive cDR neurons allowed us to assess the degree to which electrophysiology may differ within a given DR subdomain depending on molecularly-defined neuron subtype, whereas *Gad2::IRES-cre;Pet1::Flpe;RC::Ai65* neuron recordings provided a comparison group that is both anatomically and molecularly distinct. As demonstrated in the F-I curves in **Figure 6A,** we found that *P2ry1::IRES-cre;Pet1::Flpe;RC::Ai65* neurons have dramatically lower excitability than the two comparison populations, requiring substantially more injected current to reach action potential threshold, and showing a roughly three-fold lower maximum firing rate. Even within the regime of current injection that *P2ry1::IRES-cre;Pet1::Flpe;RC::Ai65* neurons are excitable, we found that they displayed very different spiking characteristics from other *Pet1* neuron groups (Figure 6B-F), specifically showing

a longer latency to first action potential (AP, Figure 6D,F). Altogether, we observed four distinct firing types exemplified by the voltage traces displayed in **Figure 6B-E**: short-latency to first AP (regular spiking/non-adapting) (**Figure 6B**), mid-latency to first AP (**Figure 6C**), long-latency to first AP (**Figure 6D**), and short-latency to first AP with spike frequency adaptation (**Figure 6E**). The heatmap in **Figure 6F** shows the percentage of single-neuron recordings from each genotype that correspond to a given firing type. **Figure 6-figure supplement 1** displays differences in measured electrophysiological properties when cells are grouped by firing type, as opposed to genotype. All *P2ry1::IRES-cre;Pet1::Flpe;RC::Ai65* neurons recorded (twelve neurons from three animals) showed long latency to first AP, whereas only one out of nine subtractive neurons in the *P2ry1::IRES-cre;Pet1::Flpe;RC*::*FL-hM3Dq* cDR (from three animals) showed this phenotype and none of the *Gad2::IRES-cre;Pet1::Flpe;RC::Ai65* neurons (twelve neurons from two animals). These latter two groups of neurons showed greater heterogeneity with respect to firing characteristics, as might be expected given that labeled cells from both genotypes comprise multiple molecular subtypes identified by our scRNA-seq experiments. While the full extent of electrophysiological heterogeneity of these populations is likely under-sampled by the present dataset, the uniqueness of *P2ry1::IRES-cre;Pet1::Flpe;RC::Ai65* neurons nonetheless stands out.

Comparison to other DR scRNA-seq datasets

Recent scRNA-seq studies of mouse DR cell types have been published (Huang et al., 2019; Ren et al., 2019), reporting using either the InDrops platform to profile dissociated DR neurons (Huang et al., 2019) or fluorescence-activated cell sorting to purify dissociated Cre-dependent tdTomato-expressing *Sert::cre* neurons from mouse DR and MR, followed by SMART-Seq v2 library preparation and sequencing (Ren et al., 2019). Huang and colleagues identified six distinct *Pet1*-expressing DR neuron subtypes – five serotonergic and one glutamatergic – while Ren and colleagues identified seven *Pet1*-expressing serotonergic DR neuron subtypes (note they did not identify a glutamatergic *Tph2*^{low} group,

presumably because these neurons do not typically express *Sert::cre*). To directly compare our subtype classifications, we used the fourteen *Pet1* neuron subtype identities derived from our 10X scRNA-seq data as a reference to query the corresponding identities of the Huang and Ren datasets (using the Seurat functions FindTransferAnchors and TransferData, as described above for comparison with our manual scRNA-seq data). The results of this analysis are shown in the dot plot in **Figure 7**. Some *Pet1* neuron subgroup classifications were highly consistent across studies. For example, one hundred percent of single neurons making up the Huang 5-HT V and Ren cDR subgroups map to our cluster twelve *Pet1* neuron subgroup (*Met-Vglut3-Tph2-Pet1* neurons, corresponding to neurons intersectionally captured by *P2ry1::cre;Pet1::Flpe* expression in the cDR shown in **Figure 3E**). Likewise, there is high correspondence between Huang 5-HT I, Ren DR 1, and our cluster-two *Pet1*-neuron subgroup (dorsolateral DR *Gad2-Trh-Tph2-Pet1* neurons). Huang 5-HT II and Ren 2 subgroups are largely split between our cluster two and cluster three subgroups, with a smaller portion of each mapping to our cluster four subgroup (which also corresponds to a small subset of Huang 5-HT I and Ren DR 1 neurons). Huang 5-HT III and Ren DR 3 correspond to our cluster five and six subgroups, with a larger percentage of Huang 5-HT III neurons mapping to cluster five and a larger percentage of Ren DR 3 neurons mapping to cluster six.

In other cases, there is better correspondence between our identified *Pet1* neuron subgroups and one or the other study, likely due in part to technological differences between studies. For example, Huang Glu V corresponds well with our cluster thirteen *Pet1* neuron subgroup (*Vglut3-Tph2*^{low}*-Pet1* neurons) but very few neurons profiled in the Ren study map to cluster thirteen. As mentioned above, the absence of a prominent glutamatergic *Tph2*^{low} group of neurons in the Ren study likely stems from the fact that the low level of *Sert* transcription in these neurons does not reliably drive *Sert::cre* transgene expression and thus reporter expression for their cell sorting. However, the fact that a small number of *Sert::cre* expressing neurons from the Ren study do map to our cluster thirteen

subgroup indicates that there may be exceptions (moreover, these cells may more specifically map to cluster thirteen neurons at the higher end of the distribution of *Sert* and *Tph2* transcript levels **Figure 1–figure supplement 3**).

On the other hand, Ren DR 6 corresponds well with our cluster one subgroup (*Npas1/3-Tph2-Pet1* neurons) and Ren DR 4 corresponds well with our cluster nine subgroup (*Maf-Nos1-Tph2-Pet1* neurons), but there is no such one-to-one correspondence between these groups and the neuron groups identified in the Huang study. Rather, cluster one and cluster nine neurons get “pulled” from other groups identified by Huang. This likely reflects the different sensitivities of the various approaches. Specifically, our study and the Ren study achieved more than three-fold higher gene detection per single cell library on average than the Huang study, thus allowing for finer-scale molecular subgroup classification. However our higher single-cell sampling resolution – we profiled 2,350 DR *Pet1* neurons, whereas Huang and Ren each profiled roughly seven hundred DR *Pet1* neurons – ultimately allowed us to resolve more subgroups. Huang 5-HT IV and Ren DR 5 show the greatest degree of dispersion into different clusters identified in our study. Ren DR 5 is split predominately between clusters seven, ten, and fourteen, while Huang 5-HT IV is split into clusters ten and fourteen, as well as across several other clusters. Importantly, our higher number of identified clusters does not appear to stem from analytic differences between studies *per se*, given that we identified more clusters using a lower resolution parameter in our clustering analysis than the other two studies. Huang, et al. reported using a Seurat FindCluster resolution of 2.0, Ren, et al. used a resolution of 1.0, whereas the highest resolution we used was 0.9.

Lastly, we also found that Ren MR 1 (identified as being a median raphe 5-HT neuron subtype in that study) shows striking similarity to our cluster eight subgroup, which we have mapped to the cDR based on histology and our manual scRNA-seq data. As described above, the boundary between the cDR and the MR, specifically the portion of the MR attributed to r1-derived neurons (Alonso et al., 2013; Okaty et al., 2015), is poorly defined, thus Ren MR 1 and

our cluster eight neurons may indeed partially overlap anatomically. Notably, some Huang 5-HT IV neurons (microdissected from what was considered the DR in that study) also map to our cluster eight subgroup.

Discussion

The dorsal raphe nucleus is likely one of the most extensively connected hubs in the mammalian brain. Efferent DR fibers, predominantly serotonergic (but also glutamatergic and GABAergic), collectively innervate much of the forebrain and midbrain, as well as some hindbrain nuclei (Azmitia and Segal, 1978; Bang and Commons, 2012; Bang et al., 2012; Beaudet and Descarries, 1976; Fernandez et al., 2016; Gagnon and Parent, 2014; Hale and Lowry, 2011; Kast et al., 2017; Kosofsky and Molliver, 1987; Lidov et al., 1980; Lidov and Molliver, 1982; Maddaloni et al., 2017; McDevitt et al., 2014; Molliver, 1987; Muzerelle et al., 2016; O'Hearn and Molliver, 1984; Prouty et al., 2017; Ren et al., 2018; Steinbusch, 1981; Steinbusch et al., 1980; Vasudeva et al., 2011; Vertes, 1991; Vertes and Kocsis, 1994), and DR afferents have been identified from as many as eighty distinct anatomical brain regions, including other brainstem raphe nuclei (Celada et al., 2001; Commons, 2015; Goncalves et al., 2009; Levine and Jacobs, 1992; Mosko et al., 1977; Ogawa et al., 2014; Peyron et al., 1998; Peyron et al., 2018; Pollak Dorocic et al., 2014; Weissbourd et al., 2014). As such, the DR is hodologically poised to broadcast and receive signals related to a wide range of sensory, motor, affective, and cognitive processes. Indeed, DR neuropathology is associated with several human disorders (or disease models thereof) with broad symptomatology, such as major depressive disorder, autism, and Alzheimer’s disease (Chen et al., 2000; Dengler-Crish et al., 2017; Ellegood et al., 2015; Guo and Commons, 2017; Ji et al., 2020; Luo et al., 2017; Michelsen et al., 2008; Miyazaki et al., 2005; Simic et al., 2017; Vakalopoulos, 2017; Wang et al., 2018; Zweig et al., 1988). Outside of DR-specialist research, the DR has often been viewed by the wider neuroscience community as a “black box” source of a single neurochemical, namely 5-HT. Accordingly, development of therapeutics for associated disorders has largely focused on modulating overall

serotonergic tone. However, DR-focused research over several decades has revealed layers of functional complexity and compositional heterogeneity warranting a more nuanced view (reviewed in (Abrams et al., 2004; Andrade and Haj-Dahmane, 2013; Gaspar and Lillesaar, 2012; Hale and Lowry, 2011; Michelsen et al., 2007; Okaty et al., 2019; Vasudeva et al., 2011)). While these studies have reached into the black box of the DR and described a variety of features at different levels of observation, integration across levels to arrive at principles of DR organization has proved challenging. Elucidating how molecular, neurochemical, anatomical, hodological, electrophysiological, and functional descriptions of the DR overlap is essential to understanding the structure-function relationship of the DR and other raphe nuclei (Brust et al., 2014; Fernandez et al., 2016; Huang et al., 2019; Kast et al., 2017; Niederkofler et al., 2016; Okaty et al., 2015; Prouty et al., 2017; Ren et al., 2018; Ren et al., 2019), and will likely facilitate improved therapies for human disorders. Here we have focused on one broadly defined subgroup of DR cells – neurons that express the gene *Pet1/Fev* – and applied scRNA-seq, iterative intersectional genetics, histology, and slice electrophysiology to provide a transcriptomic and anatomic atlas of mouse DR *Pet1* neurons with examples of links between molecular, neurochemical, anatomical, hodological, and electrophysiological levels of description. We identify as many as fourteen distinct molecularly defined subtypes of *Pet1* neurons that show biased cell body distributions in DR sub-regions. We further characterize projections and electrophysiology of the most molecularly unique DR *Pet1* neuron subtype – *Met-Vglut3-Tph2-Pet1* cDR neurons (cluster twelve), genetically accessed by intersectional *P2ry1::cre;Pet1::Flpe* expression. The present study complements other recent characterizations of DR cell types (Huang et al., 2019; Ren et al., 2019), increasing the sampling resolution of *Pet1* neurons in particular through our experimental approach to achieve fine-scale identification of *Pet1* neuron subtypes.

Molecular and anatomic organization of Pet1 neuron subtypes

Our data and analysis highlight the hierarchical organization of DR *Pet1* neurons molecularly and anatomically, allowing for identification of features that organize *Pet1* neurons at different levels of granularity (**Figure 8**). Neurochemistry has long served as a principal phenotypic axis for classifying neurons, and concordantly we found that distributions of transcripts associated with distinct neurotransmitters correspond with broad subgroup divisions. The majority of *Pet1* neurons (clusters one through twelve) express high levels of *Tph2* mRNA, encoding tryptophan hydroxylase two, the rate-limiting biosynthetic enzyme for 5-HT, as well as several other genes indicative of a serotonergic phenotype, such as *Slc6a4* (*Sert*), *Slc18a2* (*Vmat2*), and *Maob*. However, we also identified two subgroups of *Pet1* neurons with 5-HT marker gene profiles that differ from the majority (clusters thirteen and fourteen). One subgroup (cluster thirteen) expresses very low transcript levels of 5-HT neuron marker genes, is mostly negative for TPH2 immunolabeling, and shows a biased cell body distribution in the rostromedial DR, as well as distributing sporadically throughout. The other subgroup (cluster fourteen) exhibits a much broader distribution of transcript levels for 5-HT marker genes than other groups. The functional significance of this variable expression can only be hypothesized at present; we speculate that it may reflect a capacity for neurotransmitter plasticity – i.e. experience-dependent induction or up-regulation of 5-HT phenotype, as hinted at by a recent study (Prakash et al., 2019). If this is the case, cluster fourteen neurons may be partially in transition, for example, from a predominately glutamatergic phenotype to a 5-HT phenotype or to a glutamate-5-HT co-transmitter phenotype. Both cluster thirteen and fourteen *Pet1* neuron subgroups express *Slc17a8* (*Vglut3*) transcripts, suggestive of a capacity for synaptic glutamate packaging and release, and show shared enrichment for several transcripts, including *Ldb2*, encoding the transcription factor LIM domain binding 2, and *Cnr1*, encoding cannabinoid receptor 1. Cluster fourteen is also uniquely distinguished by enrichment for *Gpr101* transcripts, encoding an orphan G protein-coupled receptor.

Among *Pet1* neurons expressing high levels of *Tph2* and other 5-HT gene markers, expression of genes related to GABA synthesis (*Gad1* and *Gad2*) or glutamatergic synaptic vesicle packaging (*Vglut3*) correlate with major molecular and anatomical subdivisions (evident in the dendrogram in **Figure 1B**, the UMAP plot in **Figure 1C**, and the histological image series in **Figure 3 B1-6 and Figure 3 – figure supplement 1D-J**). We found that the cell bodies of non-*Vglut3*, largely *Gad2*-expressing *Pet1* neurons are preferentially distributed in the dorsal and lateral sub-regions of the rostral DR, and become exclusively lateral and ultimately absent at more caudal extents of the DR. Conversely, *Vglut3-Tph2-Pet1* neuron bodies show a ventromedial bias rostrally and predominate the entire cDR. *Gad2-Tph2-Pet1* neurons and *Vglut3-Tph2-Pet1* neurons show differential enrichment of hundreds of transcripts, including *Pax5* and *Nr2f2*. Both genes encode transcription factors, the expression of which we examined through immunohistology and found a similar distribution of cell body staining as revealed by intersectional genetic labeling of *Vglut3::cre;Pet1::Flpe* neurons – *Pax5* expression overlaps predominately with the non-*Vglut3*-expressing population, whereas *Nr2f2* overlaps with the *Vglut3*-expressing population (**Figure 4 – figure supplement 2**). We also found one *Pet1* neuron subgroup (cluster six) that expresses *Gad1*, *Gad2*, and “intermediate” levels of *Vglut3* transcripts (relative to other *Vglut3*+ clusters). These neurons correspond with the rostral population of neurons labeled by intersectional *Npy2r::cre;Pet1::Flpe* expression (**Figure 3C**), which we characterized by manual scRNA-seq (**Figure 4**).

Altogether we identified five *Pet1* neuron subgroups that express *Gad1* or *Gad2* transcripts (clusters two through six), and found *Gad2* to be expressed more consistently and at higher levels than *Gad1* (with the exception of cluster six). *Gad1* and *Gad2* encode two distinct isoforms of glutamate decarboxylase, referred to as GAD67 and GAD65, respectively. In many neuron types, these proteins are often co-expressed, but localize to different subcellular compartments and differ in their interaction with the co-factor pyridoxol

phosphate (Chen et al., 2003; Erlander et al., 1991; Soghomonian and Martin, 1998). GAD65 (encoded by *Gad2*) is typically found in axon terminals where it is thought to play a role in GABA synthesis specifically for synaptic vesicular release, whereas GAD67 is typically localized to the soma and may be more involved with non-vesicular GABA release. While we did not reliably detect transcripts for the vesicular GABA transporter (*Slc32a1*), we did detect expression of transcripts encoding VMAT2 which has been shown to package GABA into synaptic vesicles in dopaminergic neurons, allowing for monoaminergic-GABAergic co-transmission (Tritsch et al., 2012). Thus it is plausible that *Gad2-Tph2-Pet1* neurons may likewise co-release GABA, though it has yet to be reported in the literature.

Beyond classic neurotransmitters, we also found enrichment of various peptide hormone transmitters in different *Gad2-Tph2-Pet1* neuron subgroups. Cluster two shows enrichment for thyrotropin-releasing hormone transcripts (*Trh*), and clusters five and six show enrichment for prodynorphin (*Pdyn*) (as does cluster fourteen). As can be seen in the dendrogram in **Figure 1B** and UMAP plot in **Figure 1C**, there appears to be a major division between *Gad2-Tph2-Pet1* clusters two through four and clusters five and six, with clusters five and six also sharing many molecular similarities with *Vglut3-Tph2-Pet1* subgroups. This may in part reflect differential expression of transcription factors that regulate divergent gene “modules”. While all *Gad2-Tph2-Pet1* neurons express *Pax5*, clusters two through four also express *Sox14* and *Satb2*. Cluster six, on the other hand, shows enrichment for several transcription factor genes that are also enriched (or trend towards enrichment) in clusters thirteen and fourteen, such as *Pou3f2*, *Bcl11a*, and *Id2*. These molecularly distinct *Gad2-Tph2-Pet1* subgroups also show differences in anatomy. Based on manual scRNA-seq of sub-anatomically targeted *Pet1* neurons, we found that cluster two *Gad2-Trh-Tph2-Pet1* neuron cell bodies are found predominately in the dorsolateral DR, as well as the dorsomedial DR, whereas clusters three, four, and five appear to be more dorsomedially biased, consistent with recent reports (Huang et al., 2019; Ren et

al., 2019). Cluster six neurons, as captured by *Npy2r::cre;Pet1::Flpe* expression, show a more diffuse distribution in the rostral DR, illustrating that not all *Pet1* neuron subtypes, as defined transcriptomically, correspond with clear-cut anatomical patterns. Indeed, while there are major differences between predominately dorsal versus ventral or rostral versus caudal DR *Pet1* neuron subtypes, different subtypes nonetheless intermix within these domains, emphasizing the importance of molecular-genetic targeting of *Pet1* neuron subtypes to gain specificity for functional characterization (a point also made by (Huang et al., 2019) and (Okaty et al., 2019)).

Vglut3-Tph2-Pet1 neuron subgroups, as noted above, are found more ventrally than *Gad2-Tph2-Pet1* neurons in the rostral DR, and are the dominant neurotransmitter phenotype in the caudal DR (as inferred by transcript expression and VGLUT3 and TPH2 immunostaining). We found two *Vglut3-Tph2-Pet1* neuron subtypes with cell bodies biased towards the rostral DR (clusters nine and ten) and three subtypes (clusters seven, eight, and twelve) biased towards the more caudal DR (as delineated in **Figure 4**, and see the discussion of varying nomenclature around the cDR in the **Results** section *Histology of Pet1-Intersectionally Defined Neuron Populations* above). Cluster twelve *Pet1* neurons, also marked by expression of the gene *Met*, we found to be the most different from all other *Pet1* neurons, both in terms of the number of differentially expressed genes and the magnitudes of enrichment/depletion compared to other *Pet1* neuron subtypes (as also observed by (Huang et al., 2019; Ren et al., 2019)). We show by histology of genetically marked neurons (intersectional *P2ry1::cre;Pet1::Flpe* expression) that the cell bodies of these *Met-Vglut3-Tph2-Pet1* neurons are clustered beneath the aqueduct in the caudal DR (Figure 3E) and send extensive axonal projections throughout the ventricles (Figure 5). Based on retrograde tracing experiments (Kast et al., 2017; Tong et al., 2014), it is likely that these neurons constitute the major source of 5-HT innervation to the ventricles. Furthermore, our demonstration that *P2ry1::cre;Pet1::Flpe* fibers are closely apposed with proliferating and migrating

cells in the SVZ and rostral migratory stream (**Figure 5**), supports a proposed role for these neurons in regulating adult neural stem cell proliferation in the SVZ (Tong et al., 2014). Cluster twelve neuron transcript enrichment for several GPCRs implicated in modulation of adult neurogenesis, such as *P2ry1* (Lin et al., 2007), *Gipr* (found to be enriched in our *P2ry1::cre;Pet1::Flpe* manual scRNA-seq data) (Nyberg et al., 2005), *S1pr3* (Alfonso et al., 2015; Ye et al., 2016), and *Oprm1* (Harburg et al., 2007) lends further support to this hypothesis. Now, with intersectional access to this population of cDR 5-HT neurons provided by *P2ry1::IRES-cre* with *Pet1::Flpe,* the function of *Met-Vglut3-Tph2-Pet1* cDR neurons in regulating SVZ proliferation can be tested directly in a cell type-specific manner using dual Cre- and Flpe- responsive chemo- or optogenetic approaches (Brust et al., 2014; Hennessy et al., 2017; Kim et al., 2009; Madisen et al., 2015; Niederkofler et al., 2016; Okaty et al., 2015; Ray et al., 2011; Sciolino et al., 2016; Teissier et al., 2015).

DR *Pet1* neuron subtypes have distinct electrophysiological properties

To further characterize correspondence of molecular identities with other cell phenotypes we performed whole-cell electrophysiological recordings in acute slices prepared from mice in which different *Pet1* neuron subsets were genetically labeled. We found that 5-HT neurons with different molecular identities also exhibit distinct electrophysiological properties likely to impact their circuit function. While we did not comprehensively sample all molecularly defined subtypes, our survey of cDR *Pet1* neurons and rostrodorsal *Gad2::cre;Pet1::Flpe* neurons provides evidence for at least four distinct electrophysiological types based on four key properties: (1) rheobase (also known as current threshold), which reflects a neuron's sensitivity to input, (2) delay to first spike, which reflects the degree to which a neuron is able to activate phasically in response to input, (3) spike-frequency adaptation, which reflects the degree to which a neuron is able to continuously signal ongoing input, and (4) maximum firing rate, which determines the dynamic range of neuron responsiveness to graded inputs. As with molecular differences, cluster twelve *Met-Vglut3-Tph2-Pet1* cDR neurons

(*P2ry1::cre;Pet1::Flpe* intersectional expression) showed profound differences from other subtypes, including other cDR *Pet1* neurons. *P2ry1::cre;Pet1::Flpe* neurons consistently displayed a long latency to first action potential, required substantially more input to reach action potential threshold, and had a lower maximum firing rate (**Figure 6 and Figure 6 – figure supplement 1**). These differences, together with differential transcript expression of several GPCRs, suggest that *Met-Vglut3-Tph2-Pet1* cDR neurons respond in a different way and to very different stimuli than other DR *Pet1* neuron types. For example, low excitability and long-latency to spike suggest that these neurons may only be recruited by very strong stimuli at relatively slower timescales than other *Pet1* neurons (to the extent that properties recorded in slice reflect *in vivo* properties). Notably, 5-HT neurons with this electrophysiological profile have not yet been reported in the literature. However, the two firing types that we have defined as "Short-Latency to First AP; Non-Adapting" and "Mid-Latency to First AP" (**Figure 6B,C**) correspond well to those described by (Fernandez et al., 2016) in groups of *Pet1-eGFP* serotonergic neurons projecting to the mPFC and the BLA, respectively. Differential expression of Ion channels and receptors identified here suggest molecular substrates of these different electrophysiological properties.

Technical aspects of our study allow for high-resolution transcriptome characterization of *Pet1* neurons

Due to the high-dimensional "richness" of transcriptomic data, together with the capacity to propose explanations of cellular phenotypes in terms of molecular mechanisms – RNA-seq dissection of neural circuits has gained traction as a way to define and enumerate cell types in the brain (and other tissues). Single-cell RNA-sequencing, in particular, has become an indispensable approach, with different methods achieving different resolution of underlying cellular diversity (Bakken et al., 2018; Campbell et al., 2017; Hodge et al., 2019; Huang et al., 2019; Lovatt et al., 2014; Macosko et al., 2015; Okaty et al., 2015; Poulin et al., 2016; Ren et al., 2019; Rosenberg et al., 2018; Saunders et al., 2018; Spaethling et al., 2014; Tasic, 2018; Tasic et al., 2016; Tasic et al., 2018; Usoskin et al.,

2015; Zeisel et al., 2018; Zeisel et al., 2015). Droplet-based scRNA-seq approaches (without cell-type-specific purification) allow for unbiased classification of major cell types residing in a particular microdissected tissue region of interest, however lower abundance cell types, such as DR *Pet1* neurons profiled in the present study, are often insufficiently sampled to achieve high resolution of subtype molecular diversity. Moreover, different reaction chemistries employed in different droplet-based scRNA-seq approaches can lead to different gene detection sensitivity. Low cellular abundance compounded with low gene detection can greatly limit the power of a study to reveal fine-scale variation in molecular phenotypes that may be important for identifying neuronal subtypes and subtype “states” (e.g. adaptive or pathological transcriptional variation). Where cell type-specific markers are available, cell sorting prior to scRNA-seq library preparation can greatly enhance the resolution of cellular diversity for less abundant cell classes. While manual sorting approaches combined with RNA-seq library preparation optimized for low amounts of input RNA achieve high single-cell gene detection and allow for sampling genetically and anatomically-defined neuron populations (Niederkofler et al., 2016; Okaty et al., 2015), they are often limited in the number of cells profiled, and therefore may lack sufficient throughput to fully characterize subtype diversity. On the other hand, automated sorting approaches achieve greater throughput but are less well suited to collecting low abundance cell types, such as defined by fine-scale anatomy or highly restricted marker gene expression. Our particular experimental approach to characterizing DR *Pet1*-lineage neuron diversity in the present study was informed by all of the above concerns. By combining intersectional genetic labeling of DR *Pet1* neurons with both high-throughput (On-chip microfluidics) and targeted low-throughput (manual) sorting approaches, followed by high-sensitivity RNA-seq library preparation protocols (10X Genomics Chromium Single Cell 3’ v3 and SMART-Seq v4 kits, respectively) we leveraged the strengths of multiple approaches to achieve high-resolution transcriptomic profiling of DR *Pet1* neurons.

Resource value of DR Pet1 neuron scRNA-seq data

While we have highlighted many salient experimental findings in the present report, the data no doubt have more to reveal, and we thus offer this dataset as a resource to be mined by the larger community in the hopes that it may facilitate and stimulate future studies (**GEO accession number pending**). For example, newly identified *Pet1* neuron subtype marker genes may guide development of new recombinase driver lines allowing for subtype-specific genetic access, or shape approaches for developing more targeted therapeutics. Moreover, we hope this work, together with other recent studies (Huang et al., 2019; Ren et al., 2019), may lead to the development of a standardized DR *Pet1* neuron subtype nomenclature that allows for consolidation of results across different labs and different data modalities.

Methods

Intersectional genetic fate mapping

Triple transgenic mice were generated by crossing *Pet1::Flpe; FrePe* (Brust et al., 2014; Jensen et al., 2008; Okaty et al., 2015) or *Pet1::Flpe; Ai65* (Madisen et al., 2015) mice with *Sert::*cre (Gong et al., 2007), *Npy2r::IRES-cre* (Chang et al., 2015), *En1::cre* (Kimmel et al., 2000), *Crh::cre* (https://www.mmrrc.org/catalog/sds.php?mmrrc_id=30850), and *P2ry1::IRES-cre* (Chang et al., 2015) mice, or by crossing *Pet1::Flpe; hM3Dq* (Sciolino et al., 2016) mice with *Vglut3::IRES-cre* mice (https://www.jax.org/strain/028534).

Perfusion and immunohistochemistry

Anesthetized mice were transcardially perfused with cold phosphate-buffered saline (PBS) followed by 4% paraformaldehyde (PFA) overnight. Tissue was dissected and fixed in 4% PFA overnight followed by cryoprotection in 30%

sucrose/PBS until equilibrated (~48 hours) before being frozen in tissue freezing medium (Triangle Biomedical Services). Tissue was cryosectioned in 40um coronal sections and processed as floating sections.

For fluorescent staining, sections were washed with PBS and PBS with 0.1% Triton-X-100 (PBS-T), blocked in 5% normal donkey serum (NDS) and 1% bovine serum albumin (BSA) for 2 hours at room temperature (RT), and incubated with primary antibody at 4°C for 48 hours: anti-GFP (1:3000, chicken polyclonal, Aves Labs, GFP-1020), anti-DsRed (1:1000, rabbit polyclonal, Takara, 632496), anti-TPH2 (1:1000, rabbit polyclonal, Novus Biologicals, NB100-74555), anti-Pax5 (1:1000, goat polyclonal, Santa Cruz, sc-1974), anti-SATB2 (1:1000, guinea pig polyclonal, Synaptic Systems, 327-004), anti-COUP-TFII (1:1000, mouse monoclonal, Perseus Proteomics, PP-H7 147-00), anti-ZEB2 (1:200, rabbit polyclonal, MyBioSource, MBS9601451), anti-VGLUT3 (1:500, guinea pig polyclonal, Synaptic Systems, 135-204), anti-RFP (1:500, rat monoclonal, Chromotek, 5f8-100), anti-Doublecortin (1:1000, goat polyclonal, Santa Cruz, SC-8066), and anti-Ki-67(1:1000, rat monoclonal, Invitrogen, 14-5698-80). For fluorescent detection, sections were washed in PBS-T and incubated with species matched secondary antibodies- Alexa Fluor 488 (donkey anti-chicken, Jackson, 703-545-155), Alexa Fluor 546 (donkey anti-rabbit, Invitrogen, A10040), Alexa Fluor 647 (donkey anti-goat, Invitrogen, A21447 or donkey anti-mouse, Jackson, 715-605-151), and Cy5 (donkey anti-guinea pig, Jackson, 706-175-148)- at 1:500 dilution for two hours. Sections were washed in PBS and 1:3000 DAPI before rinsing and mounting onto slides.

Confocal and fluorescent microscopy and quantification

Overview images**:** Overview images of intersectional subtypes were acquired using a 5x objective on a Zeiss Axioplan2 fluorescence microscope equipped with an Axiocam digital camera and Axiovision software using 1x1 binning. Images were then cropped to a 1000x1000 pixel square containing the dorsal raphe. Images showing the distribution of PAX5, SATB2, and NR2F2 are 2x2

tiled maximum intensity images acquired using a Plan Apo λ 20x/0.75 DIC I objective on a spinning disk confocal. Images showing TPH2 and VGLUT3 staining are a single optical slice taken on a spinning disk confocal using a Plan Apo λ 20x/0.75 DIC I objective or Plan Fluor 40x/1.3 Oil DIC H/N2 objective respectively. Images were cropped to create a zoomed image of the region of interest.

Quantification: Quantification of PAX5, NR2F2, and SATB2 was completed in *Vglut3::IRES-cre; Pet1::Flpe; hM3Dq* animals, where cells expressing both *Vglut3::IRES-cre* and *Pet1::Flpe* express an hM3Dq-mCherry fusion and all other *Pet1*+ cells express eGFP. Images were acquired as 2x2 tiles as a z-stack (0.9um step) using a Plan Apo λ 20x/0.75 DIC I objective on a spinning disk confocal and cropped into equally sized non-overlapping subregions (1000x1000 pixel) spanning the rostral to caudal extent of the dorsal raphe. Cells were counted positive if antibody staining for the protein of interest overlapped with DAPI staining and was within a DsRed + cell (*Vglut3::cre;Pet1::Flpe* lineage) or a GFP+ cell (subtractive *Pet1* lineage). All counts were completed in images taken from 2 to 4 animals depending on the brain region. Images used for the quantification of VGLUT3 antibody staining were acquired using a Plan Fluor 40x/1.3 Oil DIC H/N2 objective on a spinning disk confocal on non-overlapping anatomical subdivisions of the dorsal raphe. Cells were counted positive based on the overlap of VGLUT3 antibody staining with mCherry (*VGlut3::cre;Pet1::Flpe* lineage) or a eGFP (subtractive *Pet1* lineage) staining. In the case of TPH2 quantification, *En1::cre; Pet1::Flpe; FrePe* animals were used (eGFP+ *En1::cre; Pet1::Flpe* intersectional lineage cells). Images were acquired as 2x2 tiles as a z-stack (0.9um step) using a Plan Apo λ 20x/0.75 DIC I objective on a spinning disk confocal and cropped into equally sized non-overlapping subregions (1000x1000 pixel) spanning the rostral to caudal extent of the dorsal raphe. Cells were counted positive based on colocalization of TPH2 antibody staining with eGFP. All quantification was performed by an experienced

observer blinded to the anatomical region of the image in a minimum of two animals per region.

Flat mount of lateral wall of lateral ventricle: *P2ry1::IRES-cre; Pet1::Flpe; Ai65* mice (n=4) were transcardially perfused with cold PBS. Lateral wall dissection was completed as described in Mirzadeh, et.al, 2010. Briefly, brains were dissected into PBS and split into two hemispheres. The hippocampus was removed, exposing the lateral wall, and the brain was fixed overnight in 4% PFA in PBS. The remainder of the microdissection of the lateral wall was then completed and immediately proceeded to immunohistochemistry as described above.

Single-cell sorting and RNA sequencing

OnChip Sorting, 10X library preparation, and RNA sequencing: Data was derived from two different experiments composed of brain tissue harvested from *En1::cre; Pet1::Flpe; FrePe* mice (n=4) or *Pet1::Flpe; RC::FL-hM3Dq* mice (n=6). Tissue was sectioned on a vibratome and protease-digested in ACSF containing activity blockers as described in (Hempel et al., 2007). The dorsal raphe was micro-dissected under an upright dissection microscope with fluorescence optics and all tissue was combined in a 1.5mL Eppendorf tube containing 500ul of filtered ACSF/1%FBS. Tissue was then gently triturated using glass micropipettes of decreasing diameter until achieving a mostly homogeneous single-cell suspension without visible tissue chunks. One drop of NucBlue (Thermo Fisher Scientific) was added to the cell suspension and allowed to sit for 20 minutes (to aid in sorting and cell quantification). The cell suspension was then loaded onto a microfluidic chip and eGFP-marked, NucBlue-positive cells were sorted using an OnChip sorter (OnChip Biotechnologies Co.). Final cell concentration was determined by counting the number of cells in 10ul of the sorted output using a hemacytometer. Cells were then run through the 10X Genomics Chromium Single Cell 3' v3 protocol, and libraries were sequenced on an Illumina NextSeq 500 sequencer to a mean depth of ~115,000 reads per cell.

Manual Sorting and RNA sequencing: Brain tissue was harvested from triple transgenic animals – *Sert::cre;Pet1::Flpe;FrePe*, *Npy2r::IRES-cre Pet1::Flpe;FrePe, Crh::cre;Pet1::Flpe;FrePe,* and *P2ry1::IRES-cre* (p60-p120, a minimum of two mice per condition) and fluorescently labeled cells were sorted as described in (Okaty et al., 2015). Briefly, the brainstem was sectioned into 400um coronal sections using a vibratome. Sections were bubbled in artificial cerebrospinal fluid (ACSF) containing activity blockers for at least 5 minutes before being transferred to ACSF containing 1mg/ml pronase for 1 hour. Slices were then returned to protease-free ACSF for 15 minutes, before regions of interest were micro-dissected. Anatomical subdivisions of the dorsal raphe were made based on the shape of the dorsal raphe and landmarks including fiber tracts and the aqueduct (as indicated in **Figure 4A**). Dissected chunks of tissue were transferred first to a clean 35-mm dish containing ACSF and then to a 1.5mL Eppendorf tube containing 1mL of filtered ACSF/1% FBS. Tissue was then gently triturated until without visible chunks. Dissociated cells were diluted and poured into a Petri dish. Fluorescently marked cells were aspirated using mouth aspiration and moved into 3 consecutive wash dishes. Each cell was then aspirated a final time and deposited into an individual 0.5mL tube containing 9.5ul of nuclease-free water and 1ul of 10x Reaction Buffer (Smart-Seq V4 Ultra Low Input RNA kit, Takara Bio) and allowed to incubate at room temperature for 5 minutes before being stored at -80deg until cDNA synthesis. Single cells were converted to cDNA and amplified using Smart-Seq V4 Ultra Low Input RNA Kit (Takara Bio). The cDNA output was then processed with Nextera XT DNA Library Preparation Kit. Quantification and quality control were assessed with TapeStation. Libraries were then sequenced on either an Illumina HiSeq 2500 (50 base-pair, single-end) or NextSeq 500 (75-bp, paired-end) to a mean depth of ~4,000,000 reads per cell.

scRNA-seq Analysis

10x scRNA-seq data: Transcriptome mapping (using the mm10 genome assembly) and demultiplexing were performed using the 10X Genomics Cell

Ranger software (version 3.0.2). Several data-filtering steps were performed on the matrix of transcript counts (using R version 3.5.3) prior to further analysis. First, we filtered out all genes detected in fewer than ten single-cell libraries, and filtered out all libraries with less than 4,500 detected genes. This threshold was selected based on the histogram of gene detection for all single-cell libraries as initially called by the Cell Ranger cell detection algorithm, which appeared to reflect two different distributions corresponding to low-complexity versus high-complexity libraries. The low-complexity distribution was right-skewed and had a mode of less than 1,000 detected genes, whereas the high-complexity distribution was left-skewed and had a mode of ~7,500 detected genes. 4,500 genes was roughly the boundary between the two distributions; i.e. the minima between the two modes, and also corresponded to a sharp inflection point in the Barcodes versus UMI counts plot in the web_summary.html file generated by Cell Ranger. While many of these low-complexity libraries may have been misidentified as cells by Cell Ranger (e.g. droplets containing transcripts from lysed cells, rather than intact cells) examination of genes enriched in lower-complexity libraries suggested that some of them reflected unhealthy cells (e.g. libraries with high mitochondrial gene expression) or contaminating non-neuronal cells (e.g. libraries enriched for glial marker genes). Notably, the number of cells with high-complexity libraries corresponded well with our estimated number of eGFP positive cells used as input to the 10X chip. We further excluded libraries with: (1) evidence of glial contamination, based on high-outlier expression of glial marker genes, including *Plp1*, *Olig1*, and *Aqp4*, (2) absence or low-outlier levels of *Pet1/Fev* transcripts, (3) greater than fifteen percent of detected genes corresponding with mitochondrial genes, (4) less than two percent of detected genes corresponding with ribosomal genes (these appeared to be single-nuclei libraries, rather than single-cell), (5) high-outlier UMI counts, and (6) high-outlier gene detection. 2,350 single-cell libraries and 17,231 genes passed the above filtering criteria.

Next, we created a Seurat object using these filtered data (Seurat version 3.0.2). Data were log-normalized using the NormalizeData function (using the default scale factor of 1e4), and we identified the top two thousand genes (or in some cases non-coding RNAs) with the most highly variable transcript expression across single cells using the FindVariableFeatures function (selection.method = "vst", nfeatures=2000). We then scaled and centered the log-normalized data using the ScaleData function and carried out principal components analysis (PCA) on the scaled expression values of the two thousand most highly variable genes. This allowed us to reduce the dimensionality of the data onto a smaller set of composite variables representing the most salient gene expression differences across single neurons. The procedure for identifying meaningful *Pet1* neuron subtype clusters is thoroughly described in the Results section of the main text. Briefly, we systematically varied the number of principal components included and the resolution parameter in the functions FindNeighbors, FindClusters, and RunUMAP, Dendrograms were created using BuildClusterTree and PlotClusterTree, and cluster-enriched genes were identified using the FindAllMarkers function, with min.pct = 0.25 and logfc.threshold = 0.25, using Wilcoxon Rank Sum tests.

Manual scRNA-seq data: Transcript mapping to the mm10 genome assembly and feature counts were performed using STAR (version 2.5.4) (Dobin and Gingeras, 2016). Given the high purity of manual cell sorting and the high sensitivity of SMART-Seq v4 cDNA amplification, no data filtering was required; i.e. single-cell libraries showed no evidence for off-target contamination and showed consistently high gene detection (~9,000 genes per single-cell). Counts data were analyzed using Seurat as described for 10X scRNA-seq data.

Transfer of 10X cell type labels: In order to explore the correspondence between the fourteen 10X scRNA-seq data-defined *Pet1* neuron subtypes and other scRNA-seq data, including our manual scRNA-seq data, and the Huang, et al. 2019 and Ren, et al. 2019 datasets, we employed the strategy outlined in (Stuart et al., 2019). Specifically, we used the Seurat functions FindTransferAnchors and

TransferData, using the 10X data as the “reference” and the other datasets as the “query” group.

Electrophysiology methods

In vitro brainstem slice preparations containing dorsal raphe serotonin neurons were obtained from 4-5 week old mice. After isofluorane anesthesia, mice were perfused transcardially with a solution of artificial CSF ($NaHCO_3$-aCSF) containing the following (in mM): 124 NaCl, 25 NaHCO3, 3 KCl, 2 CaCl2, 2 $MgCl_2$, 1.2, NaH2PO4 and 25 d-Glucose, equilibrated with 95% O2 and 5% CO2 adjusted to 310 ± 5 mOsm/L. The brainstem was dissected and mounted on the stage of a VT1200S vibratome while immersed in an ice slush solution aCSF containing the following (in mM): NMDG 93, HCl 93, KCL 2.5, NaH_2P0_4 1.2, $NaHCO_3$ 30, HEPES 20, d-Glucose 25, Na-Ascorbate 5, Thiourea 2, Na-Pyruvate 3, $MgSO_4$ 10, $CaCl_2$ 0.5 equilibrated with 95% O2 and 5% CO2 adjusted to 310 ± 5 mOsm/L. Coronal slices 200 µm thick containing the dorsal nucleus raphe were recovered for 1h at 35-6 C in HEPES-aCSF containing: NaCl 92, KCl 2.5, NaH_2P0_4 1.2, $NaHCO_3$ 30, HEPES 20, Glucose 25, Na-Ascorbate 5, Thiourea 2, NaPyruvate 3, $MgSO_4$ 10, $CaCl_2$ 0.5 equilibrated with 95% O2 and 5% CO2 adjusted to 310 ± 5 mOsm/L and placed at room temperature for storage. Individual slices were transferred to the recording chamber and superfused with NaHCO3-aCSF at 34ºC. Electrodes (5–7 MΩ) were pulled from borosilicate glass. Pipettes were filled with (in mM): 140 K-gluconate, HEPES 10, KCl 5, Na-ATP 2, $MgCl_2$ 2, EGTA 0.02, biocytin 0.1% Na_2GTP 0.5, Na_2-phosphocreatine 4, pH 7.4 adjusted with KOH and adjusted to 285 ± 5 mOsm/L with sucrose. Somatic whole-cell recordings were obtained with a Multiclamp 700B amplifier, signals were acquired and sampled at 100 kHz using Digidata 1440A digitizing board. Pipette capacitance was compensated ≈70% in current clamp (CC). Series resistance (*R*s) was typically 9–15 MΩ. Cells with *R*s > 15 MΩ were discarded. A measured liquid junction potential of ≈10 mV was corrected online. Cells were held at V_h= -80 mV unless otherwise indicated. To create action potential frequency-current curves, a protocol that applies a series

of 750 ms current pulses ranging from -100 pA to 220 pA was created using Molecular Devices Clampex 10.7 software running on Windows 7.

Acknowledgments

The authors thank the Biopolymers Facility at HMS for assistance with next-generation sequencing; the Microscopy Resources on the North Quad (MicRoN) core at Harvard Medical School for microscope use; Steve Liberles for providing *Npy2r::IRES-cre* and *P2ry1::IRES-cre* driver lines; ChangHee Lee and Jin Akagi for advice with On-Chip sorting; the Dymecki lab for discussions and thoughtful comments on this manuscript; J.J Mai for reagents and animal husbandry. Grants supporting this work include NARSAD Young Investigator Grant (BWO, SMD), NIDA Grant RO1DA034022 (BWO,SMD), T32 HL 007901 (NS), and the GVR Khodadad Fund for the Study of Genetic, Neurobiological, and Physiochemical Processes of EPS (BWO,SMD).

References

Abrams, J.K., Johnson, P.L., Hollis, J.H., and Lowry, C.A. (2004). Anatomic and functional topography of the dorsal raphe nucleus. Ann N Y Acad Sci 1018, 46-57.

Aghajanian, G.K., and Gallager, D.W. (1975). Raphe origin of serotonergic nerves terminating in the cerebral ventricles. Brain Res 88, 221-231.

Alfonso, J., Penkert, H., Duman, C., Zuccotti, A., and Monyer, H. (2015). Downregulation of Sphingosine 1-Phosphate Receptor 1 Promotes the Switch from Tangential to Radial Migration in the OB. J Neurosci 35, 13659-13672.

Alonso, A., Merchan, P., Sandoval, J.E., Sanchez-Arrones, L., Garcia-Cazorla, A., Artuch, R., Ferran, J.L., Martinez-de-la-Torre, M., and Puelles, L. (2013). Development of the serotonergic cells in murine raphe nuclei and their relations with rhombomeric domains. Brain Struct Funct 218, 1229-1277.

Amilhon, B., Lepicard, E., Renoir, T., Mongeau, R., Popa, D., Poirel, O., Miot, S., Gras, C., Gardier, A.M., Gallego, J.*, et al.* (2010). VGLUT3 (vesicular glutamate transporter type 3) contribution to the regulation of serotonergic transmission and anxiety. J Neurosci 30, 2198-2210.

1362 Andrade, R., and Haj-Dahmane, S. (2013). Serotonin neuron diversity in the
1363 dorsal raphe. ACS Chem Neurosci 4, 22-25.

1364 Asano, M., and Gruss, P. (1992). Pax-5 is expressed at the midbrain-hindbrain
1365 boundary during mouse development. Mech Dev 39, 29-39.

1366 Azmitia, E.C., and Segal, M. (1978). An autoradiographic analysis of the
1367 differential ascending projections of the dorsal and median raphe nuclei in the
1368 rat. J Comp Neurol 179, 641-667.

1369 Baker, K.G., Halliday, G.M., Halasz, P., Hornung, J.P., Geffen, L.B., Cotton,
1370 R.G., and Tork, I. (1991a). Cytoarchitecture of serotonin-synthesizing neurons in
1371 the pontine tegmentum of the human brain. Synapse 7, 301-320.

1372 Baker, K.G., Halliday, G.M., Hornung, J.P., Geffen, L.B., Cotton, R.G., and Tork,
1373 I. (1991b). Distribution, morphology and number of monoamine-synthesizing and
1374 substance P-containing neurons in the human dorsal raphe nucleus.
1375 Neuroscience 42, 757-775.

1376 Baker, K.G., Halliday, G.M., and Tork, I. (1990). Cytoarchitecture of the human
1377 dorsal raphe nucleus. J Comp Neurol 301, 147-161.

1378 Bakken, T.E., Hodge, R.D., Miller, J.A., Yao, Z., Nguyen, T.N., Aevermann, B.,
1379 Barkan, E., Bertagnolli, D., Casper, T., Dee, N.*, et al.* (2018). Single-nucleus and
1380 single-cell transcriptomes compared in matched cortical cell types. PLoS One 13,
1381 e0209648.

1382 Banasr, M., Hery, M., Printemps, R., and Daszuta, A. (2004). Serotonin-induced
1383 increases in adult cell proliferation and neurogenesis are mediated through
1384 different and common 5-HT receptor subtypes in the dentate gyrus and the
1385 subventricular zone. Neuropsychopharmacology 29, 450-460.

1386 Bang, S.J., and Commons, K.G. (2012). Forebrain GABAergic projections from
1387 the dorsal raphe nucleus identified by using GAD67-GFP knock-in mice. J Comp
1388 Neurol 520, 4157-4167.

1389 Bang, S.J., Jensen, P., Dymecki, S.M., and Commons, K.G. (2012). Projections
1390 and interconnections of genetically defined serotonin neurons in mice. Eur J
1391 Neurosci 35, 85-96.

1392 Barrett, K.T., Dosumu-Johnson, R.T., Daubenspeck, J.A., Brust, R.D., Kreouzis,
1393 V., Kim, J.C., Li, A., Dymecki, S.M., and Nattie, E.E. (2016). Partial Raphe
1394 Dysfunction in Neurotransmission Is Sufficient to Increase Mortality after Anoxic
1395 Exposures in Mice at a Critical Period in Postnatal Development. J Neurosci 36,
1396 3943-3953.

1397 Beaudet, A., and Descarries, L. (1976). Quantitative data on serotonin nerve
1398 terminals in adult rat neocortex. Brain Res 111, 301-309.

1399 Bellido, I., Hansson, A.C., Gomez-Luque, A.J., Andbjer, B., Agnati, L.F., and
1400 Fuxe, K. (2004). Corticosterone strongly increases the affinity of dorsal raphe 5-
1401 HT1A receptors. Neuroreport 15, 1457-1459.

1402 Brezun, J.M., and Daszuta, A. (1999). Depletion in serotonin decreases
1403 neurogenesis in the dentate gyrus and the subventricular zone of adult rats.
1404 Neuroscience 89, 999-1002.

1405 Bruchas, M.R., Land, B.B., and Chavkin, C. (2010). The dynorphin/kappa opioid
1406 system as a modulator of stress-induced and pro-addictive behaviors. Brain Res
1407 1314, 44-55.

1408 Brust, R.D., Corcoran, A.E., Richerson, G.B., Nattie, E., and Dymecki, S.M.
1409 (2014). Functional and developmental identification of a molecular subtype of
1410 brain serotonergic neuron specialized to regulate breathing dynamics. Cell Rep
1411 9, 2152-2165.

1412 Butler, A., Hoffman, P., Smibert, P., Papalexi, E., and Satija, R. (2018).
1413 Integrating single-cell transcriptomic data across different conditions,
1414 technologies, and species. Nat Biotechnol 36, 411-420.

1415 Calizo, L.H., Akanwa, A., Ma, X., Pan, Y.Z., Lemos, J.C., Craige, C., Heemstra,
1416 L.A., and Beck, S.G. (2011). Raphe serotonin neurons are not homogenous:
1417 electrophysiological, morphological and neurochemical evidence.
1418 Neuropharmacology 61, 524-543.

1419 Campbell, J.N., Macosko, E.Z., Fenselau, H., Pers, T.H., Lyubetskaya, A.,
1420 Tenen, D., Goldman, M., Verstegen, A.M., Resch, J.M., McCarroll, S.A.*, et al.*
1421 (2017). A molecular census of arcuate hypothalamus and median eminence cell
1422 types. Nat Neurosci 20, 484-496.

1423 Celada, P., Puig, M.V., Casanovas, J.M., Guillazo, G., and Artigas, F. (2001).
1424 Control of dorsal raphe serotonergic neurons by the medial prefrontal cortex:
1425 Involvement of serotonin-1A, GABA(A), and glutamate receptors. J Neurosci 21,
1426 9917-9929.

1427 Challis, C., Boulden, J., Veerakumar, A., Espallergues, J., Vassoler, F.M., Pierce,
1428 R.C., Beck, S.G., and Berton, O. (2013). Raphe GABAergic neurons mediate the
1429 acquisition of avoidance after social defeat. J Neurosci 33, 13978-13988,
1430 13988a.

1431 Chang, R.B., Strochlic, D.E., Williams, E.K., Umans, B.D., and Liberles, S.D.
1432 (2015). Vagal Sensory Neuron Subtypes that Differentially Control Breathing.
1433 Cell 161, 622-633.

1434 Chavkin, C., James, I.F., and Goldstein, A. (1982). Dynorphin is a specific
1435 endogenous ligand of the kappa opioid receptor. Science 215, 413-415.

1436 Chen, C.H., Battaglioli, G., Martin, D.L., Hobart, S.A., and Colon, W. (2003).
1437 Distinctive interactions in the holoenzyme formation for two isoforms of glutamate
1438 decarboxylase. Biochim Biophys Acta 1645, 63-71.

1439 Chen, C.P., Eastwood, S.L., Hope, T., McDonald, B., Francis, P.T., and Esiri,
1440 M.M. (2000). Immunocytochemical study of the dorsal and median raphe nuclei
1441 in patients with Alzheimer's disease prospectively assessed for behavioural
1442 changes. Neuropathol Appl Neurobiol 26, 347-355.

1443 Commons, K.G. (2009). Locally collateralizing glutamate neurons in the dorsal
1444 raphe nucleus responsive to substance P contain vesicular glutamate transporter
1445 3 (VGLUT3). J Chem Neuroanat 38, 273-281.

1446 Commons, K.G. (2015). Two major network domains in the dorsal raphe nucleus.
1447 J Comp Neurol 523, 1488-1504.

1448 Commons, K.G. (2016). Ascending serotonin neuron diversity under two
1449 umbrellas. Brain Struct Funct 221, 3347-3360.

1450 Condomitti, G., and de Wit, J. (2018). Heparan Sulfate Proteoglycans as
1451 Emerging Players in Synaptic Specificity. Front Mol Neurosci 11, 14.

1452 Crawford, L.K., Craige, C.P., and Beck, S.G. (2010). Increased intrinsic
1453 excitability of lateral wing serotonin neurons of the dorsal raphe: a mechanism for
1454 selective activation in stress circuits. J Neurophysiol 103, 2652-2663.

1455 Dahlstroem, A., and Fuxe, K. (1964). Evidence for the Existence of Monoamine-
1456 Containing Neurons in the Central Nervous System. I. Demonstration of
1457 Monoamines in the Cell Bodies of Brain Stem Neurons. Acta Physiol Scand
1458 Suppl, SUPPL 232:231-255.

1459 Dengler-Crish, C.M., Smith, M.A., and Wilson, G.N. (2017). Early Evidence of
1460 Low Bone Density and Decreased Serotonergic Synthesis in the Dorsal Raphe of
1461 a Tauopathy Model of Alzheimer's Disease. J Alzheimers Dis 55, 1605-1619.

1462 Di Donato, V., De Santis, F., Albadri, S., Auer, T.O., Duroure, K., Charpentier,
1463 M., Concordet, J.P., Gebhardt, C., and Del Bene, F. (2018). An Attractive Reelin
1464 Gradient Establishes Synaptic Lamination in the Vertebrate Visual System.
1465 Neuron 97, 1049-1062 e1046.

1466 Dobin, A., and Gingeras, T.R. (2016). Optimizing RNA-Seq Mapping with STAR.
1467 Methods Mol Biol 1415, 245-262.

1468 Dymecki, S.M., Ray, R.S., and Kim, J.C. (2010). Mapping cell fate and function
1469 using recombinase-based intersectional strategies. Methods Enzymol 477, 183-
1470 213.

1471 El Mestikawy, S., Wallen-Mackenzie, A., Fortin, G.M., Descarries, L., and
1472 Trudeau, L.E. (2011). From glutamate co-release to vesicular synergy: vesicular
1473 glutamate transporters. Nat Rev Neurosci 12, 204-216.

1474 Ellegood, J., Nakai, N., Nakatani, J., Henkelman, M., Takumi, T., and Lerch, J.
1475 (2015). Neuroanatomical Phenotypes Are Consistent With Autism-Like
1476 Behavioral Phenotypes in the 15q11-13 Duplication Mouse Model. Autism Res 8,
1477 545-555.

1478 Erbel-Sieler, C., Dudley, C., Zhou, Y., Wu, X., Estill, S.J., Han, T., Diaz-Arrastia,
1479 R., Brunskill, E.W., Potter, S.S., and McKnight, S.L. (2004). Behavioral and
1480 regulatory abnormalities in mice deficient in the NPAS1 and NPAS3 transcription
1481 factors. Proc Natl Acad Sci U S A 101, 13648-13653.

1482 Erickson, J.D., Eiden, L.E., and Hoffman, B.J. (1992). Expression cloning of a
1483 reserpine-sensitive vesicular monoamine transporter. Proc Natl Acad Sci U S A
1484 89, 10993-10997.

1485 Erlander, M.G., Tillakaratne, N.J., Feldblum, S., Patel, N., and Tobin, A.J. (1991).
1486 Two genes encode distinct glutamate decarboxylases. Neuron 7, 91-100.

1487 Evrard, A., Barden, N., Hamon, M., and Adrien, J. (2006). Glucocorticoid
1488 receptor-dependent desensitization of 5-HT1A autoreceptors by sleep
1489 deprivation: studies in GR-i transgenic mice. Sleep 29, 31-36.

1490 Fernandez, S.P., Cauli, B., Cabezas, C., Muzerelle, A., Poncer, J.C., and
1491 Gaspar, P. (2016). Multiscale single-cell analysis reveals unique phenotypes of
1492 raphe 5-HT neurons projecting to the forebrain. Brain Struct Funct 221, 4007-
1493 4025.

1494 Fox, S.R., and Deneris, E.S. (2012). Engrailed is required in maturing serotonin
1495 neurons to regulate the cytoarchitecture and survival of the dorsal raphe nucleus.
1496 J Neurosci 32, 7832-7842.

1497 Fremeau, R.T., Jr., Burman, J., Qureshi, T., Tran, C.H., Proctor, J., Johnson, J.,
1498 Zhang, H., Sulzer, D., Copenhagen, D.R., Storm-Mathisen, J.*, et al.* (2002). The
1499 identification of vesicular glutamate transporter 3 suggests novel modes of
1500 signaling by glutamate. Proc Natl Acad Sci U S A 99, 14488-14493.

1501 Fu, W., Le Maitre, E., Fabre, V., Bernard, J.F., David Xu, Z.Q., and Hokfelt, T.
1502 (2010). Chemical neuroanatomy of the dorsal raphe nucleus and adjacent
1503 structures of the mouse brain. J Comp Neurol 518, 3464-3494.

1504 Funahashi, J., Okafuji, T., Ohuchi, H., Noji, S., Tanaka, H., and Nakamura, H.
1505 (1999). Role of Pax-5 in the regulation of a mid-hindbrain organizer's activity. Dev
1506 Growth Differ 41, 59-72.

1507 Fyodorov, D., Nelson, T., and Deneris, E. (1998). Pet-1, a novel ETS domain
1508 factor that can activate neuronal nAchR gene transcription. J Neurobiol 34, 151-
1509 163.

1510 Gagnon, D., and Parent, M. (2014). Distribution of VGLUT3 in highly
1511 collateralized axons from the rat dorsal raphe nucleus as revealed by single-
1512 neuron reconstructions. PLoS One 9, e87709.

1513 Gaspar, P., and Lillesaar, C. (2012). Probing the diversity of serotonin neurons.
1514 Philos Trans R Soc Lond B Biol Sci 367, 2382-2394.

1515 Goncalves, L., Nogueira, M.I., Shammah-Lagnado, S.J., and Metzger, M. (2009).
1516 Prefrontal afferents to the dorsal raphe nucleus in the rat. Brain Res Bull 78, 240-
1517 247.

1518 Gong, S., Doughty, M., Harbaugh, C.R., Cummins, A., Hatten, M.E., Heintz, N.,
1519 and Gerfen, C.R. (2007). Targeting Cre recombinase to specific neuron
1520 populations with bacterial artificial chromosome constructs. J Neurosci 27, 9817-
1521 9823.

1522 Gras, C., Herzog, E., Bellenchi, G.C., Bernard, V., Ravassard, P., Pohl, M.,
1523 Gasnier, B., Giros, B., and El Mestikawy, S. (2002). A third vesicular glutamate
1524 transporter expressed by cholinergic and serotoninergic neurons. J Neurosci 22,
1525 5442-5451.

1526 Guo, Y.P., and Commons, K.G. (2017). Serotonin neuron abnormalities in the
1527 BTBR mouse model of autism. Autism Res 10, 66-77.

1528 Hale, M.W., and Lowry, C.A. (2011). Functional topography of midbrain and
1529 pontine serotonergic systems: implications for synaptic regulation of serotonergic
1530 circuits. Psychopharmacology (Berl) 213, 243-264.

1531 Harburg, G.C., Hall, F.S., Harrist, A.V., Sora, I., Uhl, G.R., and Eisch, A.J. (2007).
1532 Knockout of the mu opioid receptor enhances the survival of adult-generated
1533 hippocampal granule cell neurons. Neuroscience 144, 77-87.

1534 Hempel, C.M., Sugino, K., and Nelson, S.B. (2007). A manual method for the
1535 purification of fluorescently labeled neurons from the mammalian brain. Nat
1536 Protoc 2, 2924-2929.

1537 Hendricks, T., Francis, N., Fyodorov, D., and Deneris, E.S. (1999). The ETS
1538 domain factor Pet-1 is an early and precise marker of central serotonin neurons
1539 and interacts with a conserved element in serotonergic genes. J Neurosci 19,
1540 10348-10356.

1541 Hendricks, T.J., Fyodorov, D.V., Wegman, L.J., Lelutiu, N.B., Pehek, E.A.,
1542 Yamamoto, B., Silver, J., Weeber, E.J., Sweatt, J.D., and Deneris, E.S. (2003).
1543 Pet-1 ETS gene plays a critical role in 5-HT neuron development and is required
1544 for normal anxiety-like and aggressive behavior. Neuron 37, 233-247.

1545 Hennessy, M.L., Corcoran, A.E., Brust, R.D., Chang, Y., Nattie, E.E., and
1546 Dymecki, S.M. (2017). Activity of Tachykinin1-Expressing Pet1 Raphe Neurons
1547 Modulates the Respiratory Chemoreflex. J Neurosci 37, 1807-1819.

1548 Herzog, E., Gilchrist, J., Gras, C., Muzerelle, A., Ravassard, P., Giros, B.,
1549 Gaspar, P., and El Mestikawy, S. (2004). Localization of VGLUT3, the vesicular
1550 glutamate transporter type 3, in the rat brain. Neuroscience 123, 983-1002.

1551 Hioki, H., Fujiyama, F., Nakamura, K., Wu, S.X., Matsuda, W., and Kaneko, T.
1552 (2004). Chemically specific circuit composed of vesicular glutamate transporter
1553 3- and preprotachykinin B-producing interneurons in the rat neocortex. Cereb
1554 Cortex 14, 1266-1275.

1555 Hioki, H., Nakamura, H., Ma, Y.F., Konno, M., Hayakawa, T., Nakamura, K.C.,
1556 Fujiyama, F., and Kaneko, T. (2010). Vesicular glutamate transporter 3-
1557 expressing nonserotonergic projection neurons constitute a subregion in the rat
1558 midbrain raphe nuclei. J Comp Neurol 518, 668-686.

1559 Hitoshi, S., Maruta, N., Higashi, M., Kumar, A., Kato, N., and Ikenaka, K. (2007).
1560 Antidepressant drugs reverse the loss of adult neural stem cells following chronic
1561 stress. J Neurosci Res 85, 3574-3585.

1562 Hodge, R.D., Bakken, T.E., Miller, J.A., Smith, K.A., Barkan, E.R., Graybuck,
1563 L.T., Close, J.L., Long, B., Johansen, N., Penn, O.*, et al.* (2019). Conserved cell
1564 types with divergent features in human versus mouse cortex. Nature 573, 61-68.

1565 Hoffman, B.J., Mezey, E., and Brownstein, M.J. (1991). Cloning of a serotonin
1566 transporter affected by antidepressants. Science 254, 579-580.

1567 Huang, K.W., Ochandarena, N.E., Philson, A.C., Hyun, M., Birnbaum, J.E.,
1568 Cicconet, M., and Sabatini, B.L. (2019). Molecular and anatomical organization of
1569 the dorsal raphe nucleus. Elife 8.

1570 Ishimura, K., Takeuchi, Y., Fujiwara, K., Tominaga, M., Yoshioka, H., and
1571 Sawada, T. (1988). Quantitative analysis of the distribution of serotonin-
1572 immunoreactive cell bodies in the mouse brain. Neurosci Lett 91, 265-270.

1573 Iyer, A., Kmiecik, T.E., Park, M., Daar, I., Blair, D., Dunn, K.J., Sutrave, P., Ihle,
1574 J.N., Bodescot, M., and Vande Woude, G.F. (1990). Structure, tissue-specific
1575 expression, and transforming activity of the mouse met protooncogene. Cell
1576 Growth Differ 1, 87-95.

1577 Jacobs, B.L., and Azmitia, E.C. (1992). Structure and function of the brain
1578 serotonin system. Physiol Rev 72, 165-229.

1579 Jensen, P., Farago, A.F., Awatramani, R.B., Scott, M.M., Deneris, E.S., and
1580 Dymecki, S.M. (2008). Redefining the serotonergic system by genetic lineage.
1581 Nat Neurosci 11, 417-419.

1582 Ji, X., Wang, H., Zhu, M., He, Y., Zhang, H., Chen, X., Gao, W., Fu, Y., and
1583 Alzheimer's Disease Neuroimaging, I. (2020). Brainstem atrophy in the early
1584 stage of Alzheimer's disease: a voxel-based morphometry study. Brain Imaging
1585 Behav.

1586 Johnson, M.D. (1994). Synaptic glutamate release by postnatal rat serotonergic
1587 neurons in microculture. Neuron 12, 433-442.

1588 Joyner, A.L., Kornberg, T., Coleman, K.G., Cox, D.R., and Martin, G.R. (1985).
1589 Expression during embryogenesis of a mouse gene with sequence homology to
1590 the Drosophila engrailed gene. Cell 43, 29-37.

1591 Joyner, A.L., and Martin, G.R. (1987). En-1 and En-2, two mouse genes with
1592 sequence homology to the Drosophila engrailed gene: expression during
1593 embryogenesis. Genes Dev 1, 29-38.

1594 Judge, S.J., Ingram, C.D., and Gartside, S.E. (2004). Moderate differences in
1595 circulating corticosterone alter receptor-mediated regulation of 5-
1596 hydroxytryptamine neuronal activity. J Psychopharmacol 18, 475-483.

1597 Kapoor, V., Provost, A.C., Agarwal, P., and Murthy, V.N. (2016). Activation of
1598 raphe nuclei triggers rapid and distinct effects on parallel olfactory bulb output
1599 channels. Nat Neurosci 19, 271-282.

1600 Kast, R.J., Wu, H.H., Williams, P., Gaspar, P., and Levitt, P. (2017). Specific
1601 Connectivity and Unique Molecular Identity of MET Receptor Tyrosine Kinase
1602 Expressing Serotonergic Neurons in the Caudal Dorsal Raphe Nuclei. ACS
1603 Chem Neurosci 8, 1053-1064.

1604 Kim, J.C., Cook, M.N., Carey, M.R., Shen, C., Regehr, W.G., and Dymecki, S.M.
1605 (2009). Linking genetically defined neurons to behavior through a broadly
1606 applicable silencing allele. Neuron 63, 305-315.

1607 Kimmel, R.A., Turnbull, D.H., Blanquet, V., Wurst, W., Loomis, C.A., and Joyner,
1608 A.L. (2000). Two lineage boundaries coordinate vertebrate apical ectodermal
1609 ridge formation. Genes Dev 14, 1377-1389.

1610 Kirby, L.G., Pernar, L., Valentino, R.J., and Beck, S.G. (2003). Distinguishing
1611 characteristics of serotonin and non-serotonin-containing cells in the dorsal raphe
1612 nucleus: electrophysiological and immunohistochemical studies. Neuroscience
1613 116, 669-683.

1614 Kosofsky, B.E., and Molliver, M.E. (1987). The serotoninergic innervation of
1615 cerebral cortex: different classes of axon terminals arise from dorsal and median
1616 raphe nuclei. Synapse 1, 153-168.

1617 Krueger, K.C., and Deneris, E.S. (2008). Serotonergic transcription of human
1618 FEV reveals direct GATA factor interactions and fate of Pet-1-deficient serotonin
1619 neuron precursors. J Neurosci 28, 12748-12758.

1620 Laaris, N., Haj-Dahmane, S., Hamon, M., and Lanfumey, L. (1995).
1621 Glucocorticoid receptor-mediated inhibition by corticosterone of 5-HT1A
1622 autoreceptor functioning in the rat dorsal raphe nucleus. Neuropharmacology 34,
1623 1201-1210.

1624 Land, B.B., Bruchas, M.R., Lemos, J.C., Xu, M., Melief, E.J., and Chavkin, C.
1625 (2008). The dysphoric component of stress is encoded by activation of the
1626 dynorphin kappa-opioid system. J Neurosci 28, 407-414.

1627 Land, B.B., Bruchas, M.R., Schattauer, S., Giardino, W.J., Aita, M., Messinger,
1628 D., Hnasko, T.S., Palmiter, R.D., and Chavkin, C. (2009). Activation of the kappa
1629 opioid receptor in the dorsal raphe nucleus mediates the aversive effects of
1630 stress and reinstates drug seeking. Proc Natl Acad Sci U S A 106, 19168-19173.

1631 Lazaro-Pena, M.I., Diaz-Balzac, C.A., Bulow, H.E., and Emmons, S.W. (2018).
1632 Synaptogenesis Is Modulated by Heparan Sulfate in Caenorhabditis elegans.
1633 Genetics 209, 195-208.

1634 Lesch, K.P., Wolozin, B.L., Estler, H.C., Murphy, D.L., and Riederer, P. (1993).
1635 Isolation of a cDNA encoding the human brain serotonin transporter. J Neural
1636 Transm Gen Sect 91, 67-72.

1637 Levine, E.S., and Jacobs, B.L. (1992). Neurochemical afferents controlling the
1638 activity of serotonergic neurons in the dorsal raphe nucleus: microiontophoretic
1639 studies in the awake cat. J Neurosci 12, 4037-4044.

1640 Lidov, H.G., Grzanna, R., and Molliver, M.E. (1980). The serotonin innervation of
1641 the cerebral cortex in the rat--an immunohistochemical analysis. Neuroscience 5,
1642 207-227.

1643 Lidov, H.G., and Molliver, M.E. (1982). Immunohistochemical study of the
1644 development of serotonergic neurons in the rat CNS. Brain Res Bull 9, 559-604.

1645 Lin, J.H., Takano, T., Arcuino, G., Wang, X., Hu, F., Darzynkiewicz, Z., Nunes,
1646 M., Goldman, S.A., and Nedergaard, M. (2007). Purinergic signaling regulates
1647 neural progenitor cell expansion and neurogenesis. Dev Biol 302, 356-366.

1648 Liu, C., Maejima, T., Wyler, S.C., Casadesus, G., Herlitze, S., and Deneris, E.S.
1649 (2010). Pet-1 is required across different stages of life to regulate serotonergic
1650 function. Nat Neurosci 13, 1190-1198.

1651 Liu, Z., Zhou, J., Li, Y., Hu, F., Lu, Y., Ma, M., Feng, Q., Zhang, J.E., Wang, D.,
1652 Zeng, J.*, et al.* (2014). Dorsal raphe neurons signal reward through 5-HT and
1653 glutamate. Neuron 81, 1360-1374.

1654 Lorez, H.P., and Richards, J.G. (1982). Supra-ependymal serotoninergic nerves
1655 in mammalian brain: morphological, pharmacological and functional studies.
1656 Brain Res Bull 9, 727-741.

1657 Lovatt, D., Ruble, B.K., Lee, J., Dueck, H., Kim, T.K., Fisher, S., Francis, C.,
1658 Spaethling, J.M., Wolf, J.A., Grady, M.S.*, et al.* (2014). Transcriptome in vivo
1659 analysis (TIVA) of spatially defined single cells in live tissue. Nat Methods 11,
1660 190-196.

1661 Love, C.E., and Prince, V.E. (2012). Expression and retinoic acid regulation of
1662 the zebrafish nr2f orphan nuclear receptor genes. Dev Dyn 241, 1603-1615.

1663 Luo, J., Feng, Q., Wei, L., and Luo, M. (2017). Optogenetic activation of dorsal
1664 raphe neurons rescues the autistic-like social deficits in Shank3 knockout mice.
1665 Cell Res 27, 950-953.

1666 Macosko, E.Z., Basu, A., Satija, R., Nemesh, J., Shekhar, K., Goldman, M.,
1667 Tirosh, I., Bialas, A.R., Kamitaki, N., Martersteck, E.M.*, et al.* (2015). Highly
1668 Parallel Genome-wide Expression Profiling of Individual Cells Using Nanoliter
1669 Droplets. Cell 161, 1202-1214.

1670 Maddaloni, G., Bertero, A., Pratelli, M., Barsotti, N., Boonstra, A., Giorgi, A.,
1671 Migliarini, S., and Pasqualetti, M. (2017). Development of Serotonergic Fibers in
1672 the Post-Natal Mouse Brain. Front Cell Neurosci 11, 202.

1673 Madisen, L., Garner, A.R., Shimaoka, D., Chuong, A.S., Klapoetke, N.C., Li, L.,
1674 van der Bourg, A., Niino, Y., Egolf, L., Monetti, C.*, et al.* (2015). Transgenic mice

1675 for intersectional targeting of neural sensors and effectors with high specificity
1676 and performance. Neuron 85, 942-958.

1677 Makrides, N., Panayiotou, E., Fanis, P., Karaiskos, C., Lapathitis, G., and Malas,
1678 S. (2018). Sequential Role of SOXB2 Factors in GABAergic Neuron Specification
1679 of the Dorsal Midbrain. Front Mol Neurosci 11, 152.

1680 McDevitt, R.A., Tiran-Cappello, A., Shen, H., Balderas, I., Britt, J.P., Marino,
1681 R.A., Chung, S.L., Richie, C.T., Harvey, B.K., and Bonci, A. (2014). Serotonergic
1682 versus nonserotonergic dorsal raphe projection neurons: differential participation
1683 in reward circuitry. Cell Rep 8, 1857-1869.

1684 Michaelson, J.J., Shin, M.K., Koh, J.Y., Brueggeman, L., Zhang, A., Katzman, A.,
1685 McDaniel, L., Fang, M., Pufall, M., and Pieper, A.A. (2017). Neuronal PAS
1686 Domain Proteins 1 and 3 Are Master Regulators of Neuropsychiatric Risk Genes.
1687 Biol Psychiatry 82, 213-223.

1688 Michelsen, K.A., Prickaerts, J., and Steinbusch, H.W. (2008). The dorsal raphe
1689 nucleus and serotonin: implications for neuroplasticity linked to major depression
1690 and Alzheimer's disease. Prog Brain Res 172, 233-264.

1691 Michelsen, K.A., Schmitz, C., and Steinbusch, H.W. (2007). The dorsal raphe
1692 nucleus--from silver stainings to a role in depression. Brain Res Rev 55, 329-342.

1693 Minge, D., Senkov, O., Kaushik, R., Herde, M.K., Tikhobrazova, O., Wulff, A.B.,
1694 Mironov, A., van Kuppevelt, T.H., Oosterhof, A., Kochlamazashvili, G.*, et al.*
1695 (2017). Heparan Sulfates Support Pyramidal Cell Excitability, Synaptic Plasticity,
1696 and Context Discrimination. Cereb Cortex 27, 903-918.

1697 Mirzadeh, Z., Doetsch, F., Sawamoto, K., Wichterle, H., and Alvarez-Buylla, A.
1698 (2010). The subventricular zone en-face: wholemount staining and ependymal
1699 flow. J Vis Exp.

1700 Miyazaki, K., Narita, N., and Narita, M. (2005). Maternal administration of
1701 thalidomide or valproic acid causes abnormal serotonergic neurons in the
1702 offspring: implication for pathogenesis of autism. Int J Dev Neurosci 23, 287-297.

1703 Molliver, M.E. (1987). Serotonergic neuronal systems: what their anatomic
1704 organization tells us about function. J Clin Psychopharmacol 7, 3S-23S.

1705 Mosko, S.S., Haubrich, D., and Jacobs, B.L. (1977). Serotonergic afferents to the
1706 dorsal raphe nucleus: evdience from HRP and synaptosomal uptake studies.
1707 Brain Res 119, 269-290.

1708 Munster-Wandowski, A., Zander, J.F., Richter, K., and Ahnert-Hilger, G. (2016).
1709 Co-existence of Functionally Different Vesicular Neurotransmitter Transporters.
1710 Front Synaptic Neurosci 8, 4.

1711 Muzerelle, A., Scotto-Lomassese, S., Bernard, J.F., Soiza-Reilly, M., and
1712 Gaspar, P. (2016). Conditional anterograde tracing reveals distinct targeting of
1713 individual serotonin cell groups (B5-B9) to the forebrain and brainstem. Brain
1714 Struct Funct 221, 535-561.

1715 Negoias, S., Croy, I., Gerber, J., Puschmann, S., Petrowski, K., Joraschky, P.,
1716 and Hummel, T. (2010). Reduced olfactory bulb volume and olfactory sensitivity
1717 in patients with acute major depression. Neuroscience 169, 415-421.

1718 Niederkofler, V., Asher, T.E., Okaty, B.W., Rood, B.D., Narayan, A., Hwa, L.S.,
1719 Beck, S.G., Miczek, K.A., and Dymecki, S.M. (2016). Identification of
1720 Serotonergic Neuronal Modules that Affect Aggressive Behavior. Cell Rep 17,
1721 1934-1949.

1722 Nyberg, J., Anderson, M.F., Meister, B., Alborn, A.M., Strom, A.K., Brederlau, A.,
1723 Illerskog, A.C., Nilsson, O., Kieffer, T.J., Hietala, M.A.*, et al.* (2005). Glucose-
1724 dependent insulinotropic polypeptide is expressed in adult hippocampus and
1725 induces progenitor cell proliferation. J Neurosci 25, 1816-1825.

1726 O'Hearn, E., and Molliver, M.E. (1984). Organization of raphe-cortical projections
1727 in rat: a quantitative retrograde study. Brain Res Bull 13, 709-726.

1728 Ogawa, S.K., Cohen, J.Y., Hwang, D., Uchida, N., and Watabe-Uchida, M.
1729 (2014). Organization of monosynaptic inputs to the serotonin and dopamine
1730 neuromodulatory systems. Cell Rep 8, 1105-1118.

1731 Okaty, B.W., Commons, K.G., and Dymecki, S.M. (2019). Embracing diversity in
1732 the 5-HT neuronal system. Nat Rev Neurosci.

1733 Okaty, B.W., Freret, M.E., Rood, B.D., Brust, R.D., Hennessy, M.L., deBairos, D.,
1734 Kim, J.C., Cook, M.N., and Dymecki, S.M. (2015). Multi-Scale Molecular
1735 Deconstruction of the Serotonin Neuron System. Neuron 88, 774-791.

1736 Pelosi, B., Migliarini, S., Pacini, G., Pratelli, M., and Pasqualetti, M. (2014).
1737 Generation of Pet1210-Cre transgenic mouse line reveals non-serotonergic
1738 expression domains of Pet1 both in CNS and periphery. PLoS One 9, e104318.

1739 Peyron, C., Petit, J.M., Rampon, C., Jouvet, M., and Luppi, P.H. (1998).
1740 Forebrain afferents to the rat dorsal raphe nucleus demonstrated by retrograde
1741 and anterograde tracing methods. Neuroscience 82, 443-468.

1742 Peyron, C., Rampon, C., Petit, J.M., and Luppi, P.H. (2018). Sub-regions of the
1743 dorsal raphe nucleus receive different inputs from the brainstem. Sleep Med 49,
1744 53-63.

1745 Pillai, A., Mansouri, A., Behringer, R., Westphal, H., and Goulding, M. (2007).
1746 Lhx1 and Lhx5 maintain the inhibitory-neurotransmitter status of interneurons in
1747 the dorsal spinal cord. Development 134, 357-366.

1748 Pollak Dorocic, I., Furth, D., Xuan, Y., Johansson, Y., Pozzi, L., Silberberg, G.,
1749 Carlen, M., and Meletis, K. (2014). A whole-brain atlas of inputs to serotonergic
1750 neurons of the dorsal and median raphe nuclei. Neuron 83, 663-678.

1751 Poulin, J.F., Tasic, B., Hjerling-Leffler, J., Trimarchi, J.M., and Awatramani, R.
1752 (2016). Disentangling neural cell diversity using single-cell transcriptomics. Nat
1753 Neurosci 19, 1131-1141.

1754 Prakash, N., Stark, C.J., Keisler, M.N., Luo, L., Der-Avakian, A., and Dulcis, D.
1755 (2019). Serotonergic plasticity in the dorsal raphe nucleus characterizes
1756 susceptibility and resilience to anhedonia. J Neurosci.

1757 Prouty, E.W., Chandler, D.J., and Waterhouse, B.D. (2017). Neurochemical
1758 differences betweentarget-specific populations of rat dorsal raphe projection
1759 neurons. Brain Res.

1760 Ray, R.S., Corcoran, A.E., Brust, R.D., Kim, J.C., Richerson, G.B., Nattie, E., and
1761 Dymecki, S.M. (2011). Impaired respiratory and body temperature control upon
1762 acute serotonergic neuron inhibition. Science 333, 637-642.

1763 Ren, J., Friedmann, D., Xiong, J., Liu, C.D., Ferguson, B.R., Weerakkody, T.,
1764 DeLoach, K.E., Ran, C., Pun, A., Sun, Y.*, et al.* (2018). Anatomically Defined and
1765 Functionally Distinct Dorsal Raphe Serotonin Sub-systems. Cell 175, 472-487
1766 e420.

1767 Ren, J., Isakova, A., Friedmann, D., Zeng, J., Grutzner, S.M., Pun, A., Zhao,
1768 G.Q., Kolluru, S.S., Wang, R., Lin, R.*, et al.* (2019). Single-cell transcriptomes
1769 and whole-brain projections of serotonin neurons in the mouse dorsal and
1770 median raphe nuclei. Elife 8.

1771 Rood, B.D., Calizo, L.H., Piel, D., Spangler, Z.P., Campbell, K., and Beck, S.G.
1772 (2014). Dorsal raphe serotonin neurons in mice: immature hyperexcitability
1773 transitions to adult state during first three postnatal weeks suggesting sensitive
1774 period for environmental perturbation. J Neurosci 34, 4809-4821.

1775 Rosenberg, A.B., Roco, C.M., Muscat, R.A., Kuchina, A., Sample, P., Yao, Z.,
1776 Graybuck, L.T., Peeler, D.J., Mukherjee, S., Chen, W.*, et al.* (2018). Single-cell

profiling of the developing mouse brain and spinal cord with split-pool barcoding. Science 360, 176-182.

Saunders, A., Macosko, E.Z., Wysoker, A., Goldman, M., Krienen, F.M., de Rivera, H., Bien, E., Baum, M., Bortolin, L., Wang, S., *et al.* (2018). Molecular Diversity and Specializations among the Cells of the Adult Mouse Brain. Cell 174, 1015-1030 e1016.

Sciolino, N.R., Plummer, N.W., Chen, Y.W., Alexander, G.M., Robertson, S.D., Dudek, S.M., McElligott, Z.A., and Jensen, P. (2016). Recombinase-Dependent Mouse Lines for Chemogenetic Activation of Genetically Defined Cell Types. Cell Rep 15, 2563-2573.

Sengupta, A., Bocchio, M., Bannerman, D.M., Sharp, T., and Capogna, M. (2017). Control of Amygdala Circuits by 5-HT Neurons via 5-HT and Glutamate Cotransmission. J Neurosci 37, 1785-1796.

Shikanai, H., Yoshida, T., Konno, K., Yamasaki, M., Izumi, T., Ohmura, Y., Watanabe, M., and Yoshioka, M. (2012). Distinct neurochemical and functional properties of GAD67-containing 5-HT neurons in the rat dorsal raphe nucleus. J Neurosci 32, 14415-14426.

Simic, G., Babic Leko, M., Wray, S., Harrington, C.R., Delalle, I., Jovanov-Milosevic, N., Bazadona, D., Buee, L., de Silva, R., Di Giovanni, G., *et al.* (2017). Monoaminergic neuropathology in Alzheimer's disease. Prog Neurobiol 151, 101-138.

Siopi, E., Denizet, M., Gabellec, M.M., de Chaumont, F., Olivo-Marin, J.C., Guilloux, J.P., Lledo, P.M., and Lazarini, F. (2016). Anxiety- and Depression-Like States Lead to Pronounced Olfactory Deficits and Impaired Adult Neurogenesis in Mice. J Neurosci 36, 518-531.

Soghomonian, J.J., and Martin, D.L. (1998). Two isoforms of glutamate decarboxylase: why? Trends Pharmacol Sci 19, 500-505.

Sos, K.E., Mayer, M.I., Cserep, C., Takacs, F.S., Szonyi, A., Freund, T.F., and Nyiri, G. (2017). Cellular architecture and transmitter phenotypes of neurons of the mouse median raphe region. Brain Struct Funct 222, 287-299.

Soumier, A., Banasr, M., Kerkerian-Le Goff, L., and Daszuta, A. (2010). Region- and phase-dependent effects of 5-HT(1A) and 5-HT(2C) receptor activation on adult neurogenesis. Eur Neuropsychopharmacol 20, 336-345.

Spaethling, J.M., Piel, D., Dueck, H., Buckley, P.T., Morris, J.F., Fisher, S.A., Lee, J., Sul, J.Y., Kim, J., Bartfai, T., *et al.* (2014). Serotonergic neuron regulation informed by in vivo single-cell transcriptomics. FASEB J 28, 771-780.

1813 Stanco, A., Pla, R., Vogt, D., Chen, Y., Mandal, S., Walker, J., Hunt, R.F.,
1814 Lindtner, S., Erdman, C.A., Pieper, A.A.*, et al.* (2014). NPAS1 represses the
1815 generation of specific subtypes of cortical interneurons. Neuron 84, 940-953.

1816 Steinbusch, H.W. (1981). Distribution of serotonin-immunoreactivity in the central
1817 nervous system of the rat-cell bodies and terminals. Neuroscience 6, 557-618.

1818 Steinbusch, H.W., van der Kooy, D., Verhofstad, A.A., and Pellegrino, A. (1980).
1819 Serotonergic and non-serotonergic projections from the nucleus raphe dorsalis to
1820 the caudate-putamen complex in the rat, studied by a combined
1821 immunofluorescence and fluorescent retrograde axonal labeling technique.
1822 Neurosci Lett 19, 137-142.

1823 Steinbusch, H.W., Verhofstad, A.A., and Joosten, H.W. (1978). Localization of
1824 serotonin in the central nervous system by immunohistochemistry: description of
1825 a specific and sensitive technique and some applications. Neuroscience 3, 811-
1826 819.

1827 Stuart, T., Butler, A., Hoffman, P., Hafemeister, C., Papalexi, E., Mauck, W.M.,
1828 3rd, Hao, Y., Stoeckius, M., Smibert, P., and Satija, R. (2019). Comprehensive
1829 Integration of Single-Cell Data. Cell 177, 1888-1902 e1821.

1830 Tasic, B. (2018). Single cell transcriptomics in neuroscience: cell classification
1831 and beyond. Curr Opin Neurobiol 50, 242-249.

1832 Tasic, B., Menon, V., Nguyen, T.N., Kim, T.K., Jarsky, T., Yao, Z., Levi, B., Gray,
1833 L.T., Sorensen, S.A., Dolbeare, T.*, et al.* (2016). Adult mouse cortical cell
1834 taxonomy revealed by single cell transcriptomics. Nat Neurosci 19, 335-346.

1835 Tasic, B., Yao, Z., Graybuck, L.T., Smith, K.A., Nguyen, T.N., Bertagnolli, D.,
1836 Goldy, J., Garren, E., Economo, M.N., Viswanathan, S.*, et al.* (2018). Shared and
1837 distinct transcriptomic cell types across neocortical areas. Nature 563, 72-78.

1838 Teissier, A., Chemiakine, A., Inbar, B., Bagchi, S., Ray, R.S., Palmiter, R.D.,
1839 Dymecki, S.M., Moore, H., and Ansorge, M.S. (2015). Activity of Raphe
1840 Serotonergic Neurons Controls Emotional Behaviors. Cell Rep 13, 1965-1976.

1841 Teng, T., Gaillard, A., Muzerelle, A., and Gaspar, P. (2017). EphrinA5 Signaling
1842 Is Required for the Distinctive Targeting of Raphe Serotonin Neurons in the
1843 Forebrain. eNeuro 4.

1844 Tong, C.K., Chen, J., Cebrian-Silla, A., Mirzadeh, Z., Obernier, K., Guinto, C.D.,
1845 Tecott, L.H., Garcia-Verdugo, J.M., Kriegstein, A., and Alvarez-Buylla, A. (2014).
1846 Axonal control of the adult neural stem cell niche. Cell Stem Cell 14, 500-511.

1847 Tritsch, N.X., Ding, J.B., and Sabatini, B.L. (2012). Dopaminergic neurons inhibit
1848 striatal output through non-canonical release of GABA. Nature 490, 262-266.

1849 Trivellin, G., Bjelobaba, I., Daly, A.F., Larco, D.O., Palmeira, L., Faucz, F.R.,
1850 Thiry, A., Leal, L.F., Rostomyan, L., Quezado, M.*, et al.* (2016). Characterization
1851 of GPR101 transcript structure and expression patterns. J Mol Endocrinol 57, 97-
1852 111.

1853 Trivellin, G., Hernandez-Ramirez, L.C., Swan, J., and Stratakis, C.A. (2018). An
1854 orphan G-protein-coupled receptor causes human gigantism and/or acromegaly:
1855 Molecular biology and clinical correlations. Best Pract Res Clin Endocrinol Metab
1856 32, 125-140.

1857 Usoskin, D., Furlan, A., Islam, S., Abdo, H., Lonnerberg, P., Lou, D., Hjerling-
1858 Leffler, J., Haeggstrom, J., Kharchenko, O., Kharchenko, P.V.*, et al.* (2015).
1859 Unbiased classification of sensory neuron types by large-scale single-cell RNA
1860 sequencing. Nat Neurosci 18, 145-153.

1861 Vakalopoulos, C. (2017). Alzheimer's Disease: The Alternative Serotonergic
1862 Hypothesis of Cognitive Decline. J Alzheimers Dis 60, 859-866.

1863 Vasudeva, R.K., Lin, R.C., Simpson, K.L., and Waterhouse, B.D. (2011).
1864 Functional organization of the dorsal raphe efferent system with special
1865 consideration of nitrergic cell groups. J Chem Neuroanat 41, 281-293.

1866 Vasudeva, R.K., and Waterhouse, B.D. (2014). Cellular profile of the dorsal
1867 raphe lateral wing sub-region: relationship to the lateral dorsal tegmental
1868 nucleus. J Chem Neuroanat 57-58, 15-23.

1869 Vertes, R.P. (1991). A PHA-L analysis of ascending projections of the dorsal
1870 raphe nucleus in the rat. J Comp Neurol 313, 643-668.

1871 Vertes, R.P., and Kocsis, B. (1994). Projections of the dorsal raphe nucleus to
1872 the brainstem: PHA-L analysis in the rat. J Comp Neurol 340, 11-26.

1873 Vincent, M.Y., Donner, N.C., Smith, D.G., Lowry, C.A., and Jacobson, L. (2018).
1874 Dorsal raphe nucleus glucocorticoid receptors inhibit tph2 gene expression in
1875 male C57BL/6J mice. Neurosci Lett 665, 48-53.

1876 Vincent, M.Y., and Jacobson, L. (2014). Glucocorticoid receptor deletion from the
1877 dorsal raphe nucleus of mice reduces dysphoria-like behavior and impairs
1878 hypothalamic-pituitary-adrenocortical axis feedback inhibition. Eur J Neurosci 39,
1879 1671-1681.

1880 Voisin, A.N., Mnie-Filali, O., Giguere, N., Fortin, G.M., Vigneault, E., El
1881 Mestikawy, S., Descarries, L., and Trudeau, L.E. (2016). Axonal Segregation and

1882 Role of the Vesicular Glutamate Transporter VGLUT3 in Serotonin Neurons.
1883 Front Neuroanat 10, 39.

1884 Walther, D.J., and Bader, M. (2003). A unique central tryptophan hydroxylase
1885 isoform. Biochem Pharmacol 66, 1673-1680.

1886 Walther, D.J., Peter, J.U., Bashammakh, S., Hortnagl, H., Voits, M., Fink, H., and
1887 Bader, M. (2003). Synthesis of serotonin by a second tryptophan hydroxylase
1888 isoform. Science 299, 76.

1889 Wang, H.L., Zhang, S., Qi, J., Wang, H., Cachope, R., Mejias-Aponte, C.A.,
1890 Gomez, J.A., Mateo-Semidey, G.E., Beaudoin, G.M.J., Paladini, C.A.*, et al.*
1891 (2019). Dorsal Raphe Dual Serotonin-Glutamate Neurons Drive Reward by
1892 Establishing Excitatory Synapses on VTA Mesoaccumbens Dopamine Neurons.
1893 Cell Rep 26, 1128-1142 e1127.

1894 Wang, R., Hausknecht, K., Shen, R.Y., and Haj-Dahmane, S. (2018).
1895 Potentiation of Glutamatergic Synaptic Transmission Onto Dorsal Raphe
1896 Serotonergic Neurons in the Valproic Acid Model of Autism. Front Pharmacol 9,
1897 1185.

1898 Watanabe, M., Serizawa, M., Sawada, T., Takeda, K., Takahashi, T., Yamamoto,
1899 N., Koizumi, F., and Koh, Y. (2014). A novel flow cytometry-based cell capture
1900 platform for the detection, capture and molecular characterization of rare tumor
1901 cells in blood. J Transl Med 12, 143.

1902 Weissbourd, B., Ren, J., DeLoach, K.E., Guenthner, C.J., Miyamichi, K., and
1903 Luo, L. (2014). Presynaptic partners of dorsal raphe serotonergic and GABAergic
1904 neurons. Neuron 83, 645-662.

1905 Wu, H.H., and Levitt, P. (2013). Prenatal expression of MET receptor tyrosine
1906 kinase in the fetal mouse dorsal raphe nuclei and the visceral motor/sensory
1907 brainstem. Dev Neurosci 35, 1-16.

1908 Wyler, S.C., Donovan, L.J., Yeager, M., and Deneris, E. (2015). Pet-1 Controls
1909 Tetrahydrobiopterin Pathway and Slc22a3 Transporter Genes in Serotonin
1910 Neurons. ACS Chem Neurosci 6, 1198-1205.

1911 Wyler, S.C., Spencer, W.C., Green, N.H., Rood, B.D., Crawford, L., Craige, C.,
1912 Gresch, P., McMahon, D.G., Beck, S.G., and Deneris, E. (2016). Pet-1 Switches
1913 Transcriptional Targets Postnatally to Regulate Maturation of Serotonin Neuron
1914 Excitability. J Neurosci 36, 1758-1774.

1915 Ye, W., Bouchard, M., Stone, D., Liu, X., Vella, F., Lee, J., Nakamura, H., Ang,
1916 S.L., Busslinger, M., and Rosenthal, A. (2001). Distinct regulators control the

1917 expression of the mid-hindbrain organizer signal FGF8. Nat Neurosci 4, 1175-
1918 1181.

1919 Ye, Y., Zhao, Z., Xu, H., Zhang, X., Su, X., Yang, Y., Yu, X., and He, X. (2016).
1920 Activation of Sphingosine 1-Phosphate Receptor 1 Enhances Hippocampus
1921 Neurogenesis in a Rat Model of Traumatic Brain Injury: An Involvement of
1922 MEK/Erk Signaling Pathway. Neural Plast 2016, 8072156.

1923 Zeisel, A., Hochgerner, H., Lonnerberg, P., Johnsson, A., Memic, F., van der
1924 Zwan, J., Haring, M., Braun, E., Borm, L.E., La Manno, G.*, et al.* (2018).
1925 Molecular Architecture of the Mouse Nervous System. Cell 174, 999-1014 e1022.

1926 Zeisel, A., Munoz-Manchado, A.B., Codeluppi, S., Lonnerberg, P., La Manno, G.,
1927 Jureus, A., Marques, S., Munguba, H., He, L., Betsholtz, C.*, et al.* (2015). Brain
1928 structure. Cell types in the mouse cortex and hippocampus revealed by single-
1929 cell RNA-seq. Science 347, 1138-1142.

1930 Zhang, P., Lu, H., Peixoto, R.T., Pines, M.K., Ge, Y., Oku, S., Siddiqui, T.J., Xie,
1931 Y., Wu, W., Archer-Hartmann, S.*, et al.* (2018). Heparan Sulfate Organizes
1932 Neuronal Synapses through Neurexin Partnerships. Cell 174, 1450-1464 e1423.

1933 Zweig, R.M., Ross, C.A., Hedreen, J.C., Steele, C., Cardillo, J.E., Whitehouse,
1934 P.J., Folstein, M.F., and Price, D.L. (1988). The neuropathology of aminergic
1935 nuclei in Alzheimer's disease. Ann Neurol 24, 233-242.

1936

1937 **Figure Legends**

1938 Figure 1: High throughput scRNA-seq and clustering analyses reveal as many as
1939 fourteen distinct molecularly-defined subtypes (clusters) of *Pet1* neurons in the
1940 mouse DR. (A) Schematic depicting the experimental and analytical workflow,
1941 specifically: (1) brain dissection and DR microdissection, (2) cellular dissociation
1942 and microfluidic fluorescence-based cell sorting using the On-chip
1943 Biotechnologies system, and (3) library preparation, sequencing, and analysis
1944 using 10X genomics, Illumina sequencing, and the R package Seurat,
1945 respectively. (B) Hierarchical clustering of *Pet1* neuron subtypes identified by
1946 Louvain clustering (using the top two thousand genes with the highest variance,
1947 PCs = 1:5, 8:50, and resolution=0.9), with violin plots depicting the log-
1948 normalized expression of a common set of genes (*Tph2, Gad2, Gad1, Vglut3,*

and *Met*) found useful for characterizing cluster structure across multiple resolutions (see Figure 1- figure supplement 2). (C) UMAP visualization of single-neuron transcriptome community/similarity structure, with colors and numbers indicating discrete clusters (same clustering parameters as (B)). (D) Heatmap depicting the scaled expression of the top five marker genes for each cluster (ranked by p-value, or in some cases fold enrichment).

Figure 1 - figure supplement 1: Systematic variation of key clustering parameters allows for exploration of the community structure of DR *Pet1* single neuron transcriptomes at variable resolutions. (A) Scatterplot of the variance (standard deviation, Y-axis) explained by the first 250 principal components (X-axis). (B) Level plot/heat map depicting the number of clusters (DR *Pet1* neuron subtypes) resulting from variation of the number of included principle components (Y-axis) and the resolution parameter to the Seurat function FindClusters (X-axis). (C) Line graph of the frequency (Y-axis) that a given number of clusters (X-axis) arises from the analysis performed in B. (D) Plots showing the parameters (white) that lead to cluster numbers found to have the highest frequency (5, 11, 14, and 17 clusters, top left to bottom right respectively).

Figure 1 - figure supplement 2: Analysis of clusters at successively increasing resolution values. (A, D, G) Hierarchical clustering of *Pet1* neuron subtypes identified by Louvain clustering at varying resolutions (specifically, the resolution value passed to the Seurat function FindClusters A= 0.1, D= 0.3, G= 0.7), and violin plots depicting the normalized expression of *Tph2, Gad2, Gad1, Vglut3,* and *Met.* (B, E, H) UMAP visualization of community structure at a given resolution (B= 0.1, E= 0.3, H= 0.7). (C, F, I) Heatmap depicting the scaled expression of the top five marker genes for each cluster (ranked by p-value).

Figure 1 - figure supplement 3: Expression of serotonin-related genes across DR *Pet1* neuron subtypes. Violin plots depicting the log-normalized expression of twelve serotonin neuron marker genes across the fourteen *Pet1* neuron clusters.

Figure 2: Expression patterns of a subset of highly variable genes classified by biological function. Dot plots show the expression of a gene (Y-axis) in each cluster (X-axis), separated by biological function. The size of the dot represents the percentage of cells expressing the gene and saturation of color represents average normalized expression level. For convenience, the UMAP plot from Figure 1C is re-displayed at the bottom right to help link gene expression patterns to overall cluster structure. Minimum inclusion criteria for genes was that they were among the top 2000 highest variance genes and/or they were found to be significantly enriched or “de-enriched” in at least one subtype cluster.

Figure 3: Intersectionally targeted *Pet1* neuron subtypes have different anatomical distributions in subregions of the DR. (A-E) Low magnification view of 40 µm coronal sections showing the DR from rostral to caudal (1-6) in triple transgenic animals. Cell bodies are labeled by the intersectional expression of a Cre driver of interest, *Pet1::Flpe*, and the intersectional allele *FrePe* (green eGFP marked cells expressing both Cre and Flpe and red mCherry expressing *Pet1::Flpe* subtractive population) unless otherwise noted. (A) *Sert::cre; Pet1::Flpe; FrePe*, (B) *Vglut3::cre; Pet1::Flpe; hM3Dq* (green mCherry-hM3Dq marked cells expressing Cre and Flpe and red eGFP expressing *Pet1::Flpe* subtractive population), (C) *Npy2r::IRES-cre; Pet1::Flpe; FrePe*, (D) *P2ry1::IRES-cre; Pet1::Flpe; FrePe*. Top row shows violin plots depicting transcript expression (10X scRNA-seq data) of the respective gene corresponding with each Cre driver. Scale bar (A1) equals 100 µm.

Figure 3 - figure supplement 1: TPH2 and VGLUT3 antibody staining of *Pet1* neurons is anatomically biased within different DR subdomains. (A) Bar graph showing the percentage of *Pet1* cells that are TPH2-negative in a specific anatomical subdivision of the DR in an *En1::cre; Pet1::Flpe; RC::FrePe* (Green labeled neurons with intersectional expression of *En1::cre* and *Pet1::Flpe)*. Anatomical subdivisions (Dorsomedial (dmDR), Medial (mDR), Ventromedial (vmDR)) are depicted in the coronal photomicrographs from D-I, from rostral (left) to caudal (right). n=2, bar graph depicting the mean with SEM. (B) TPH2

immunostaining in an *En1::cre; Pet1::Flpe; RC::FrePe* coronal section. Open arrow indicates an example of a TPH2+ *En1::cre; Pet1::Flpe* cell and the closed arrow indicates a TPH2- *En1::cre; Pet1::Flpe* cell. (C) VGLUT3 immunostaining in a *Vglut3::IRES-cre; Pet1::Flpe; RC::FL-hM3Dq* coronal section (green indicating neurons labeled by the intersection of *Vglut3::IRES-cre* and *Pet1::Flpe*, red indicating the subtractive *Pet1* population). Open arrow shows an example of a VGLUT3 immunopositive *Vglut3::cre; Pet1::Flpe* cell, closed arrow shows a VGLUT3 immunonegative subtractive *Pet1* cell. Scale bar in B and C equals 25 μm. (D-I) Quantification of the percentage of VGLUT3 immunoreactive *Vglut3::cre; Pet1::Flpe* lineage (dark green) and VGLUT3 immunoreactive subtractive *Pet1* lineage cells (dark red) within anatomical subdivisions of the dorsal raphe from rostral (D) to caudal (I), in comparison to VGLUT3 immunonegative *Vglut3*::cre;*Pet1::Flpe* and subtractive *Pet1* neurons (light green and light red respectively). Low magnification images indicate representative quantified images. Anatomical subdivisions (dorsomedial (dm), medial (m), ventromedial (vm) and dorsolateral (dl)) are delineated with white brackets. Scale bar in D equals 100 μm, n=2, bar graph depicts mean with SEM. (J) Summary coronal brainstem schematic showing the distribution of VGLUT3 immuno-positive and immuno-negative *Vglut3::cre; Pet1::Flpe* (dark and light green) and subtractive *Pet1* neurons (dark and light red) in the DR from rostral (left) to caudal (right).

Figure 4: scRNA-seq of *Pet1* neurons sorted from anatomical subdomains map onto specific 10x scRNA-seq clusters. (A) Schematic of the pipeline used for manual sorting and sequencing, including referenced anatomical subdomains mapped onto representative images of the DR. *Pet1* neurons are in green. (B) Dot plot mapping manually sorted cells from a given genotype and anatomical subdomain (Y-axis) to the fourteen 10x clusters (X-axis). The size of the dot indicates the percentage of single cells from a genotype/anatomical region attributed to a reference cluster. Note, the asterisks after *Drd2::cre;Pet1::Flpe* is to denote that these data come from a previously published study (Niederkofler,

et al. 2016), and these particular single-cell libraries were prepared using the Nugen Ovation RNA-seq System v2 kit, rather than SMART-Seq v4. The expression of a selection of highly variable and cluster marker genes is depicted in Figure 4- figure supplement 1.

Figure 4 – figure supplement 1: Expression patterns of a selection of highly variable and cluster marker genes that show anatomical bias. Dot plot depicting the expression of genes (Y-axis) across manually sorted cells from a specific subdomain and genotype (left) and 10x scRNA-seq clusters (right). The size of the dot represents the percentage of cells expressing the gene and saturation of color represents the average normalized expression level. As with Figure 4, the asterisks after *Drd2::cre;Pet1::Flpe* denotes that these data come from a previously published study (Niederkofler, et al. 2016), and these particular single-cell libraries were prepared using the Nugen Ovation RNA-seq System v2 kit, rather than SMART-Seq v4.

Figure 4 - figure supplement 2: PAX5 and SATB2 are expressed predominately in rostral dorsomedial and dorsolateral *Pet1* neurons while NR2F2 is expressed predominately in caudal *Pet1* neurons. (A) Representative regions of the DR used for quantification of immunostaining from rostral (left) to caudal (right). Brackets indicate anatomical subdivisions- dorsomedial (dmDR, dark blue), medial (mDR, tan), ventromedial (vmDR, gray), and dorsolateral (dlDR, light blue). (B-D) (top) Distribution of normalized transcript expression of *Pax5* (B), *Satb2* (C) or *Nr2f2* (D) within *Pet1* neuron subtypes and (bottom) the percentage of counted *Pet1* neurons immunoreactive for PAX5 (B), SATB2 (C) or NR2F2 (D) that are arising from *Vglut3::cre; Pet1::Flpe* neurons (dark grey) in comparison to the subtractive *Pet1* population (light grey). (B'-D') Bar graph depicting the percentage of *Pet1* neurons immunopositive for PAX5 (B'), SATB2 (C') or NR2F2 (D') in anatomical subdivisions of the DR from rostral to caudal. n=2- 4 depending on rostral to caudal section, bar graph depicting mean with SEM. (B''-D'') Representative coronal confocal image depicting a region of the DR with *Pet1* neurons immunopositive for PAX5 (B''), SATB2 (C'') or NR2F2 (D'').

Vglut3::cre;Pet1::Flpe cells are shown in green, subtractive *Pet1* cells in red, and antibody of interest in blue. (E) Coronal brainstem schematics depicting the anatomical distribution of *Pet1* neurons (top) expressing PAX5 and NR2F2, or (bottom) that are expressing *Gad2-Tph2, Vglut3-Tph2,* or *Vglut3* only from rostral (right) to caudal (left).

Figure 5: *P2ry1::cre; Pet1::Flpe* neurons project throughout the ventricles and are in close apposition to proliferating cells in the SVZ and RMS. (A) Flat mount of the lateral wall of the lateral ventricle of a *P2ry1::cre;Pet1::Flpe;Ai65* animal, where *P2ry1::cre;Pet1::Flpe* fibers are in grey. Scale bar = 100 μm. (B-E) High magnification confocal images from regions of the lateral wall represented in red boxes in A. Scale bar (B) = 100 μm. (F) 3D brain schematic showing the *P2ry1::cre;Pet1:Flpe* cell bodies (dark orange) in the caudal part of the DR (light orange) and fibers (dark orange) projecting through the ventricles (grey) and along the migrating neuroblasts of the rostral migratory stream (RMS, blue). (G-H) Coronal confocal images depicting *P2ry1::cre;Pet1::Flpe* fibers (orange) from *P2ry1::cre;Pet1::Flpe;Ai65* animals in the SVZ (G) and RMS (H). Proliferating cells labeled with Ki67 (grey) and migrating neuroblasts labeled with doublecortin (DCX, blue). Scale bar (G, H) = 50 μm

Figure 6: *P2ry1::cre;Pet1::Flpe* neurons have a distinct firing phenotype. (A) Example voltage traces from a neuron type that started firing action potentials with short latency (mean= 17.32 ms ± 6.61 at 200 pA), in response to 750 ms current pulses. (B) Example traces from a neuron type that started firing action potentials with medium latency (mean= 64.18 ms ± 9.8 at 200 pA). (C) Example traces from a neuron that started firing action potentials with long latency (mean= 476.55 ms ± 223.64 at 200 pA). (D) Example traces from a neuron that fired action potentials with short latency (mean= 12.6 ms ± 5.9 at 200 pA) and that displayed frequency adaptation. (E) Frequency-Current curves show *P2ry1::cre; Pet1::Flpe* neurons (tdTomato$^+$ *P2ry1::IRES-cre;Pet1::Flpe;Ai65,* n=9; 3 animals; red circles) are less excitable than nearby caudodorsal raphe non-*P2ry1::cre;Pet1::Flpe* populations (eGFP$^+$ *P2ry1::IRES-cre;Pet1::Flpe;RC::FL-*

hM3Dq, n=8; 3 animals; black squares) or neurons from the dorsomedial and dorsolateral Raphe *Gad2::cre;Pet1::Flpe* population (tdTomato$^+$ *Gad2::IRES-cre;Pet1::Flpe;Ai65*, n=12; 2 animals; blue diamonds) p<0.0001 Kruskal-Wallis test. (F) Heat map shows the distribution of firing types of recorded cells according to genotype, note that while firing type B is the most frequent overall, all recorded *P2ry1::cre; Pet1::Flpe* neurons belong to type D.

Figure 6- figure supplement 1: Key membrane properties distinguish serotonergic neuron firing types. Groups are same as in Figure 6; all *P2ry1::IRES-cre; Pet1::Flpe;RC::Ai65* neurons belong to group D. (A) Scatterplot of rheobase (in pA) exhibited by each cell of the corresponding firing type. (B) Scatterplot of the latency of each cell to fire the first action potential after the onset of the depolarizing current pulse by the corresponding firing type. (C) Same as B except firing type D was split into subgroups Da and Db, based on bi-modality visible in B. (D) Scatterplot of the maximum firing frequency (in Hz) exhibited by each cell of the corresponding firing type. (E) Scatterplot of the membrane resistance (in MΩ), exhibited by each cell of the corresponding firing type. (F) Scatterplot of the average half-width of the action potential of each firing type at maximum firing rate (in ms). Dashed lines indicate the median. Asterisks indicate statistical significance, Kruskal-Wallis test *p < 0.05, **p < 0.01, ***p < 0.001, ****p < 0.0001.

Figure 7: Correspondence of serotonin subtypes identified in previous studies (Y-axis) to the fourteen 10x clusters identified in this study (X-axis). The size of the dot indicates the percentage of single cells from the original cluster that are attributed to a given reference cluster.

Figure 8: Fourteen *Pet1* subtypes in the DR can be defined by the combinatorial expression of transcription factors and other markers and have distinct anatomical organization. (A) Molecular markers (neurotransmitters (NTs), transcription factors (TFs), and other markers) on the left half of the table, with increasing specificity from left to right, that combinatorically define each identified

2126 *Pet1* subtype (colored column). Anatomical biases of each cluster are described
2127 on the right, with increasing specificity from right to left. Note, cluster numbers
2128 have been re-ordered to highlight anatomical groupings.

Figure 1

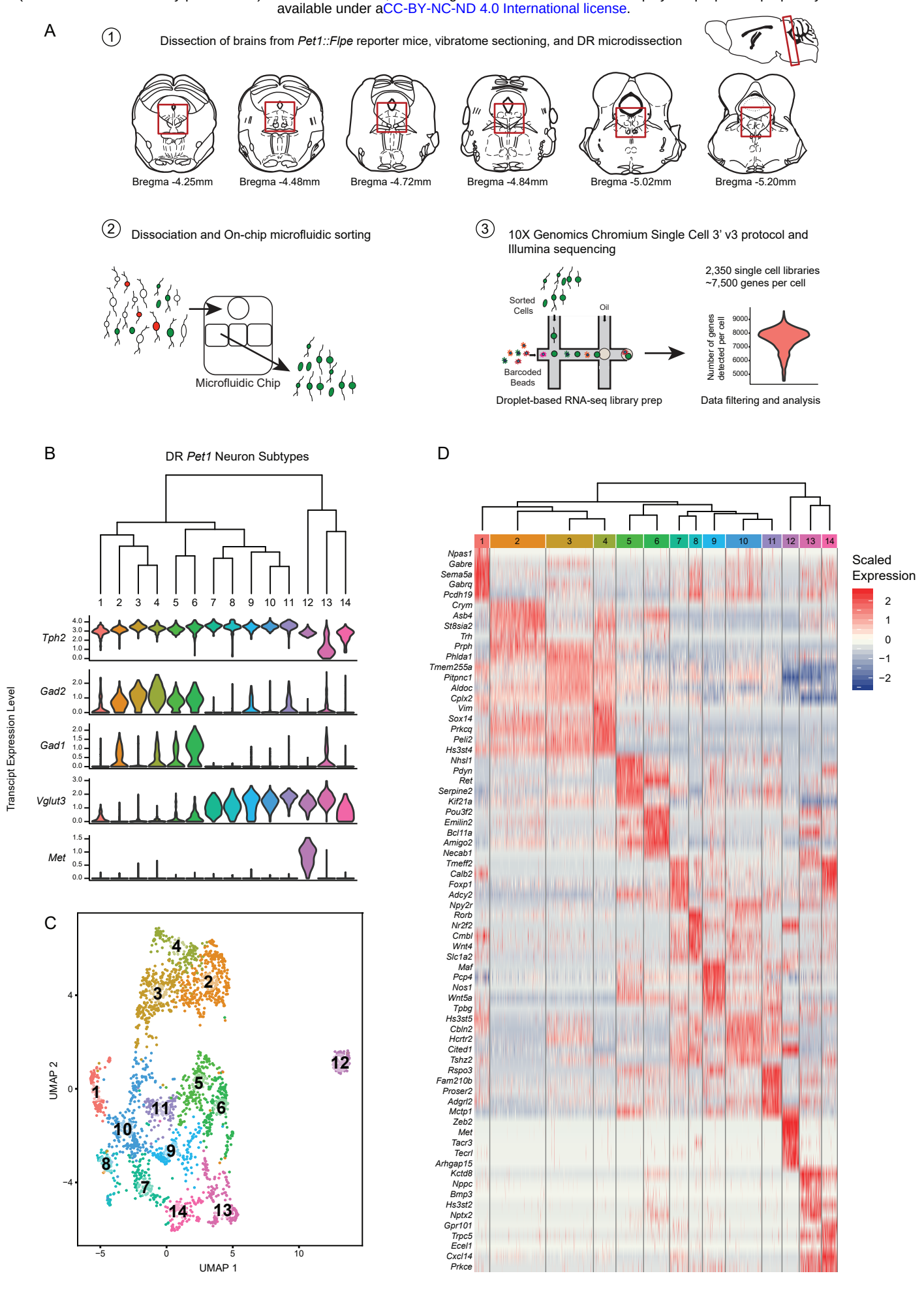

Figure 1—figure supplement 1

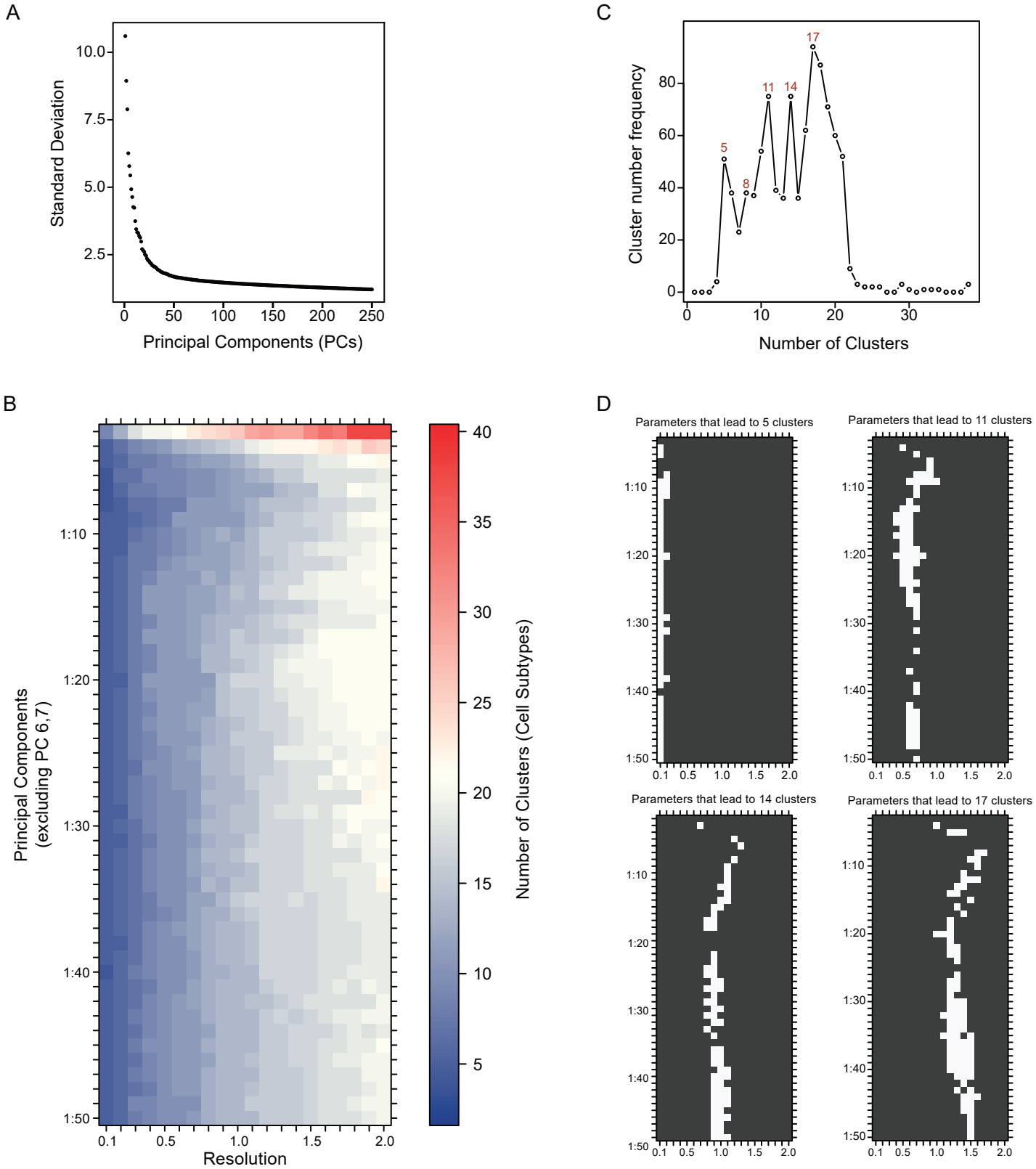

Figure 1- figure supplement 2

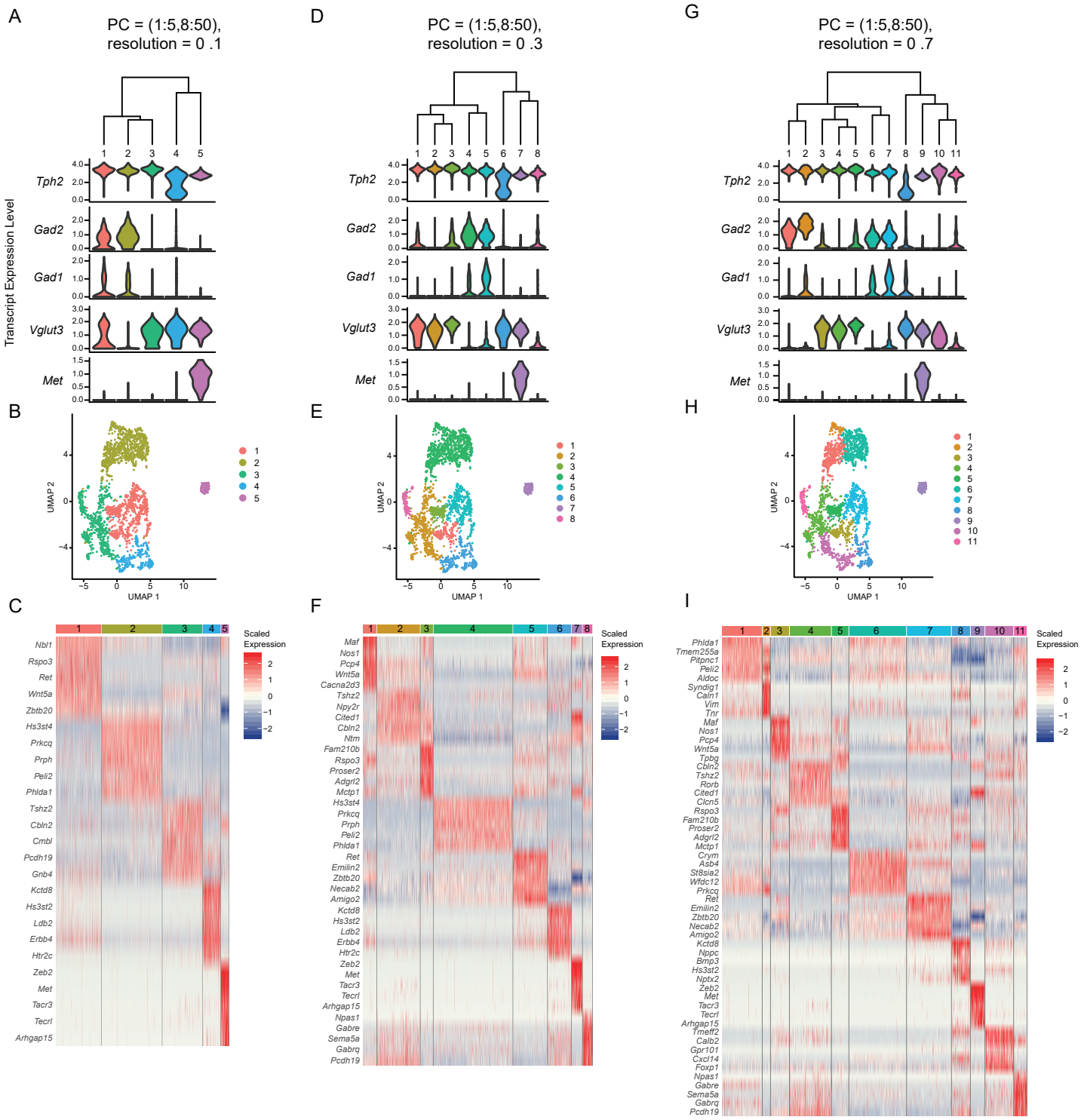

Figure 1- figure supplement 3

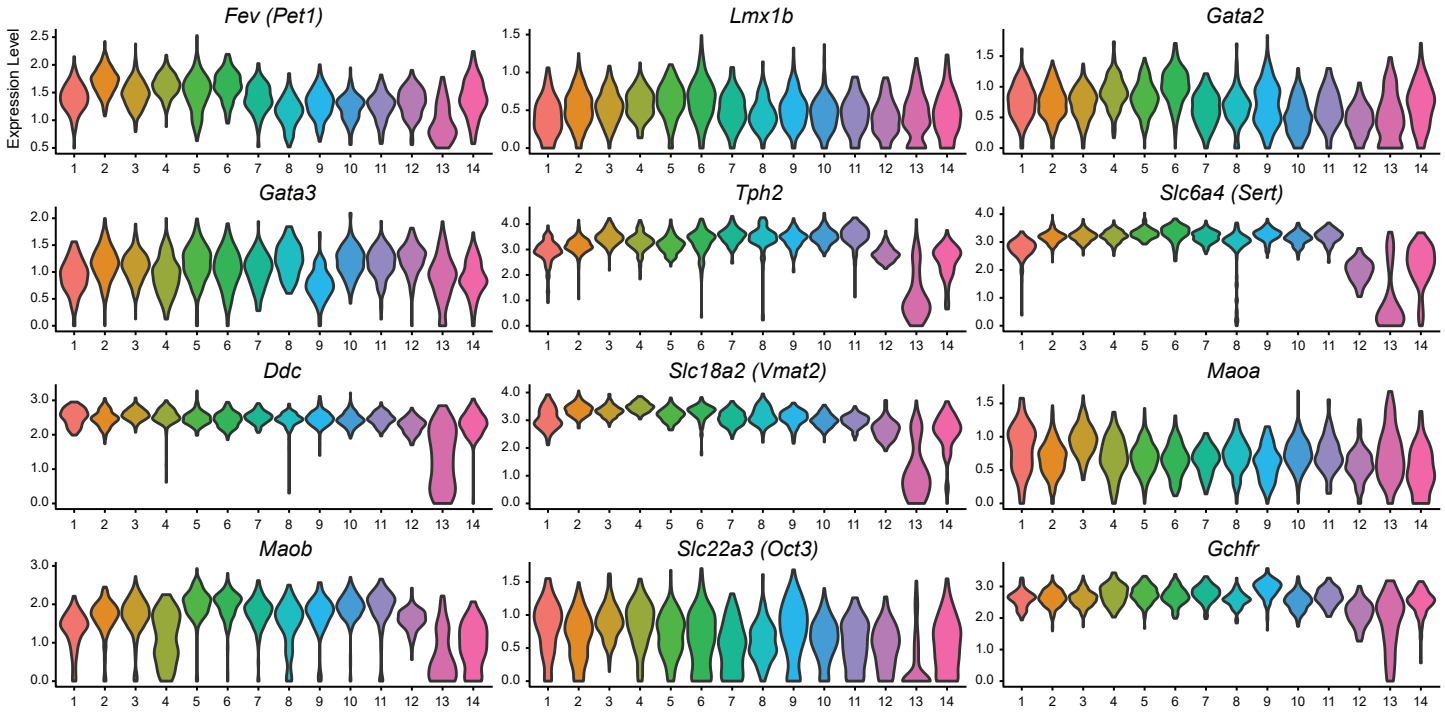

Figure 2

Figure 3

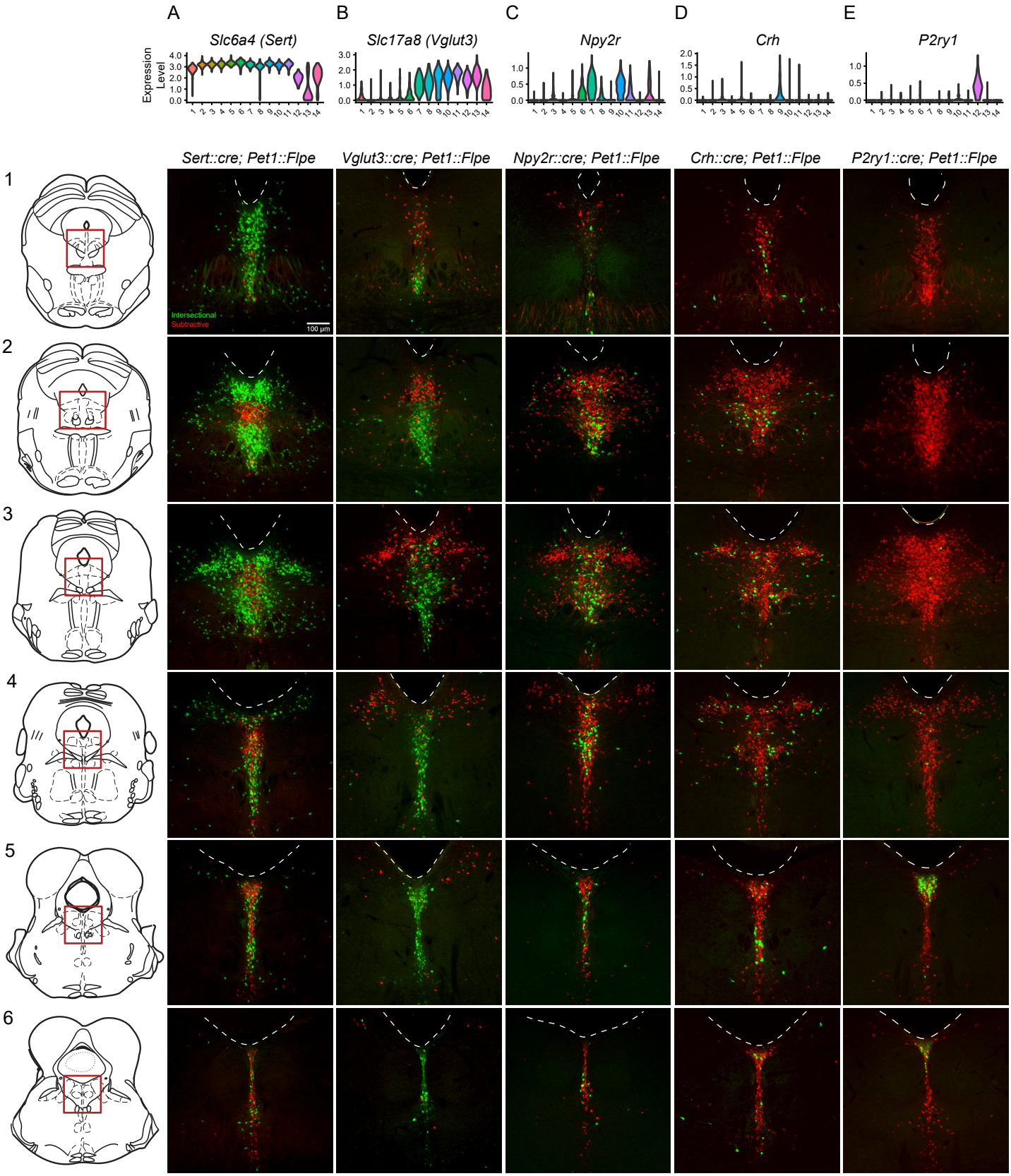

Figure 3 –figure supplement 1

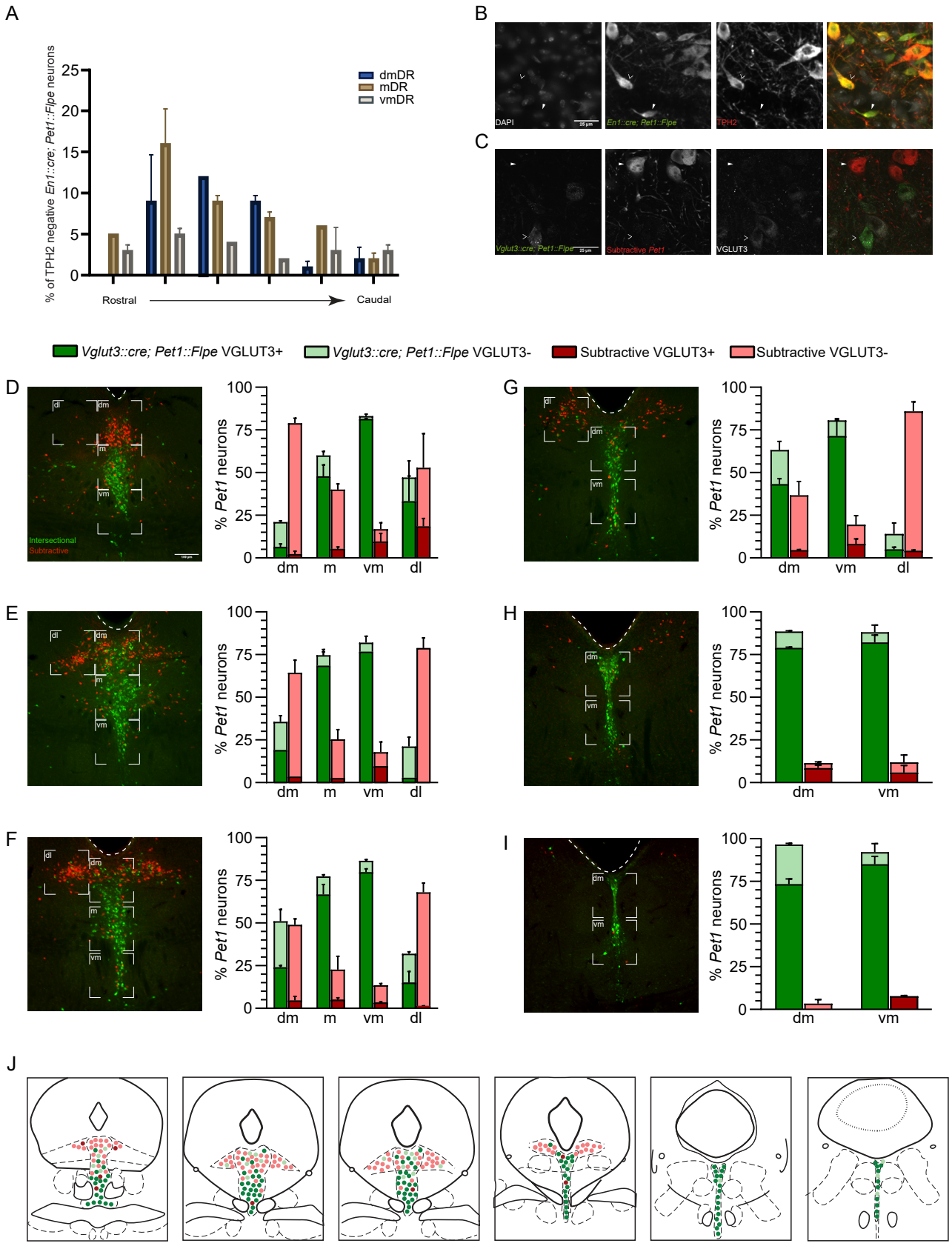

Figure 4

A

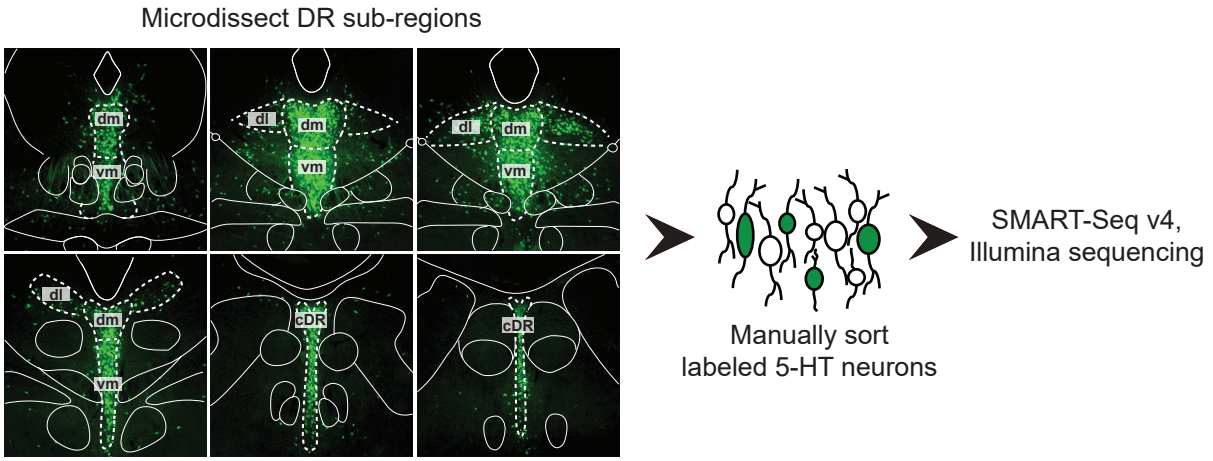

B

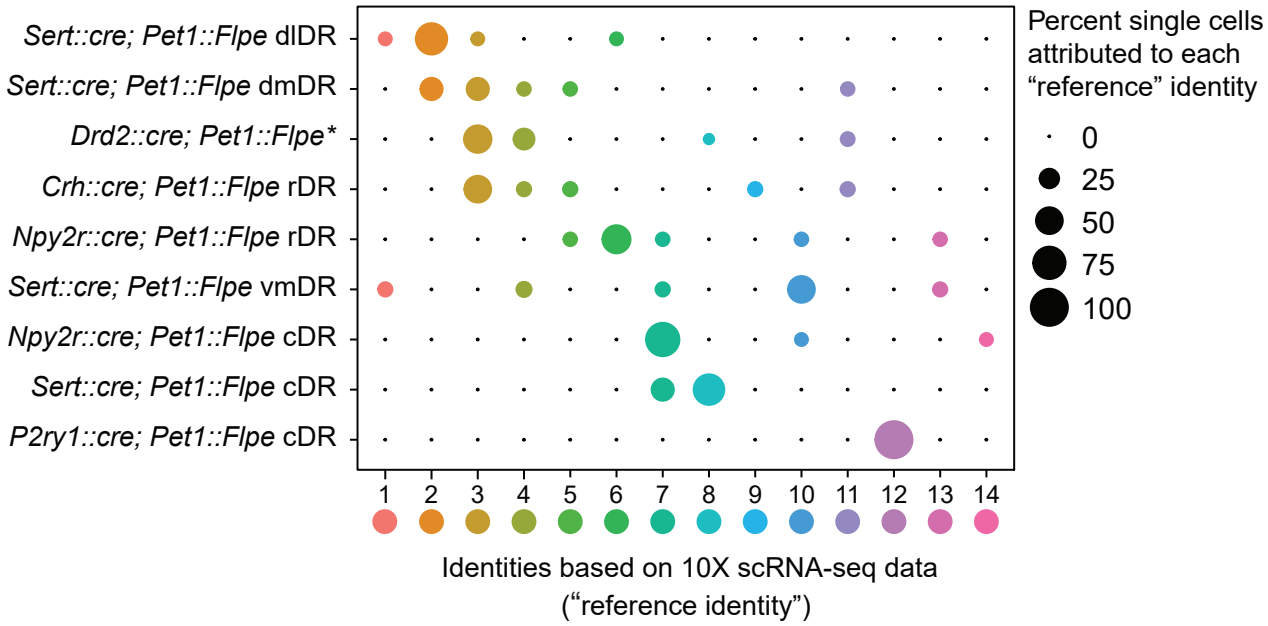

Figure 4 - figure supplement 1

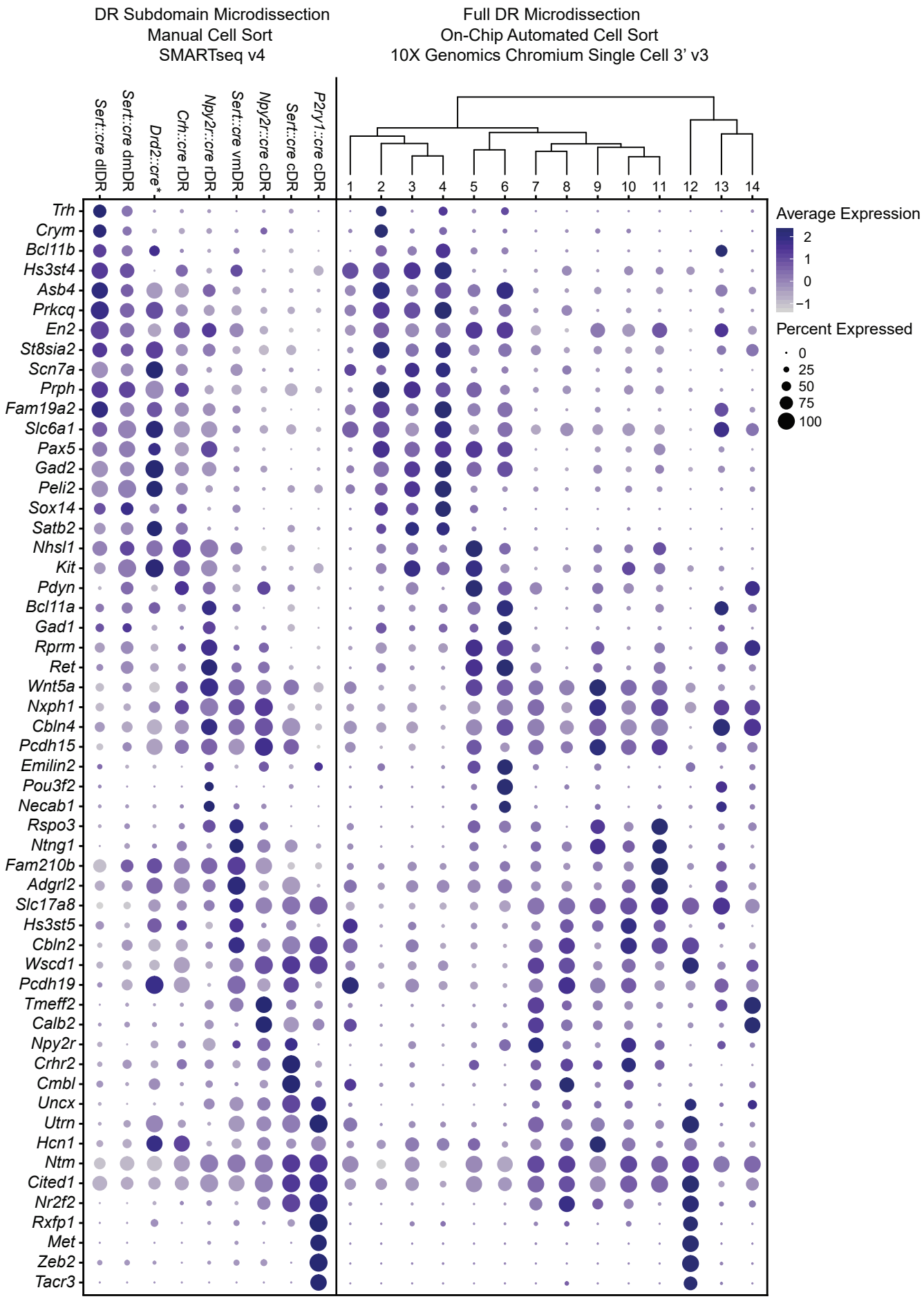

Figure 4 – figure supplement 2

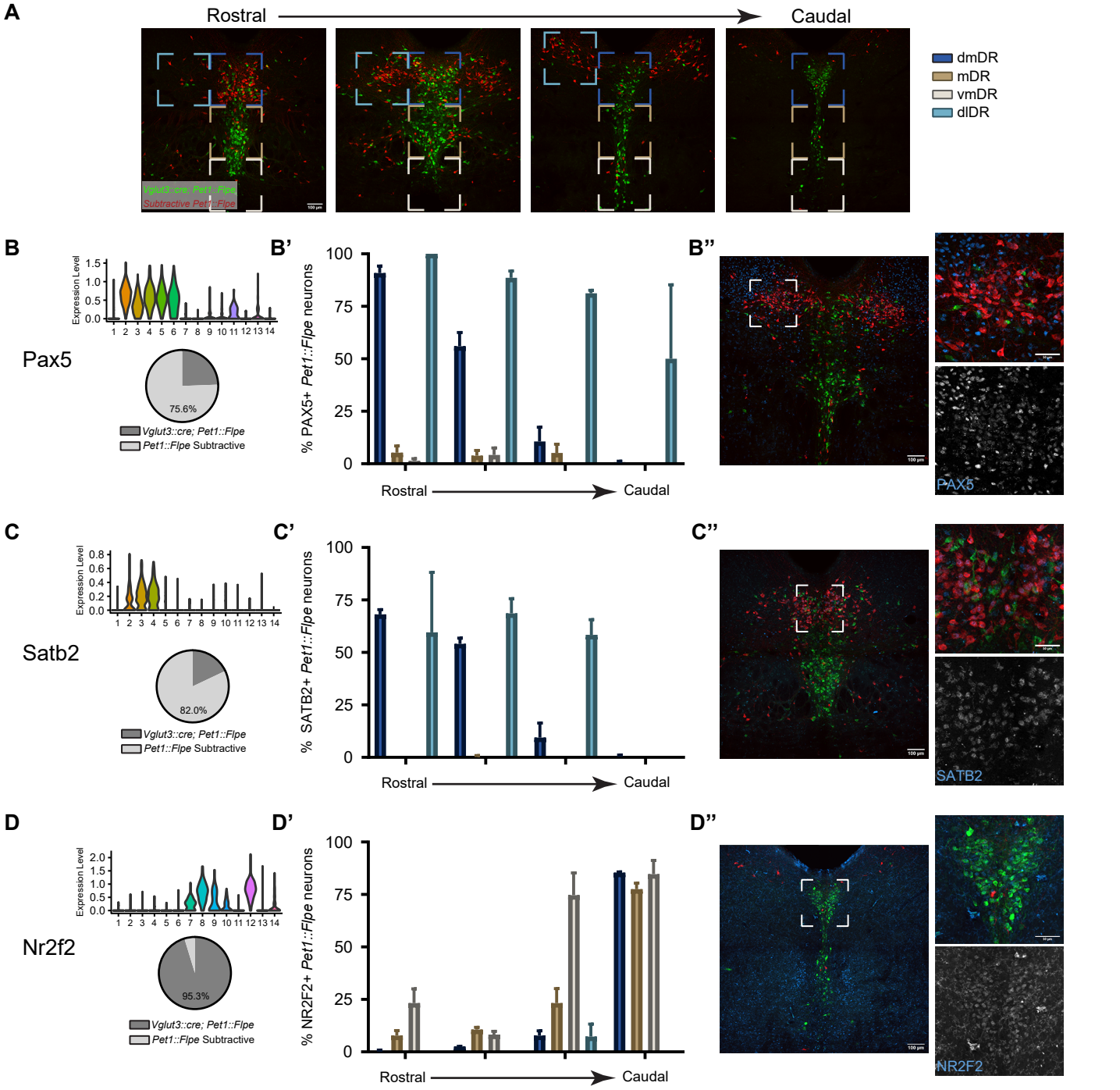

Figure 5

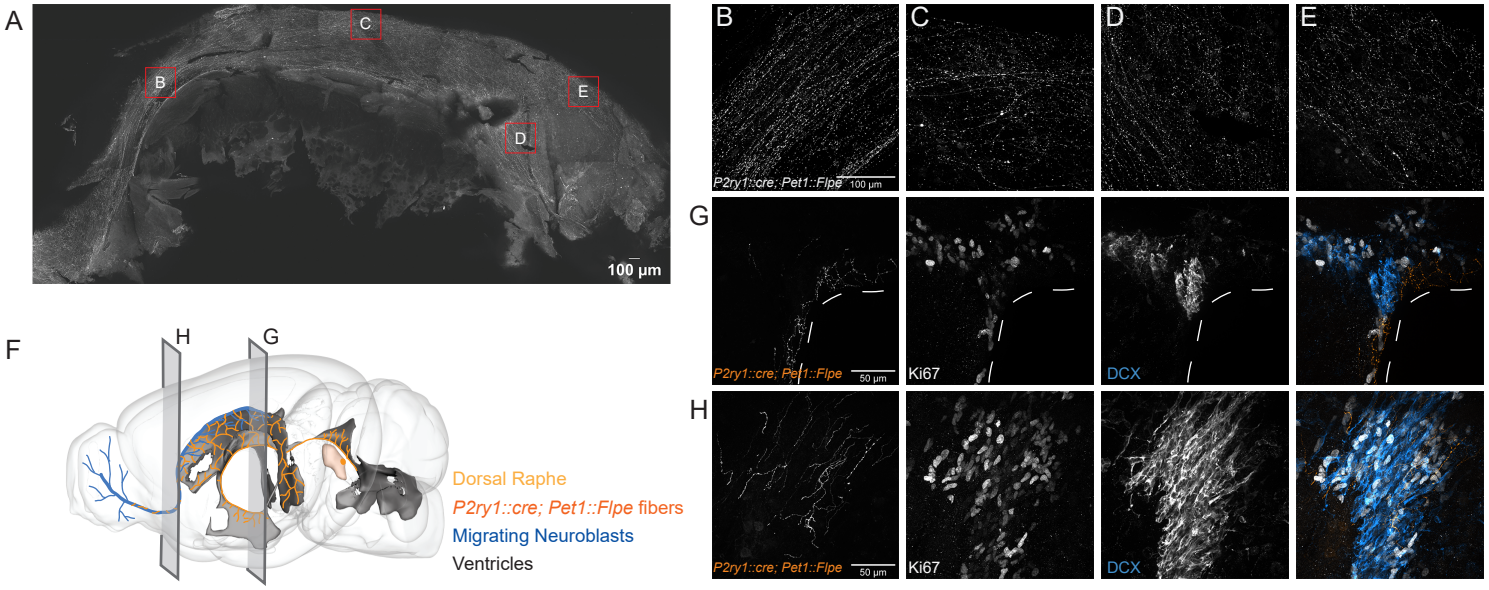

Figure 6

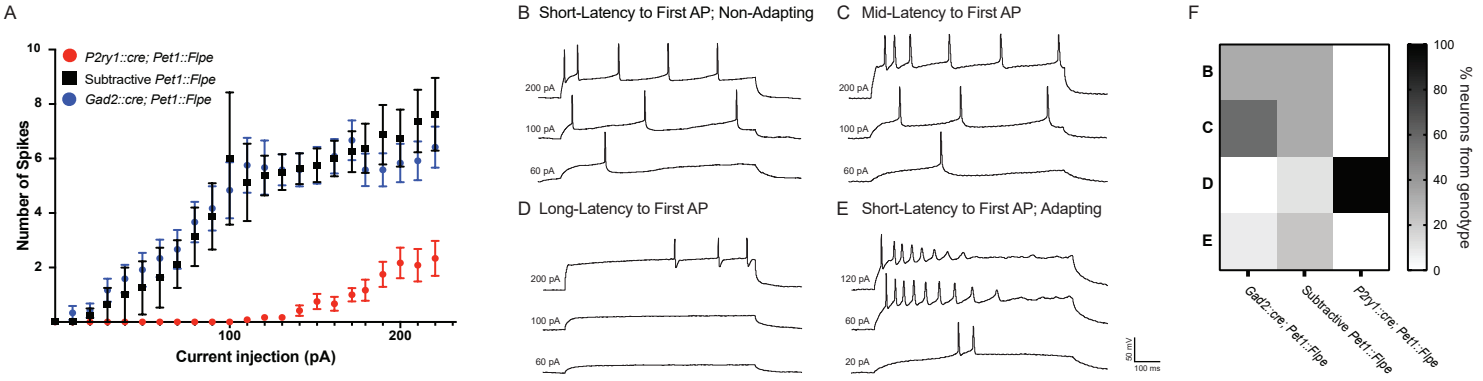

Figure 6- figure supplement 1

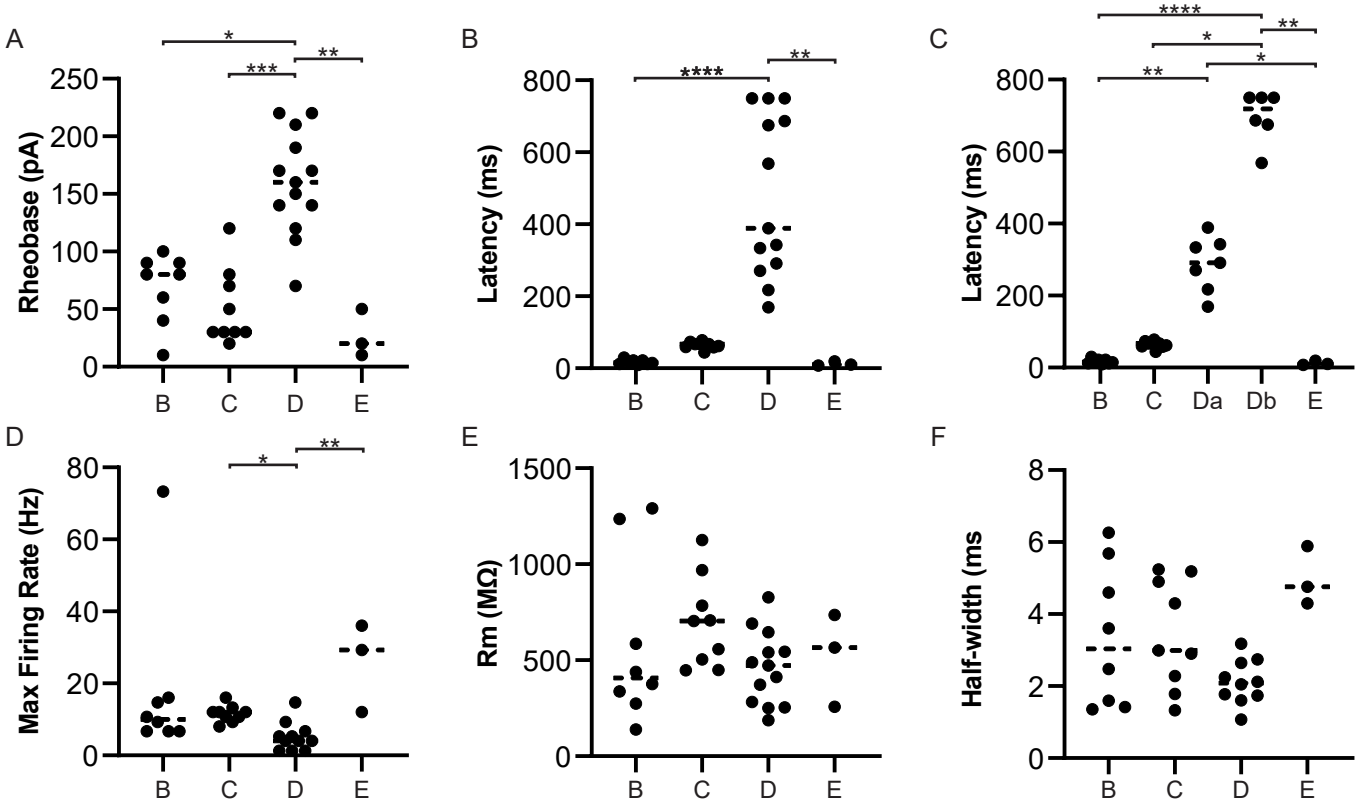

Figure 7

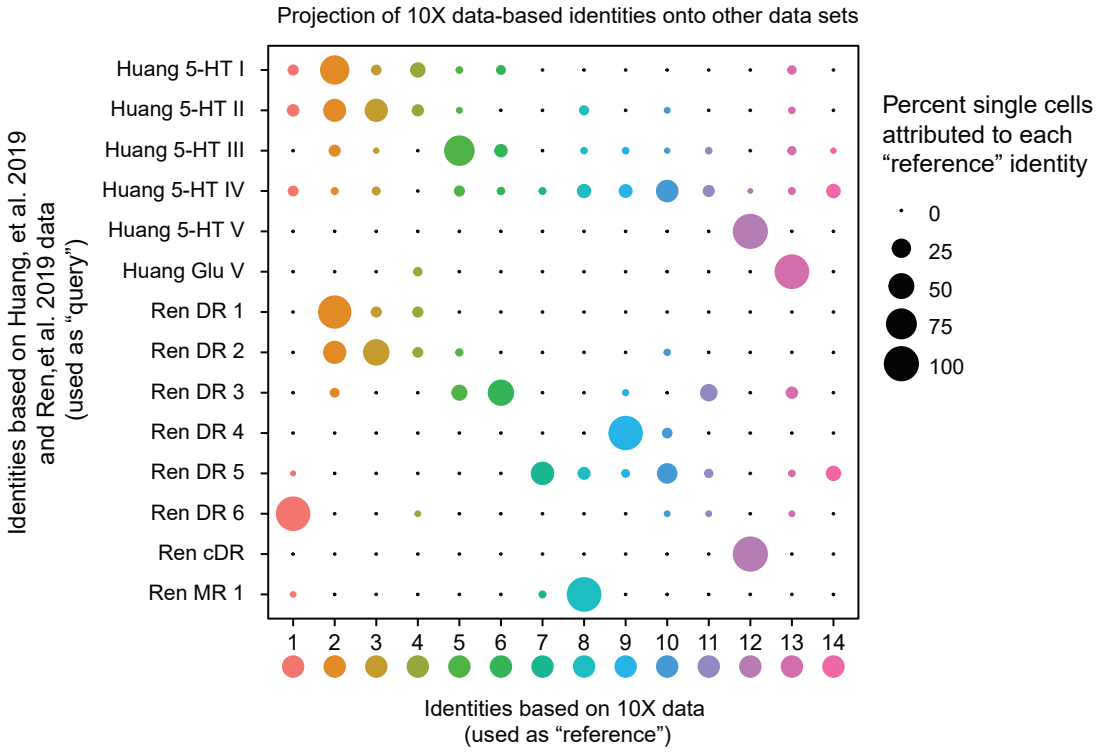

Figure 8